Structure and Mechanisms of Metalloenzymes for Incorporation of Water Across CN and C-Cl Bonds

Xinhang Yang
Marquette University

Recommended Citation

Yang, Xinhang, "Structure and Mechanisms of Metalloenzymes for Incorporation of Water Across CN and C-Cl Bonds" (2019). *Dissertations (2009 -)*. 871.
https://epublications.marquette.edu/dissertations_mu/871

Structure and Mechanisms of Metalloenzymes for Incorporation of Water Across CN and C-Cl Bonds

by

Xinhang Yang, B.Ed.

Beijing Institute of Technology

A Dissertation submitted to Faculty of the Graduate School,

Marquette University,

in Partial Fulfillment of the Requirements for

the Degree of Doctor of Philosophy

Milwaukee, Wisconsin

August 2019

ABSTRACT

STRUCTURE AND MECHANISMS OF METALLOENZYMES TOWARDS INCORPORATION OF WATER ACROSS CN AND C-CL BONDS

Xinhang Yang, B.Ed.

Marquette University, 2019

Metalloenzymes are widely involved in water incorporation across CN and C-Cl bonds.[1] In this research, the structure and mechanisms of two novel metalloenzymes that incorporate water across CN and C-Cl bonds were examined by biophysical approaches, computational modeling, and crystallographic methods.

In the research of water incorporation across CN bonds, a novel eukaryotic nitrile hydratase (NHase, EC 4.2.1.84) from *Monosiga brevicollis* (*Mb*NHase) was characterized, and the functional role of a $(His)_{17}$ section and an insert region in the *Mb*NHase, were examined by gene modifications. The kinetic and metal analysis suggested that Co-type eukaryotic NHases utilize a different mechanism for metal ion incorporation and post-translational activation compared to prokaryotic NHases.

In the research of water incorporation across C-Cl bonds, a novel Zn(II)-dependent chlorothalonil hydrolytic dehalogenase from *Pseudomonas sp. CTN-3* (Chd) was characterized and analyzed by a new direct spectrophotometric assay, metal analysis, and crystallography methods. Proton inventory studies indicated that one proton is transferred in the rate-limiting step of the reaction at pD 7.0 while multiple turnover pre-steady state stopped-flow data suggested a three-step model. The combination of these data along with pH dependent studies, allowed a catalytic mechanism for Chd to be proposed for the first time.

The X-ray crystal structure of a fifteen residue N-terminal truncated form of the Chd (Chd^T) was solved using single wavelength anomalous dispersion (SAD) to a resolution of 1.96 Å. Chd^T is a “head-to-tail” homodimer, formed between two α-helices from each monomer, with three Zn(II) binding sites, one of which is the active site Zn(II) while the third forms a structural site at the homodimer interface. The active site Zn(II) ion resides in a slightly distorted trigonal bipyramid or TBP geometry with His117, His257, Asp116, Asn216, and water/hydroxide as ligands. Substrate binding was examined by docking TPN into the hydrophobic channel with the most energetically favorable pose occurring for a TPN orientation that coordinates to the active site Zn(II) ions via a CN and that maximizes a π-π interaction with Trp227. The combination of the structure

and substrate docking studies with the previously reported kinetic studies, has allowed a refined catalytic mechanism to be propose.

ACKNOWLEDGMENTS

I would like to express my sincerest gratitude to Dr. Richard Holz, for giving me the opportunity to work on interesting bioinorganic projects and patiently guiding me. I would also like to thank my group members Irene and Wasantha for their support and advice.

I am grateful to Dr. Fiedler, Dr. Dockendorff, and Dr. Kincaid for serving as my Committee members and helping me as I work on this project. I appreciate Dr. Bennett and Dr. Dali Liu for their support and advice.

Finally, I thank my family and my friends for their support and encouragement.

TABLE OF CONTENTS

CHAPTER TWO STUDY OF A EUKARYOTIC NITRILE HYDRATASE FROM *MONOSIGA BREVICOLLIS*[53] 39

LIST OF TABLES

LIST OF FIGURES

CHAPTER ONE: INTRODUCTIONS OF METALLOENZYMES FOR INCORPORATION OF WATER ACROSS CN AND C-CL BONDS

1.1 General Introductions

Metalloenzymes are widely involved in water incorporation across CN and C-Cl bonds.[1] They make significant contributions to multiples areas including industries[2], clean energy[3], and environmental protection[4] because they convert toxic compounds to higher value or lower toxicity products. Understanding the enzymatic incorporation of water across CN and C-Cl bonds is important because it helps to increase catalytic efficiency and synthesis of novel biomimetic catalysts. However, significant details remain to be determined to understand their full catalytic cycles, especially for a growing number of new enzymes reported each year. A major challenge is understanding the structure of their active sites that are catalytically important. In this research, the structure and mechanisms of two novel metalloenzymes that incorporate water across CN and C-Cl bonds were examined by biophysical approaches, computational modeling, and crystallographic methods.

The first project analyzes the function of the insert region found between the α and β-subunits in the eukaryotic nitrile hydratase from *Monosiga brevicollis* (*Mb*NHase). Nitrile hydratases (NHases) catalyze the hydration of nitriles to their corresponding amides under mid conditions.[5] *Mb*NHase is not only the first example of a nitrile hydratase from a eukaryotic species, but also the first example of a cobalt-type nitrile hydratase that undergoes self-activation. *Mb*NHase has similar α and β-subunits to other cobalt-type nitrile hydratases, except the insert region between α and β-subunits. The function of this special sequence is not understood but may play a role in the self-activation of *Mb*NHase.

The second project is the characterization of a novel hydrolytic dehalogenase that converts Chlorothalonil (TPN; 2,4,5,6-tetrachloroiso-phtalonitrile) to 4-hydroxy-chlorothalonil (4-OH-TPN). Chd was recently found to be the first hydrolytic enzyme that is capable of hydrolyzing an aromatic C-Cl bond in the absence of a co-factor, which is unusual in biological systems.[6] However, prior to our studies, most of the details about Chd, including its structure and catalytic mechanism were unknown. In a hydrolysis reaction, the crucial steps are water activation and nucleophilic attack, which is difficult for chlorothalonil due to its nonpolar structure and the sp^2 hybridization of the aryl carbon. Thus, kinetic and spectroscopic studies along with DFT calculations are used to gain insight into this unusual hydrolysis reaction.

The third project involves the crystallization and solution of the X-ray crystal structure of Chd. Even though most of the important kinetic details were obtained in project two, structural data is required to understand how chlorothalonil binds to the active site of Chd and how the enzyme activates a water molecule and chlorothalonil for hydrolysis. The closest sequence identity to Chd is metallo-beta lactamase (E.C. 3.5.2.6) with 19% so obtaining the X-ray crystal structure of Chd is critical to understanding its catalytic mechanism.

1.2 Introduction of a Eukaryotic Hydratase for Incorporation of Water Across CN Bonds

1.2.1 Introduction to nitriles

Nitriles are organic compounds that contain a triple bond between the carbon and nitrogen atoms (C≡N). Nitriles are generally toxic and are synthesized by plants such as cassava and sorghum. Some bacterial and fungal species, such as chromobacterium violaceum, can also produce nitriles such as β-cyanoalanine.[7] The metabolism of nitriles by microorganisms enable them to obtain carbon and nitrogen depending on the enzymes they express, like nitrile hydratases (NHases), nitrogenases, or nitrilases.[8] Nitriles are also found in some useful materials like methyl acrylonitrile, which is the main ingredient in super glue, and nitrile rubber for latex-free laboratory and medical gloves.[9] Nitriles play important roles in industry and agriculture as they can be used for the preparation of amides, carboxylic acids, amines, esters, heterocyclic compounds, ketones, and amidines as well as important organic intermediates, feedstocks, solvents, extractants and pesticides.[7, 8b]

1.2.2 Nitrile metabolism

Various enzymes participate in nitrile metabolism, such as NHase, nitrilase, amidase, oxygenase, nitrogenase, oxynitrilase, etc… (Figure 1).[9]

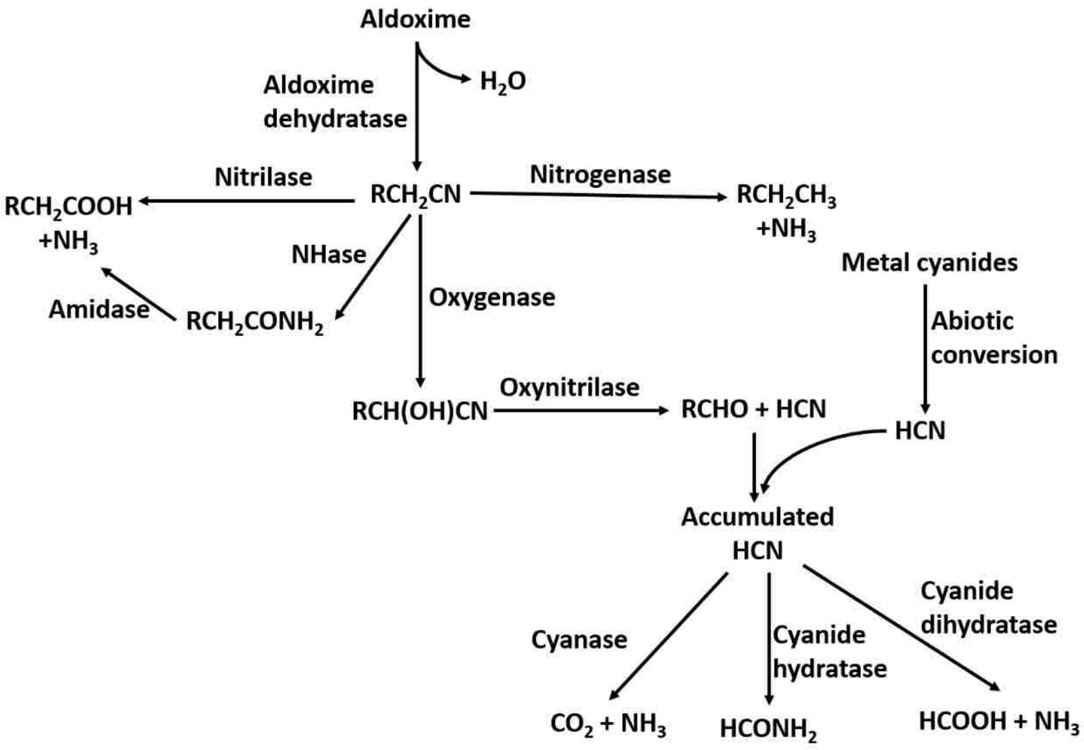

Figure 1. Different pathways of nitrile metabolism The NHase plays important role in the first step of nitrile degradation to ammonia and acid.

Initially, nitriles are synthesized from aldoxime by aldoxime dehydratase, after which two nitrile degradation pathways allow the formation of basic ammonia and an organic acid.[10] The first step of this pathway is catalyzed by nitrilase[8b, 10-11] or nitrogenase,[12] enzymes, which degrade nitriles to their corresponding acid or ammonia, respectively. A second pathway depends on NHases, which catalyzes the hydration of nitriles to amides. The resulting amide is then further degraded by an amidase to ammonia and an acid.[13] Most microorganisms contain the enzymes for at least one pathway, but certain bacteria like *Rhodococcus erythropolis* AJ270 contain the genes of NHase, amidase, and nitrilase.[14] The function of these enzymes may be related to nutrient metabolism, hormone synthesis, nitrile detoxification, or nutrient assimilation.[8b]

1.2.3 General introduction of nitrile hydratase (NHase, EC 4.2.1.84)

The high industrial demand for amides, particularly polyacrylamide and nicotinamide, is traditionally met through manufacturing processes that requires conditions of high acidity, pressure, and temperature (200 – 400°C), along with metal catalysts such as Raney copper.[15] These industrial reactions are economically inefficient and do not yield pure amide product, due to the formation of unwanted acid side products. NHases catalyze the stereo- and regio-specific hydration of nitriles to their corresponding amides under ambient temperature and physiological pH. NHases are widely used in organic synthesis within the chemical and pharmaceutical industries because of their energy-saving and eco-friendly catalytic reaction. For example, NHases are used to produce acrylamide (more than 30,000 tons per year) and nitcotinamide in single step reactions, with the elimination of the formation of acid side products.[15] They are also used for nitrile detoxification, which includes the bioremediation of toxic nitrile-containing compounds (such as herbicides or industrial effluents) from soil and aquatic environments.[1a]

1.2.4 Typical Structure of Nitrile Hydratase

There are two types of NHases: Co-type and Fe-type.[16] The NHase from *Pseudonocardia thermophila* JCM3095 (*Pt*NHase) is a typical example of a Co-type NHase,[17] while those from *Comamonas testosteroni* NI1 (*Ct*NHase) and *Rhodococcus equi* TG328-2 (*Re*NHase) are examples of Fe-type NHases. These prokaryotic NHase enzymes are typically made up of two, non-homologous sub-units (α and β) that are 20-35 kDa (Figure. 2) forming heterotetramers ($\alpha_2\beta_2$).[18] The active site is located at an interface between the α- and β-subunits with the α-subunit providing the residues that function as metal ligands, while β-subunit residues form hydrogen bonds within the second coordination sphere and play a role in catalysis.[19] In some organisms, NHase is made up of three sub-units forming a heterohexamer $(\alpha\beta\gamma)_2$ (*Toyocamycin*-NHase).[20]

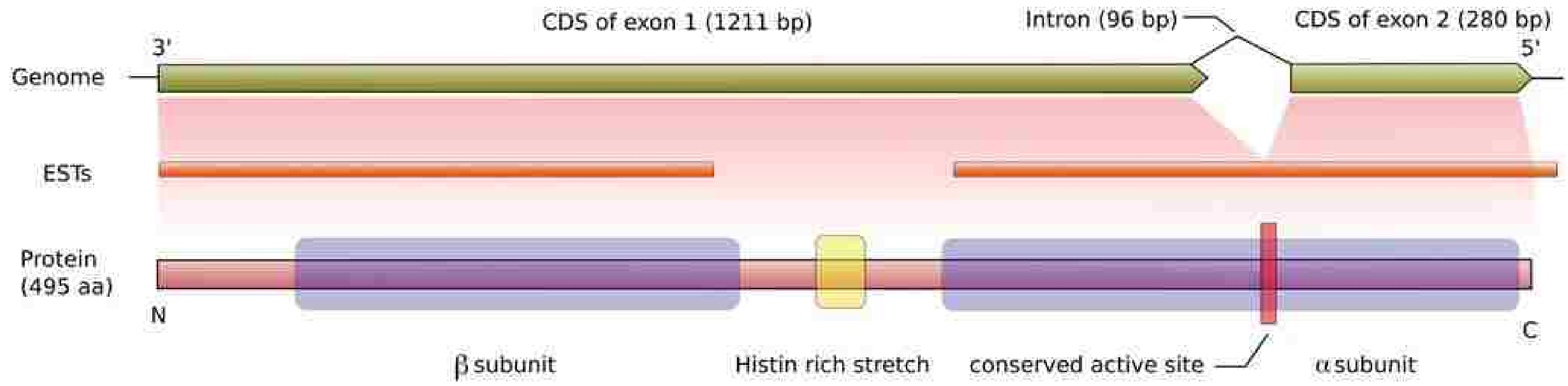

Figure 2. Sequence of *Mb*NHase genomic region and peptide. The histidine rich sequence is at the middle of insert region between two subunits.

*Pt*NHase has been crystallographically characterized and is an $\alpha_2\beta_2$ heterotetramer. One αβ heterodimer exists in an asymmetric unit and the αβ heterodimer loosely interacts with another αβ heterodimer. A crystallographic two-fold axis corresponds to the (αβ)-(αβ) interface (Figure. 3).[17] Co- and Fe-type NHase active sites contain a highly conserved.

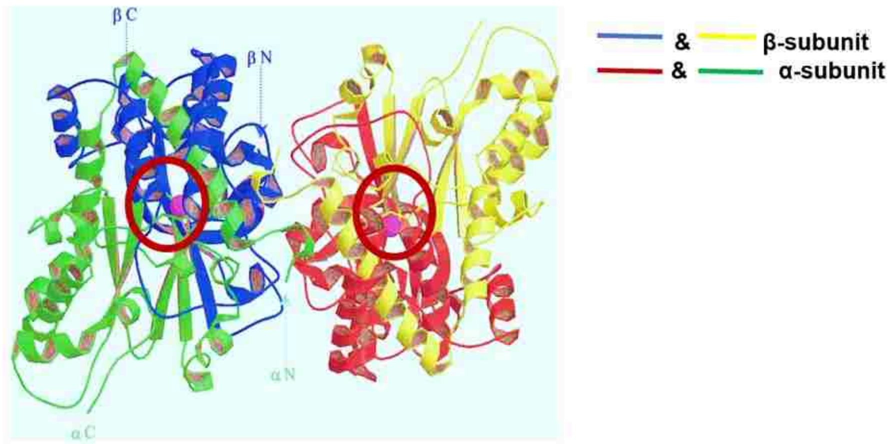

Figure 3 A ribbon drawing diagram of the $\alpha_2\beta_2$ heterotetramer of *Pt*NHase. The active sites (red cycle) were between α and β subunits.

amino acid sequence within the metal binding motif (Cys-Thr/Ser-Leu-Cys-Ser-Cys-Tyr/Thr) (Figure 4). This motif binds a low-spin ($S = {}^1/_2$) Fe(III) or ($S = 0$) Co(III) ion, which are coordinated by an axial cysteine thiolate; two equatorial peptide nitrogens; equatorial sulfur atoms that are post-translationally modified to cysteine-sulfenic (CysSOH) and cysteine-sulfinic (CysSO$_2$H) acids, respectively; and an axial water molecule in a geometry termed a “claw setting” (Figure. 4). The amide nitrogen atoms are deprotonated with significant double bond character and are strong sigma donors.[21] Fe-type NHases exhibit a similar active site structure to Co-type NHases (Figure 5a).

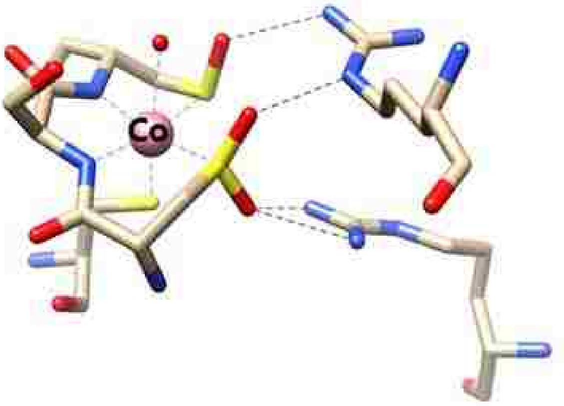

Figure 4 The active site of the Co-NHase from Pseudonocardia thermophila JCM 3095. Yellow, sulfur; Blue, nitrogen; red, Oxygen; Pink, cobalt (III).

In *Ct*NHase, which is an Fe-type NHase, the active site is solvent exposed (Figure 5b), whereas in most Co- and Fe-type NHases the active site is accessed through a narrow channel (Figure 5c).[16b]

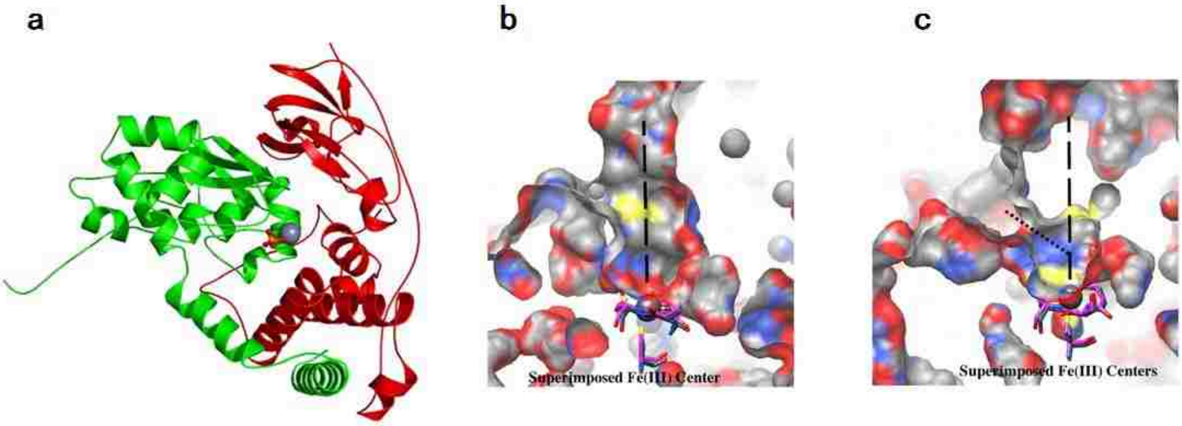

Figure 5. Structure of *Ct*NHase a) Structure of the *Ct*NHase heterodimer; b) Surface representation of the *Ct*NHase(left) and *Re*NHase(right) showing the

solvent accessible channel with the active site iron demonstrated by dash lines.

1.2.5 Enzyme Activation

Most NHases require the co-expression of an activator (e) protein for metal incorporation and post-translational modification of the active site Cys ligands.[22] The activator gene open reading frame (ORF) is typically found downstream from the genes encoding the α- and β-subunits (Figure 6a).[23] Figure 6b shows the proposed mechanism of activation for Co-type NHases.[22] The nhlB and nhlA genes express the β- and α-proteins, respectively, while nhE produces (e). The nhlE gene lacks any known metal binding motifs but exhibits significant sequence similarity to the β subunit (~27% identity). This gene organization allows (e) to form a complex with the apo-α-subunit after translation (αe_2).

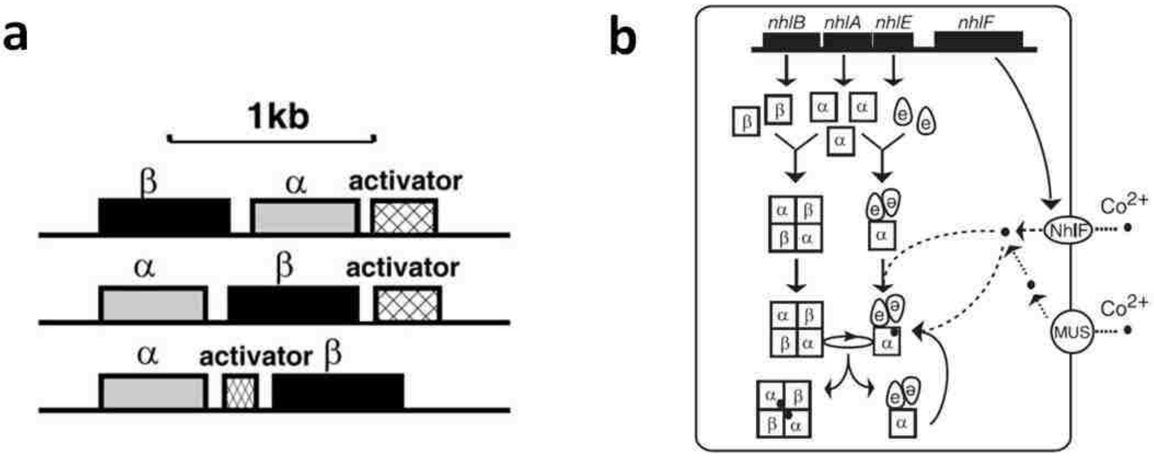

Figure 6. Activator and metal incorporation a) Co-types of NHases with different gene organizations; b) A proposed model for the process of cobalt incorporation into NHase The NhlE is the gene for activator protein expression while NhlF is gene of membrane protein for cobalt transportation.

The nhlF gene encodes a membrane bound protein that functions as a channel for

Co(II) transportation. Once Co(II) enters the cell, it is coordinated by the apo-αe_2 complex, resulting in a Co(II) bound holo-αe_2 form after which the holo-$\alpha_2\beta_2$ heterotetramer is formed through replacement of the cobalt-free α-subunit in apo-$\alpha_2\beta_2$ with the Co(II)-containing α-subunit in holo-αe_2. During the biogenesis of NHases, the αe_2 complex is recycled. The NhlE protein is proposed to act not only as a chaperone for self-subunit swapping, but also as a metallochaperone that is crucial for both Co(II) insertion and post-translational oxidation of the axial cysteine ligands. Interestingly, the apo-form of *Pt*NHase contains a disulfide bound in the active site, formed between the axial Cys and sulfenic acid Cys ligands (Figure7a). The apo-enzyme can be partially activated by dithiothreitol (DDT) followed by supplementation with metal (Figure 7b).[22-23]

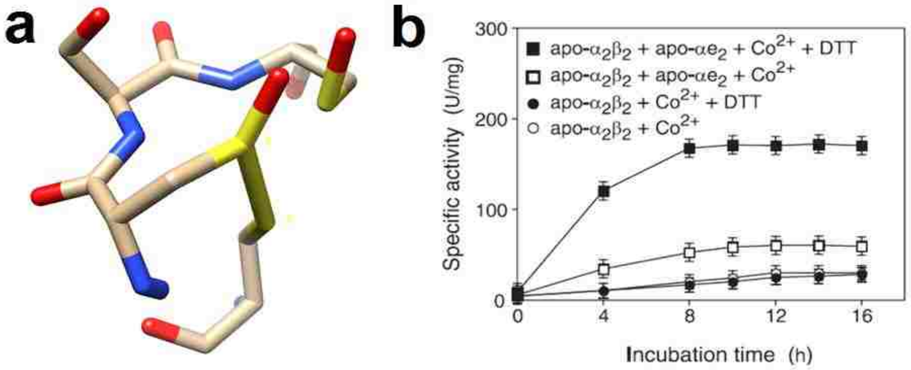

Figure 7. Apo nitrile hydratase activation. a) active site structure of structure apo NHase exhibits disulfide bond formation ; b) kinetic study of apo nitrile hydratase activation in 10mM KPB containing 20μM $CoCl_2$ at room temperature, pH=7.5. Data were obtained by at least triplicate independent experiments.

NHases are metal specific even though they have similar active site structures and catalytic mechanisms. Metal substitution of Co- and Fe-type

NHases is not possible based on current research.[24] While there are a few examples of cobalt substitution of Fe-type NHases that can be functionally expressed without an activator, there are no reports of iron substitution of Co-type NHases.[16b, 25] Even so, this cobalt substituted Fe-type NHase exhibits very low metal content and consequently, very little observed catalytic activity.

Given the active site structure of NHases, their mechanism of metal insertion, and post-translational activation metal substitution is extremely challenging. The first factor is their conserved active site motif. The difference between the active site of Co-type and Fe-type NHases is that two residues differe (α109 and α114), which are not active site metal ligands.[24b] Co-type NHases contains threonine at α109 and tyrosine at α114 [-C(T/S)LCSC(Y/T)-] while Fe-type NHase contains serine at α109 and threonine at α114 (Figure 8).

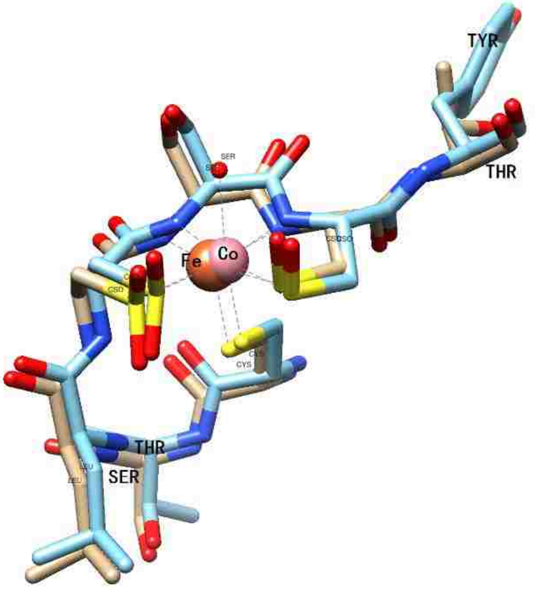

Figure 8. Superimposition of the active sites of the Fe-type NHase *from Comamonas testosteroni Ni1* and Co-type NHase from *Pseudonocardia thermophila JCM 3095*. Cyan: Co-type NHase; orange: Fe-type NHase. Red: oxygen, blue: nitrogen, yellow: sulfur.

The α109 threonine residue within the Co-type NHase active site undergoes a hydrophobic interaction with the side-chain of aVal136 within the α-subunit. On the other hand, Fe-type NHases possess a serine in position α109, which is hydrophilic, thereby offering diminished stabilization of the active site. The residue difference at α114 was hypothesized to play a role in the selective recognition of the corresponding activator protein.[24a] Metal specific activators are necessary to metal incorporation into NHases. Apo NHases can be prepared by expression in the absence of cobalt or iron by the required activator protein.[23] Subsequent incorporation of the corresponding metal ion could only be achieved in the presence of appropriate activator protein.

*Mb*NHase, a eukaryotic NHase, is a Co-type NHase whose active site is identical with prokaryotic Co-type NHases suggesting that *Mb*NHase is also specific for cobalt. Expression of *Mb*NHase using either Fe^{2+} or Fe^{3+} did not provide an Fe-type *Mb*NHase enzyme.

1.2.6 Proposed Mechanism

From previous research, three possible catalytic mechanisms have been reported: Inner sphere, outer sphere, and second outer sphere (Figure 9).[26] Within the inner sphere mechanism, substrate binds directly to the active site metal ion and the nitrile carbon is activated for nucleophilic attack. Therefore, amide forms after the transfer of two protons to the nitrile nitrogen. In the outer sphere and second outer sphere mechanisms, substrate does not bind directly to the metal ion; however, a coordinated water/hydroxide molecule is proposed to function as the nucleophile and attacks the nitrile carbon atom followed by proton transfer.

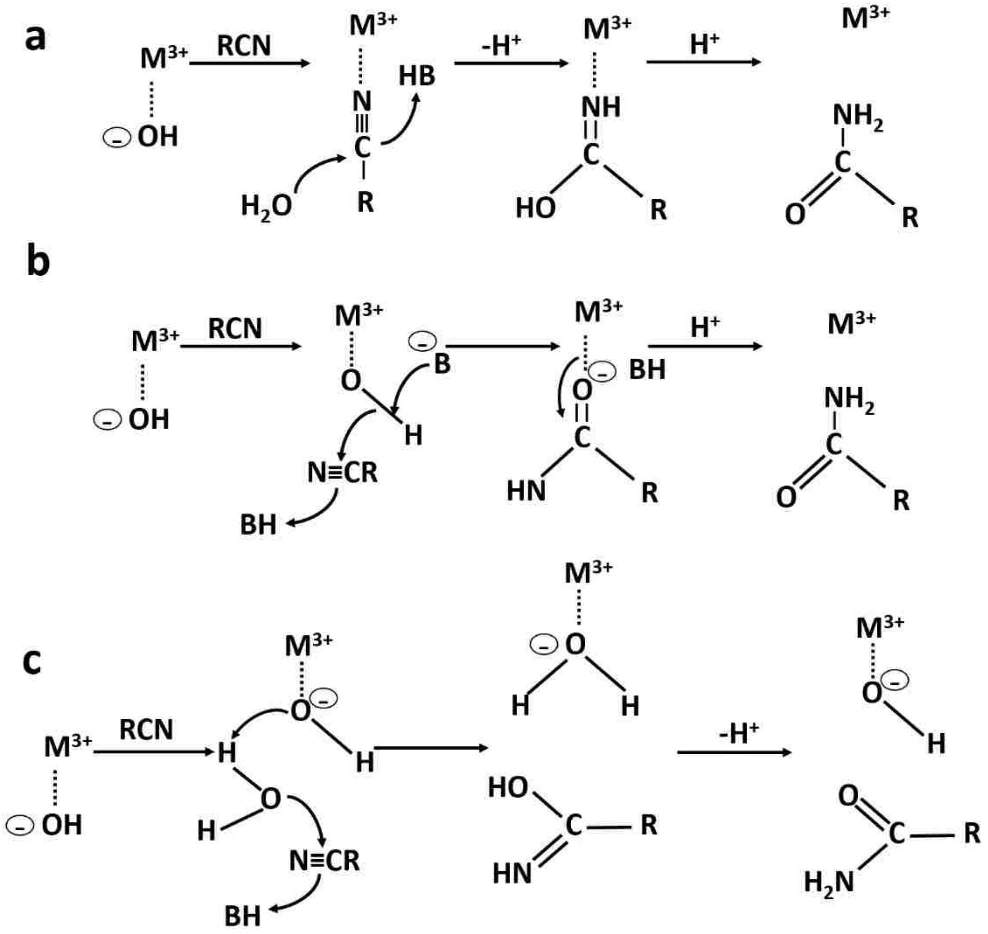

Figure 9. Three different mechanism. a) inner sphere mechanism that substrate directly binds to metal ion; b) outer sphere mechanism that substrate does not directly binds to metal ion; c) Second-outer sphere mechanism that substrate does not directly binds to metal ion.[26]

The inner sphere mechanism is supported by both experimental and theoretical studies including the X-ray crystal stucture of *Pt*NHase bound by 1-Butane boronic acid (BuBA).[19, 27] Surprisingly, the oxygen atom of the axial sulfenic acid (αCys113-SOH) forms a covalent bond with the boron atom of BuBA (Figure 10). This covalent bond indicates nucleophilic attack by the Cys-sulfenic acid oxygen on the empty P_z orbital of BuBA (Figure 10).

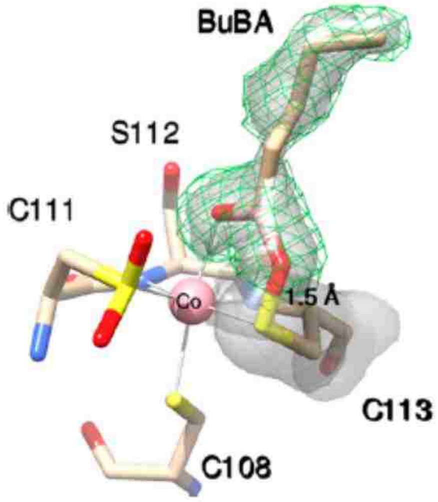

Figure 10. Stereo view of *PtNHase* bound to BuBA after co-crystallization with BuBA (PDB: 4OB1). The grey surface represent $2f_o - f_c$ map at the 1.1 σ level. The green mesh represent simulated-annealing omit map ($f_o - f_c$) at 2.8 σ.

Based on these data, a new catalytic mechanism was proposed that also takes into account DFT calculations and EPR data (Figure11).[27b] The first step involves the direct ligation of the nitrile to the active site Co(III) ion, which displaces the metal-bound water molecule and activates the CN bond toward nucleophilic attack. Following nucleophilic attack by the Cys-sulfienic acid ligand, a covalently bound cyclic intermediate is then formed. A water molecule can then attack the carbon atom of the Cys sulfur (Pathway A) or nitrogen atom

(Pathway B). The transfer of two protons to the nitrile nitrogen atom results in the formation of the corresponding amide, which can then be replaced by a water molecule to regenerate the catalyst. DFT calculations reveal that a water molecule is more likely to attack the cysteine sulfur atom than the nitrile carbon atom as the energy barrier for attacking the nitrile carbon atom is higher than the cysteine sulfur atom (Figure 11b).[27a]

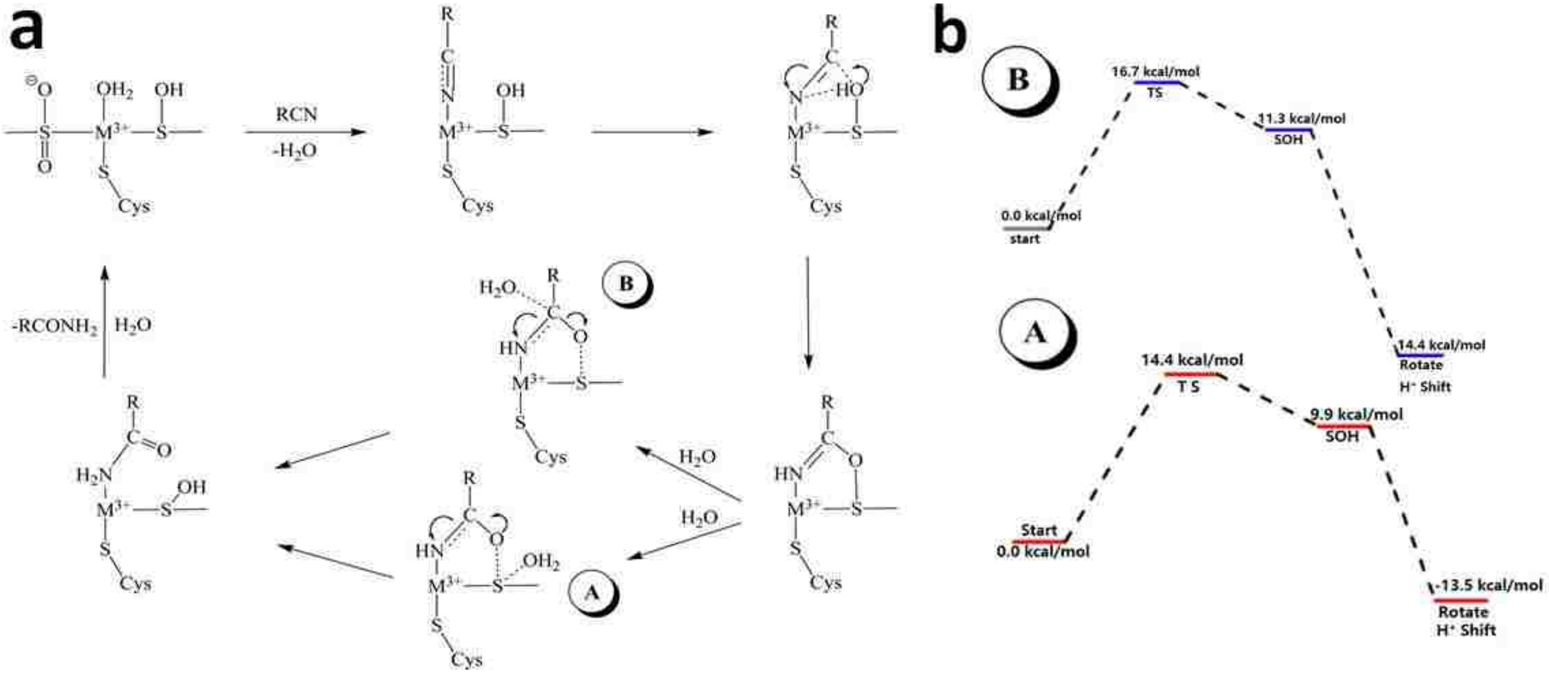

Figure 11. Carbon attack pathway and Sulfur attack pathway comparison. a) Proposed reaction mechanism of NHase based on kinetic and X-ray crystallographic studies of enzyme-inhibitor complexes; b) Energy level of two catalytic pathways.

Nucleophilic attack by a water molecule on the cysteine sulfur atom (Pathway A) is supported by MS data obtained on single turnover experiments with ^{18}O labeled water.[19] The ^{18}O only appeared on the sulfenic acid ligand within the active site and not within the amide product. Combination of these data with a recent isotope FTIR study and a time-resolved X-ray crystallographic study using the βR56K mutant of *Re*NHase, largely veririfed the mechanism shown in Figure 11a. In this mechanism (Figure 12), the sulfenic group is proposed to be deprotonated in the resting state and a water molecule is stabilized and ready for nucleophilic attack by forming a hydrogen bond with arginine and a backbone amide oxygen. [19] Upon substrate binding, the oxygen atom of the Cys sulfenic acid ligand attacks the carbon atom of the nitrile substrate to form the a cyclic reaction intermediate. The arginine residue is proposed to activate both a water molecule and the oxgen atom of the cyclic intermediate. The nitrile nitrogen atom extracts a proton from water, which facilitates nucleophilic attack of the water oxygen atom on the sufur atom of the sulfenic acid cysteine. The hydrogen atom of the regenerated sulfenic group is then transferred to the nitrile nitrogen atom allowing product to be released followed by coordination of water molecule to the active site. [19]

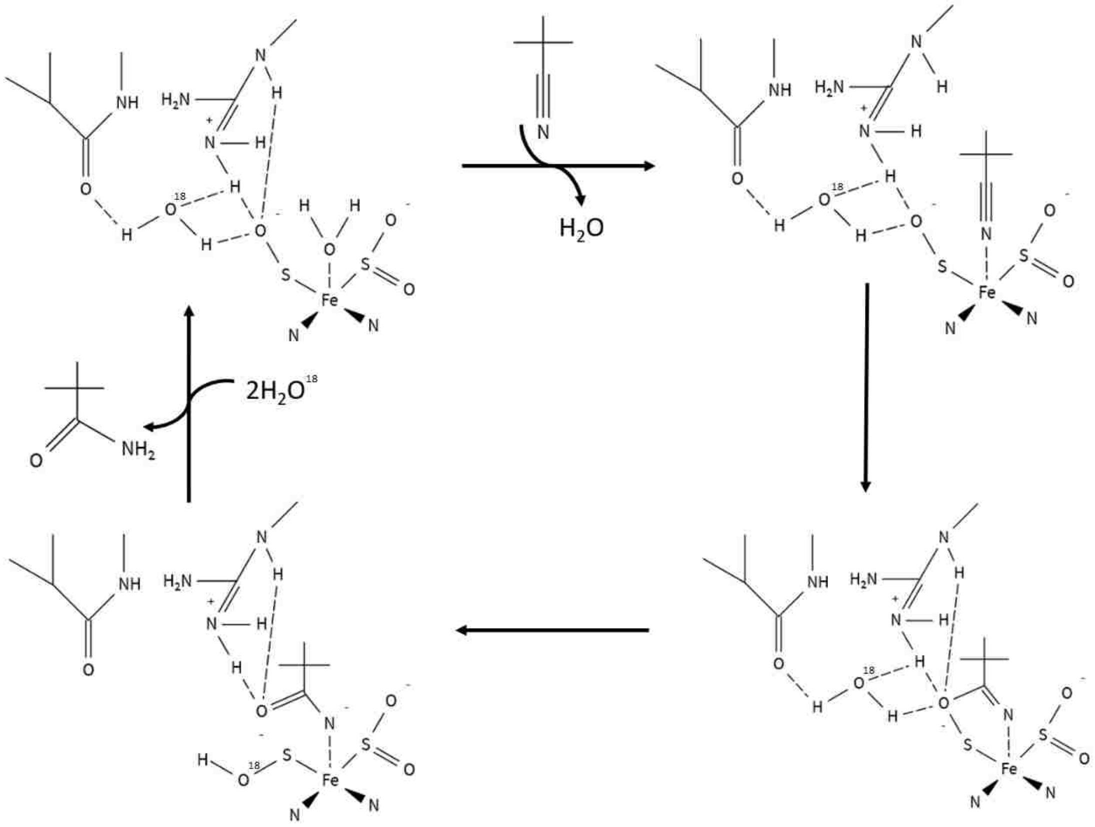

Figure 12. Catalytic mechanism proposed from time resolved X-ray crystallography of the βR56K mutant complexed. Nucleophilic attack by a water molecule on the cysteine sulfur atom (Pathway A) is supported by MS data obtained on single turnover experiments with ^{18}O labeled water.

1.2.7 A Eukaryotic Nitrile Hydratase

Until recently, NHase have only been found in prokaryotes; however, a novel gene that contains putative NHase α- and β-subunits was reported in several unicellular eukaryotic organisms (Figure 13).[28] Nearly all of these organisms reside in marine or aquatic environments and likely use nitriles as a source of nitrogen and carbon.

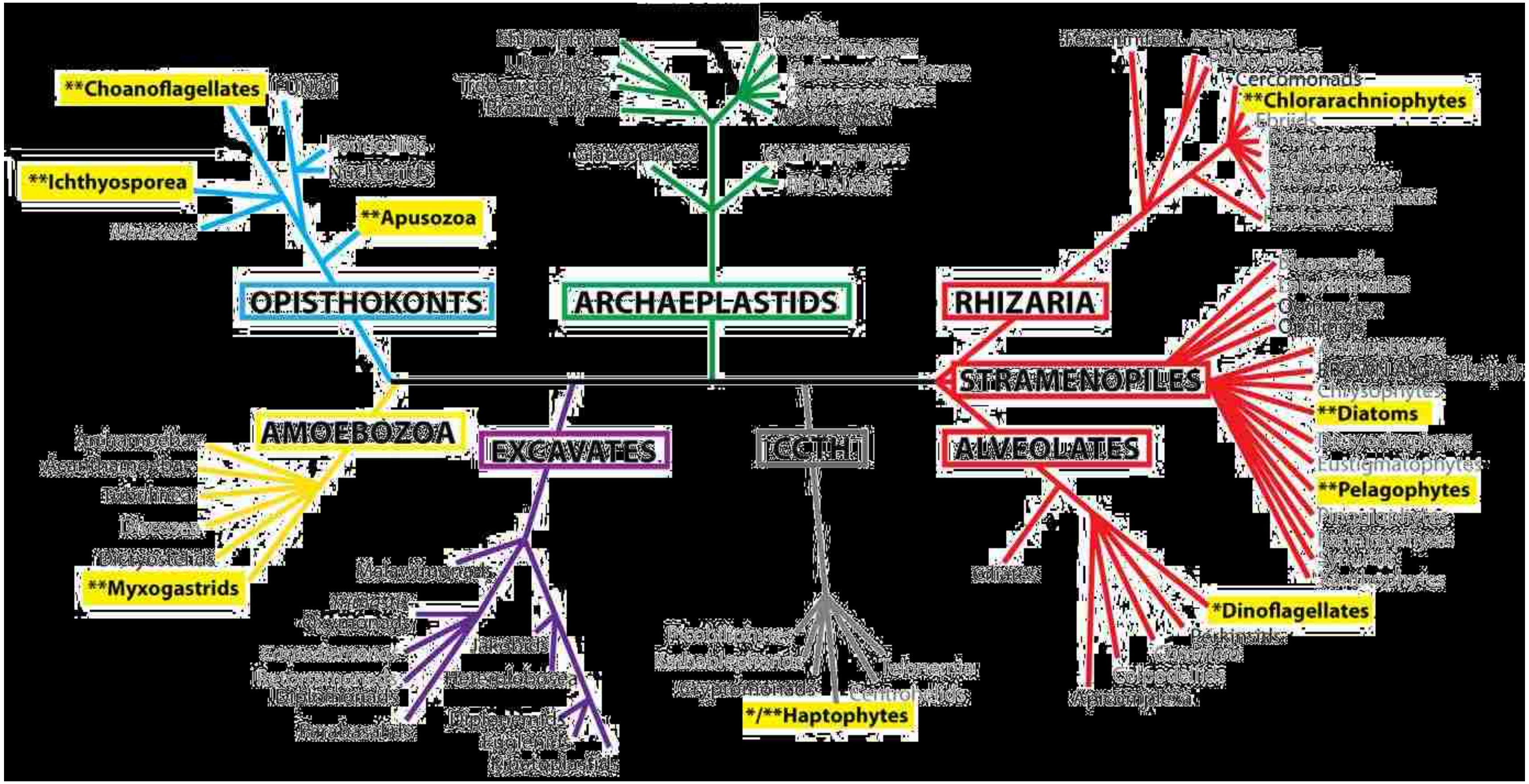

Figure 13. Schematic tree diagram of the eukaryotic super groups showing the location of nitrile hydratase. Species tree diagram of the eukaryotic super groups showing the location of nitrile hydratase. The single asterisks indicates both subunit genes, while single asterisks represent the single subunit gene.

Even though numerous putative NHase gene sequences were found in several eukaryotic species, no NHase from a eukaryotic organism has been reported. Therefore, we set out to determine if the possible α- and β-subunits from the eukaryotic organism *Monosiga brevicollis* could produce an active Co-type NHase, which I tentatively labeled *Mb*NHase. *Monosiga brevicollis* is one of 125 known chonoflagellates, which forms simple multicellular colonies found in both marine and freshwater environments. They have been shown to use their apical flagellum to prey on bacteria (Figure 14).[29]

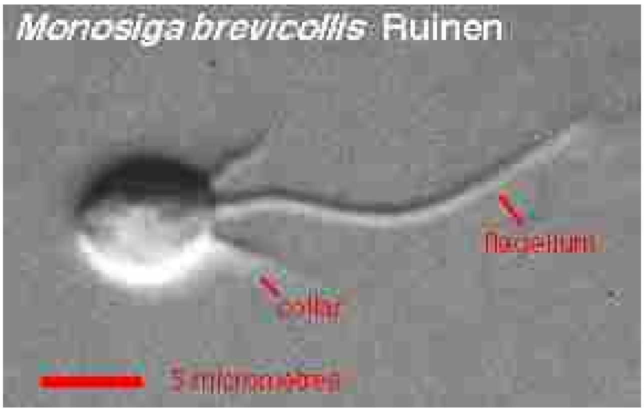

Figure 14. Micrograph of *Monosiga Brevicollis* obtained by Nomarski microscopy.

1.2.8 Sequence of the Eukaryotic Nitrile Hydratase

Unlike prokaryotic NHases, the ORF of purported eukaryotic NHases contains fused α- and β-subunits bridged by an insert made up of multiple histidine residues (Figure15a). The size of the insert and the number of histidine residues varies from one eukaryotic organism to another while the C-terminus region contains the strictly conserved NHase metal-binding motif (CTLCSCY) typically found in the α-subunit of Co-type NHases.[18] The α-subunit component of the purported *Mb*NHase exhibits ~23% sequence identity with the *Pt*NHase α-protein while the β-subunit component exhibits ~32% sequence identity with the *Pt*NHase β-protein.

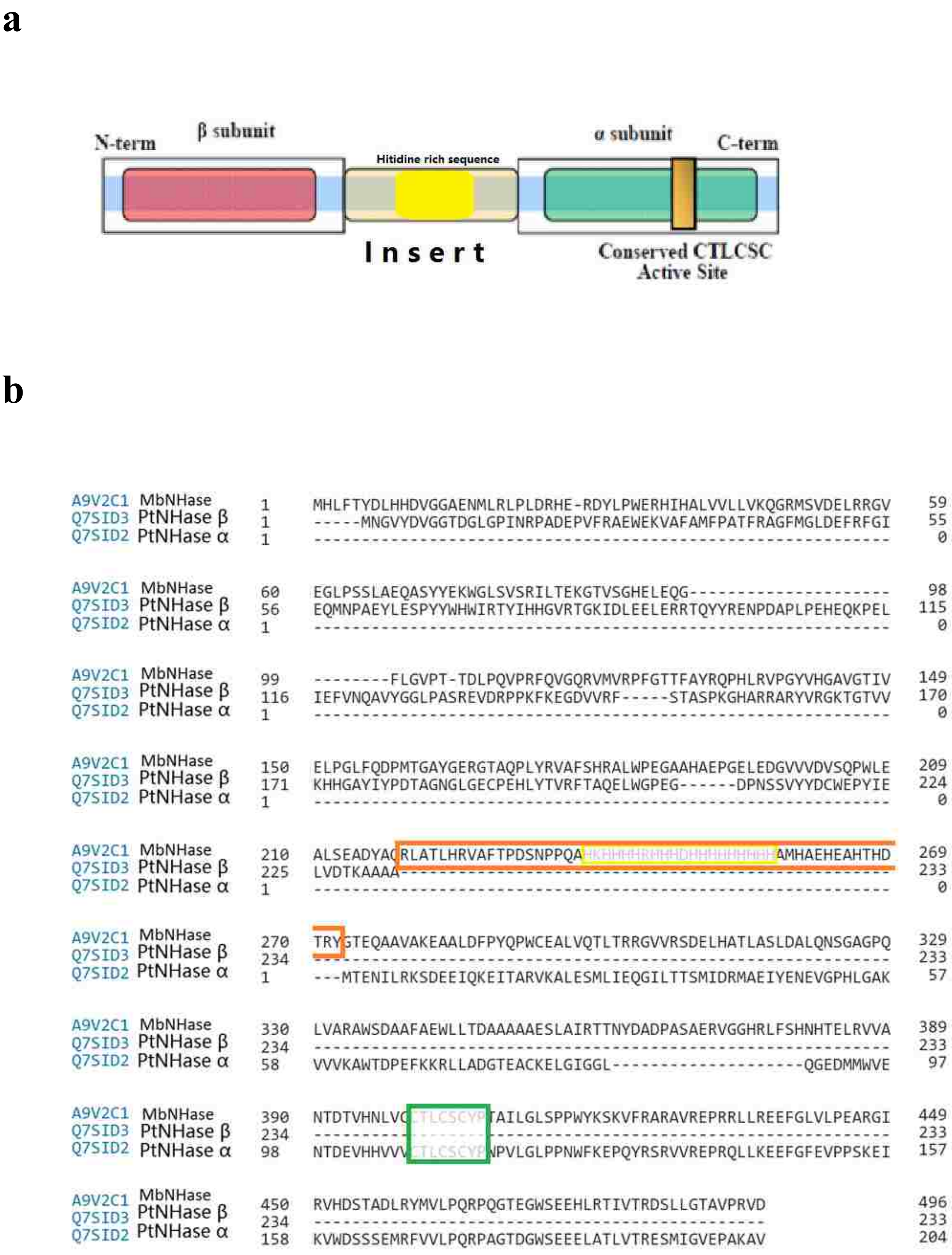

```
A9V2C1 MbNHase     1    MHLFTYDLHHDVGGAENMLRLPLDRHE-RDYLPWERHIHALVVLLVKQGRMSVDELRRGV   59
Q7SID3 PtNHase β   1    -----MNGVYDVGGTDGLGPINRPADEPVFRAEWEKVAFAMFPATFRAGFMGLDEFRFGI   55
Q7SID2 PtNHase α   1    ------------------------------------------------------------    0

A9V2C1 MbNHase     60   EGLPSSLAEQASYYEKWGLSVSRILTEKGTVSGHELEQG---------------------   98
Q7SID3 PtNHase β   56   EQMNPAEYLESPYYWHWIRTYIHHGVRTGKIDLEELERRTQYYRENPDAPLPEHEQKPEL  115
Q7SID2 PtNHase α   1    ------------------------------------------------------------    0

A9V2C1 MbNHase     99   --------FLGVPT-TDLPQVPRFQVGQRVMVRPFGTTFAYRQPHLRVPGYVHGAVGTIV  149
Q7SID3 PtNHase β   116  IEFVNQAVYGGLPASREVDRPPKFKEGDVVRF-----STASPKGHARRARYVRGKTGTVV  170
Q7SID2 PtNHase α   1    ------------------------------------------------------------    0

A9V2C1 MbNHase     150  ELPGLFQDPMTGAYGERGTAQPLYRVAFSHRALWPEGAAHAEPGELEDGVVVDVSQPWLE  209
Q7SID3 PtNHase β   171  KHHGAYIYPDTAGNGLGECPEHLYTVRFTAQELWGPEG------DPNSSVYYDCWEPYIE  224
Q7SID2 PtNHase α   1    ------------------------------------------------------------    0

A9V2C1 MbNHase     210  ALSEADYACRLATLHRVAFTPDSNPPQAHKHHHHRHHHDHHHHHHHHHAMHAEHEAHTHD  269
Q7SID3 PtNHase β   225  LVDTKAAAA---------------------------------------------------  233
Q7SID2 PtNHase α   1    ------------------------------------------------------------    0

A9V2C1 MbNHase     270  TRYGTEQAAVAKEAALDFPYQPWCEALVQTLTRRGVVRSDELHATLASLDALQNSGAGPQ  329
Q7SID3 PtNHase β   234  ------------------------------------------------------------  233
Q7SID2 PtNHase α   1    ---MTENILRKSDEEIQKEITARVKALESMLIEQGILTTSMIDRMAEIYENEVGPHLGAK   57

A9V2C1 MbNHase     330  LVARAWSDAAFAEWLLTDAAAAAESLAIRTTNYDADPASAERVGGHRLFSHNHTELRVVA  389
Q7SID3 PtNHase β   234  ------------------------------------------------------------  233
Q7SID2 PtNHase α   58   VVVKAWTDPEFKKRLLADGTEACKELGIGGL--------------------QGEDMMWVE   97

A9V2C1 MbNHase     390  NTDTVHNLVCCTLCSCYPTAILGLSPPWYKSKVFRARAVREPRRLLREEFGLVLPEARGI  449
Q7SID3 PtNHase β   234  ------------------------------------------------------------  233
Q7SID2 PtNHase α   98   NTDEVHHVVVCTLCSCYPNPVLGLPPNWFKEPQYRSRVVREPRQLLKEEFGFEVPPSKEI  157

A9V2C1 MbNHase     450  RVHDSTADLRYMVLPQRPQGTEGWSEEHLRTIVTRDSLLGTAVPRVD               496
Q7SID3 PtNHase β   234  -----------------------------------------------               233
Q7SID2 PtNHase α   158  KVWDSSSEMRFVVLPQRPAGTDGWSEEELATLVTRESMIGVEPAKAV               204
```

Figure 15. *Mb*NHase sequence a) The arrangement of the β- and α-subunits nitrile hydratase fusion in eukaryotes; b) Sequence alignment of MbNHase and PtNHase.

Orange: Insert of MbNHase sequence. Yellow: Histidine rich sequence; Green: conserved active site.

1.2.9 Possible Role of Subunit Fusion and the Histidine Rich Region

The catalytic role of fused α- and β-subunits as well as the histidine rich region found within the insert are unknown. In order to determine the possible role of these fused subunits, Xia and co-workers used dipeptides to fuse two subunits of a prokaryotic Co-type NHase (Figure 16).[30] A dramatic increase in activity was observed upon subunit fusion. However, the fused nitrile hydratase required an activator protein for functional expression.

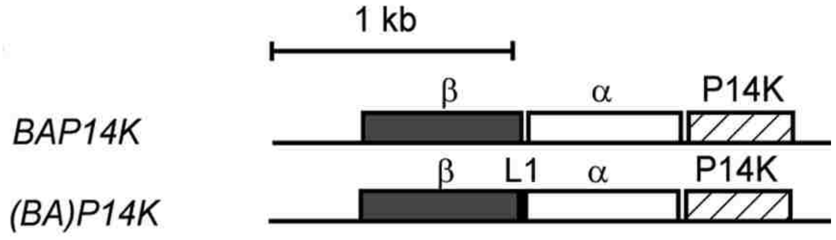

Figure 16. Genetic organization for the construction of wide type nitrile hydratase and fused subunits nitrile hydratase. L1: sequence for dipeptide, proline-glycine. P14K: activator gene.

Therefore, the histidine rich region observed in eukaryotic NHase genes was hypothesized to play the role of the activator protein suggesting that a fully functional MbNHase protein could be expressed without the co-expression of an activator protein. The Fe-type NHase, *Ct*NHase, was recently shown to be the only NHase that can be functionally expressed without an activator protein. This was hypothesized to be due to the presence of a channel along with the two histidine residues around the active site that may play a role in iron incorporation in the absence of an activator protein. Histidine rich regions are also found in metallochaperone and accessory proteins involved in the metallocenter assembly of nickel hydrogenases, whose histidine rich region can bind tightly and reversibly to nickel ions.[31]

1.2.10 Research status and problems

High demand for amides, particularly polyacrylamide and nicotinamide, is traditionally met through a manufacturing processes that requires conditions of high acidity, pressure, and temperature (200 – 400°C), along with metal catalysts such as Raney copper.[15] Energy costs and environmental pollution make this industrial process increasingly uneconomical, which has markedly increased the interest in the biocatalyst NHase.[14a] However, storage and the use of bioactive NHases requires specific conditions like constant temperature and pH. Also, most NHases depend on accessory proteins for metal incorporation and enzyme activation, which increases biosynthesis costs. The direct utilization of live cells may provide an alternative way for nitrile hydration.[32]

1.2.11 Summary

NHases play a significant role in industrial applications because they can hydrate amines to the higher value amide in a stereoselective and catalyticly efficient manner under ambient conditions. Understanding the determinants of NHase substrate and reaction specificity will facilitate engineering of both new enzyme-based and non-biological nitrile-hydrating catalysts with tailored catalytic properties. This in turn will act as a stimulus to the pharmaceutical industry to develop this technology, which will have a significant impact on current industrial synthetic methods used to prepare high value compounds, *e.g*. acrylamide, non-steroidal anti-inflammatory drugs, and agro-chemicals, to name a few.

The purported NHase from *Monosiga brevicollis* is expressed by a single gene that is made up of NHase type α- and β-subunits with a 17 histidine run between the C-terminus of the α-protein and N-terminus of β-subunit. This is a major difference form prokaryotic NHase enzymes such as *Pt*NHase, which has separated α- and β-subunit genes and a distinct gene that encodes an activator protein. The conserved active site residues suggest a similar catalytic mechanism, as proposed by Holz and co-workers.[22-24,31-33] The histidine rich region of the *Mb*NHase insert may play a role in metal ion insertion during protein expression as similar histidine rich sequences are found in metallochaperone and accessory proteins.[31] Future studies on the structure, activation, and catalytic mechanism of *Mb*NHase will provide insight into similarities and differences between eukaryotic and prokaryotic NHases.

1.3 Introduction of a Novel Hydrolytic Enzyme for Incorporation of Water Across C-Cl Bonds

1.3.1 Introduction of halogenated aromatic compounds

Halogenated aromatic compounds are known to be major organic pollutants based on United Nations and U.S environmental protection agency (EPA) data.[33] These compounds enter the environment as contaminants derived from industrial processes such as coal fired utilities, metal smelting, diesel trucks, and burning trash.[34] They are also widely used in industrial processes and within the agricultural business as solvents, defatting agents, and fungicides. It is quite challenging to remove them from the environment because of their stability and poor solubilities.[35] This is a major environmental problem, as halogenated aromatic hydrocarbons are highly toxic and carcinogens, which has led to numerous cases of human and animal poisonings.[36]

Chlorothalonil (TPN; 2,4,5,6-tetrachloroiso-phtalonitrile, figure 17) is one of the familiar examples of halogenated aromatic compounds as organochlorine fungicide for crops and fruits in our life [37], more than 5 Mil kilograms of which were consumed in the United States per year [38]. At room temperature, chlorothalonil is an odorless or slightly pungent, colorless crystalline solid and has low solubility in water (0.081mg/100mL). Chlorothalonil exhibits high toxicity to human, and it has been reported as a potential carcinogen as it shows as one of kidney cancer factors to mouse [37]. Because of these characters, increasing amounts of chlorothalonil have been releasing on surface water bodies, soil, and sediment as a kind of pollutant and threaten animals and human being in each year, resulting in high demand of degradation of this halogenated aromatic compound.

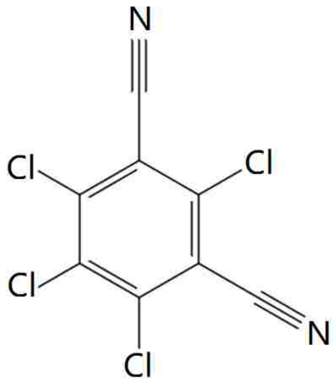

Figure 17. Structure of Chlorothalonil (TPN; 2,4,5,6-tetrachloroiso-phtalonitrile).

1.3.2. Dehalogenation pathways for halogenated compounds

Halogenated compound degradation are achieved with multiple reactions.[39] The primary step is dehalogenation because it reduces chemical stability and toxicity of chlorothalonil and intermediates during degradation pathways [40]. However, artificial degradation depends on precious metals at high temperature [41], which is not feasible in nature. Thus, dehalogenase plays crucial role in the primary step of degradation. Most biodehalogenations have been achieved through different pathways, including, thiolytic dehalogenation [42], oxidative dehalogenation [43], reductive dehalogenation [44] , and hydrolytic dehalogenation. [45]

The thiolytic dehalogenation pathway depends on glutathione S-transferase, which catalyzes the dehalogenation of dichloromethane via an S-chloromethyl glutathione intermediate (Figure 18).[42]

Figure 18. Thiolytic Dehalogenation via an S-chloromethyl glutathione intermediate.

The oxidative dehalogenation reaction pathway utilizes dioxygen and NADH to remove a halogen group from both aliphatic and haloaromatic compounds (Figure 19).[46]

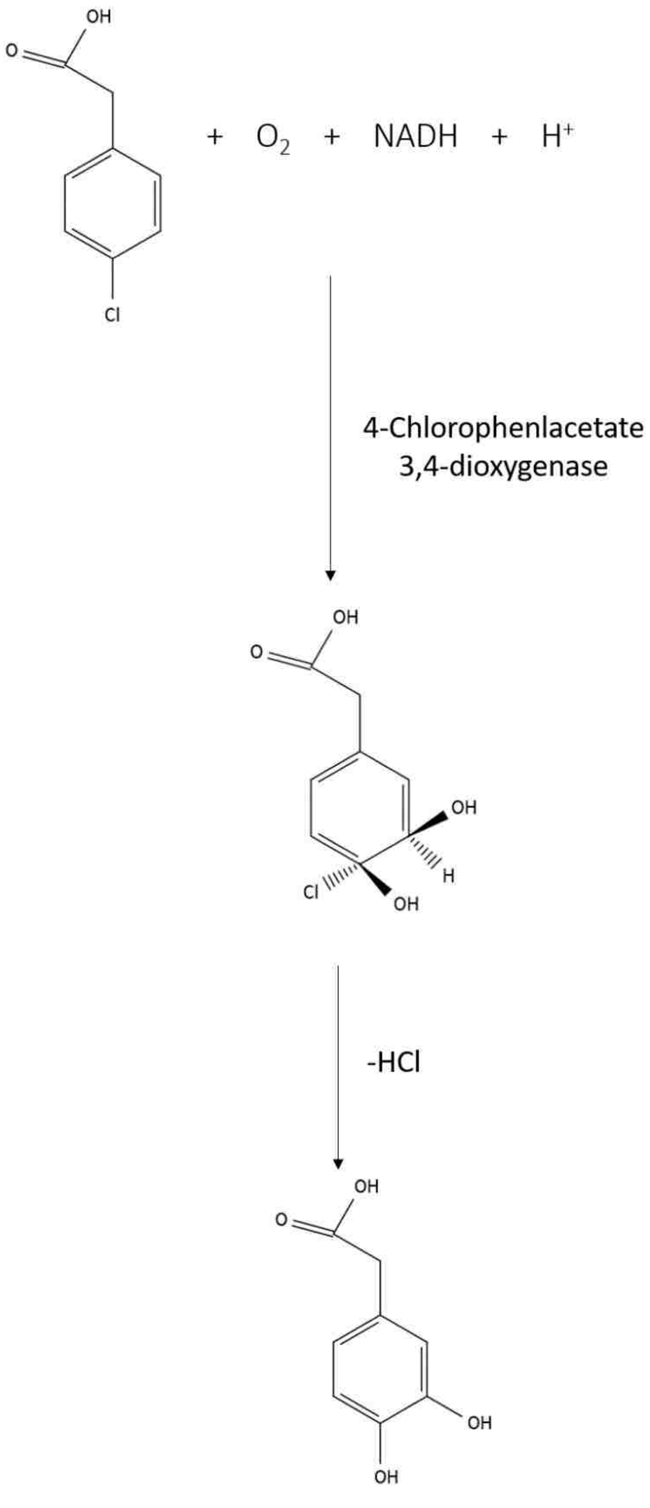

Figure 19. Oxidative pathway of oxidative dehalogenation depending on NADH and oxygen.

Reductive dehalogenation is important for the dehalogenation of chlorinated aromatics as they are utilized as electron acceptors by several bacterial specieses.[47] One example of reductive dehalogenation is the NADH-dependent 2-chloromaleylacetate dehalogenation reaction catalyzed by the maleylacetate reductase, which has been isolated from several *Pseudomonas* strains and *Ralstonia eutropha* (Figure 20). [47]

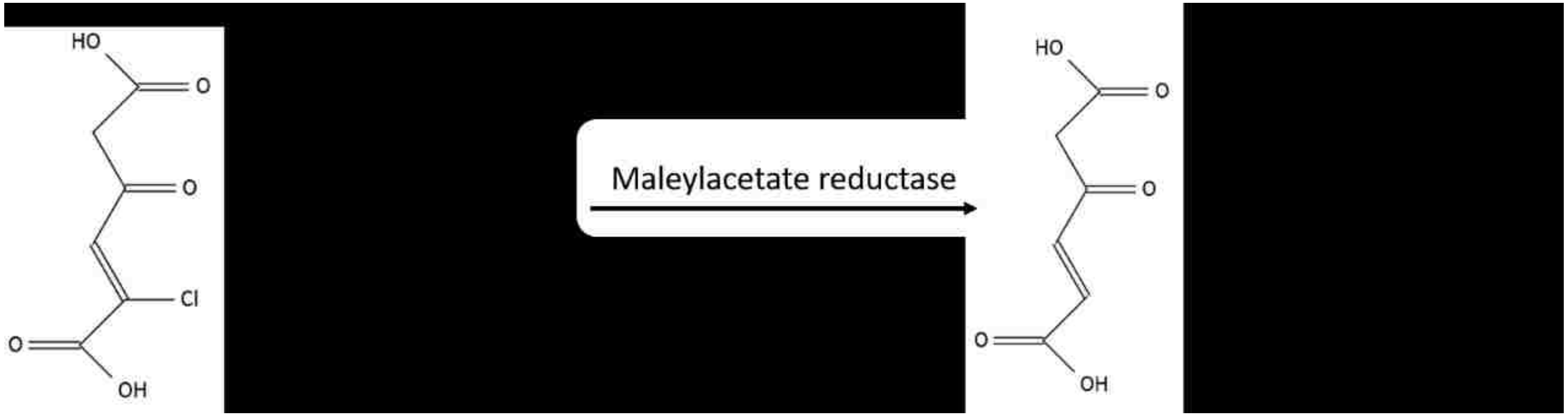

Figure 20. NADH-dependent reductive dehalogenation of 2-chloromaleylacetate to 3-oxoadipate under aerobic conditions by utilizing H+.

Hydrolytic dehalogenation substitutes a halogen with a hydroxide derived from water.[45a] Several hydrolytic dehalogenases that utilize halogenated aliphatic hydrocarbons and halogenated carboxylic acids as substrates have been characterized.[45a, 48] However, only a few enzymes that are capable of hydrolytically dehalogenating aromatic compounds have been reported.[6, 49] One example is 4-chlorobenzoyl–CoA dehalogenase, which is a member of the 4-chlorobenzoate degradation pathway (Figure 21).[49]

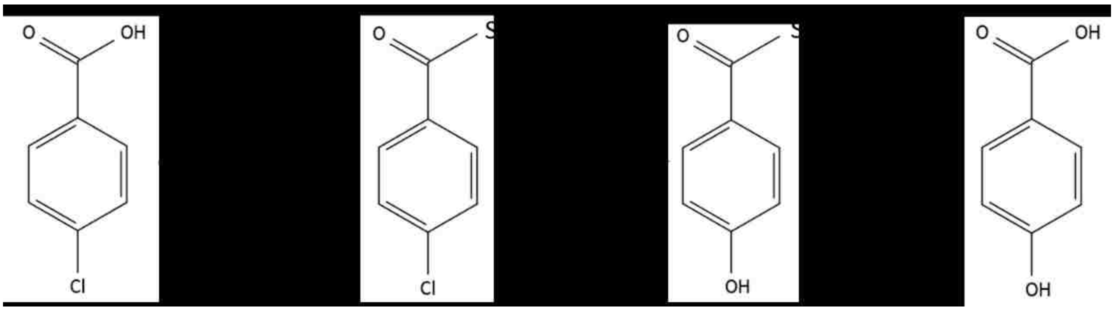

Figure 21. Mechanism of 4-chlorobenzoate dechlorination in *Pseudomonas* sp. CBS3 and *Acinetobacter* sp. strain 4-CB1.

3.1.3 Introduction of dehalogenase for aromatic compound chlorothalonil (Chd)

In 2010, *Pseudomonas sp*. CTN-3 was reported to efficiently catalyze the hydrolytic dehalogenation of chlorothalonil to 4-hydroxy-trichloroisophthalonitrile which is less toxic (Figure 22).[6] *Pseudomonas* is a genus of motile, polar-flagellate, non-spore-forming, strictly aerobic bacteria (family *Pseudomonadaceae*) containing straight or curved, but not helical, gram-negative rods that occur singly in soil and in freshwater and marine environments.[50]

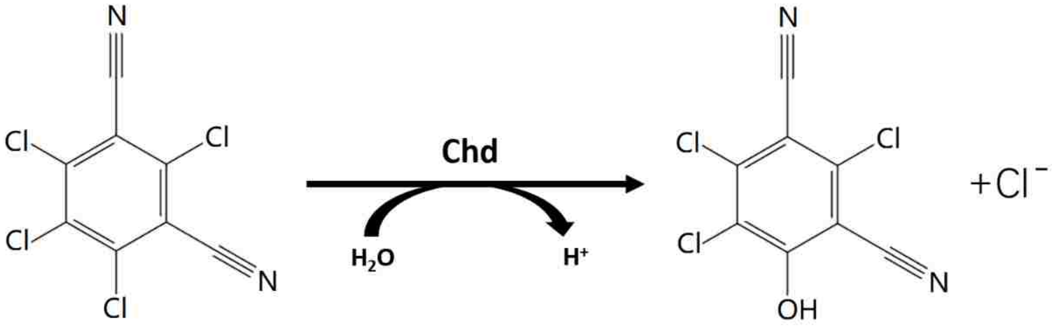

Figure 22. First-step dechlorination mechanism of 2,4,5,6-tetrachloroisophthalonitrile(chlorothalonil) in Pseudomonas sp. CTN-3.

It was shown that the enzyme responsible for this reaction is a novel metallo-hydrolytic chlorothalonil dehalogenase (Chd) and shares sequence similarity to metallo-β-lactamases (MBL).

3.1.4 Research status and problems

Large amounts of halogenated compound are utilized in the industrial and agricultural fields on an annual basis. Due to their insolubility and resistance to biodegradation, halogenated compounds contaminate the soil and water, making them a significant environmental problem.[51] Dehalogenation of these compounds helps to reduce their toxicity and the risk of forming unwanted intermediates during subsequent metabolic degradation steps. However, most dehalogenation reactions are achieved using precious metal catalysts at high temperatures[41], while biological catalyzes are rare.[52] Exploring and utilizing new enzymes for biological dehalogenation is critical for environmental protection. Understanding the structures and mechanisms of these dehalogenases will provide new models for biomimetic catalysis synthesis.

3.1.5 Summary

Halogenated aromatic compounds are widely used industrially and in the agricultural business as pesticides and fungicides. Since halogenated aromatic compounds are typically highly toxic and can act as carcinogens, it is important to develop methods to degrade these compounds to environmentally more favorable complexes. Four different types of dehalogenation processes are known, all of which play important roles in the biodegradation of halogenated hydrocarbons, which in turn, reduces the risk of toxic intermediates forming during subsequent metabolic steps. Hydrolytic dehalogenation enzymes have attracted significant interest for halogenated compound bioremediation. However, enzymes that catalyze the hydrolytic dehalogenation of aromatic compounds are rare. Chd is one of two enzymes reported that are capable of hydrolyzing the widely used fungicide chlorothalonil. It is the only hydrolytic dehalogenase that that does not require a coenzyme. Chd displays sequence similarities to MBLs including parts of their conserved metal binding motif. Even so, Chd also has significant sequence differences that may be important in facilitating the unique metal dependent hydrolytic dehalogenation reaction.

1.4 Research Aims

NHases have attracted substantial interest as biocatalysts in preparative organic chemistry and are currently used in the large-scale industrial production of acrylamide and nicotinamide. The major impediment to industrial uses of NHases is the lack of a detailed understanding of their catalytic mechanism. Therefore, for the NHase studies, I will

(1) Examine the catalytic mechanism via kinetic, molecular biological, and spectroscopic techniques.

(2) Analyzing the function of the insert region found between the α and β-

subunits in the eukaryotic nitrile hydratase from Monosiga brevicollis;

(3) Study the possible activation mechanism.

For the dehalogenase studies, understanding the structure and reaction mechanism of Chd will provide new insight into the metal catalyzed hydrolytic dehalogenation of aromatic compounds. As chlorothalonil is toxic, the mechanistic data obtained will also benefit the chemical and agricultural business. In this regard, the proposed research is geared towards understanding the structure and mechanism of Chd. Specifically:

(1) Expressing and purifying Chd.

(2) Characterization studies of Chd via kinetic, molecular biological, and spectroscopic techniques.

(3) Investigating the role of metal in Chd.

(4) General mechanistic studies by new developed spectrophotometric methods, mutagenesis stopped-flow experiments.

(5) Structure determination and substrate binding model prediction.

CHAPTER TWO STUDY OF A EUKARYOTIC NITRILE HYDRATASE FROM *MONOSIGA BREVICOLLIS*[53]

2.1 Introduction

Nitrile hydratases (NHases, EC 4.2.1.84) are metalloenzymes that contain either a non-heme Fe(III) ion (Fe-type) or a non-corrin Co(III) ion (Co-type) in their active site [54]. NHases catalyze the hydration of nitriles to their corresponding higher value amides under mild conditions (room temperature and physiological pH) and have attracted substantial interest as biocatalysts in preparative organic chemistry and bioremediation processes [55]. NHases have historically been only found in prokaryotes; however, multiple eukaryotic organisms were shown to contain genes that potentially encode NHase enzymes [18, 28]. I recently cloned and over-expressed the candidate gene from the eukaryotic organism *Monosiga brevicollis* in *E. coli* and characterized a fully functional Co-type NHase gene product, with fused α- and β-subunits linked by a $(His)_{17}$ region (*Mb*NHase) (Figure 1) [56]. Size-exclusion chromatography indicated that *Mb*NHase is an $(\alpha\beta)_2$ homodimer in solution, analogous to the $\alpha_2\beta_2$ heterotetrameric architecture of prokaryotic NHases, of which numerous X-ray crystal structures exist [54, 57].

Several open reading frames (ORFs) have been identified just downstream from the structural α- and β-subunit genes in prokaryotic NHases, and one of these genes has been proposed to function as an activator (*ε*) protein [58]. The prevailing dogma is that both Co- and Fe-type NHase enzymes require the co-expression of an (*ε*) protein to be fully metallated, post-translationally modified, and fully functional [58]. No such (*ε*) protein has been identified for eukaryotic NHases, such as *Mb*NHase [18, 28]. It is tempting to speculate that the insert region within *Mb*NHase, which contains a $(\text{His})_{17}$ motif, plays the role of the (*ε*) protein. Histidine rich regions are present in some cobalamin (vitamin B12) biosynthetic pathway proteins, *e.g.*, the chelatase CbiX enzyme from *Bacillus megaterium* and CobW from *Pseudomonas denitrificans* [59]. Histidine rich regions are also found in accessory proteins involved in metallocentre assembly of nickel hydrogenases and ureases, such as HypB from *Bradyrhizobium japonicum* and *Rhizobium leguminosarum*, SlyD from *Escherichia coli* and *Helicobacter pylori*, UreE from *Klebsiella aerogenes*, and Hpn and Hpn-like proteins from *Helicobacter pylori* [60].

To investigate metallocentre assembly in *Mb*NHase, I created three different altered *Mb*NHase enzymes. First, *Mb*NHase was cleaved proteolytically resulting in separated α- and β-subunits providing an enzyme that structurally mimics prokaryotic NHase enzymes. Second, a mutant, in which the entire $(\text{His})_{17}$ motif was removed (*Mb*NHase$^{\Delta 238\text{-}257}$), was constructed and expressed in the presence and absence of the Co-type (*ε*) activator protein from *Pseudonocardia thermophila* JCM 3095 (*Pt*NHase$^{\text{act}}$). Finally, a mutant was constructed in which the entire $(\text{His})_{17}$-containing insert region was deleted (*Mb*NHase$^{\Delta 219\text{-}272}$), leaving only the classical prokaryotic NHase α- and β-subunit analogs; this mutant was also expressed in the presence and absence of *Pt*NHase$^{\text{act}}$. Functional interrogation of these species provides important insight into the role of the insert region in *Mb*NHase and how functional eukaryotic NHase enzymes are activated.

2.2 Materials and Methods[61]

2.2.1 Materials

4-(2-hydroxyethyl) piperazine-1-ethanesulfonic acid(HEPES), sodium chloride, sodium phosphate dibasic, cobalt(II) chloride, acrylonitrile, acrylamide, Laemmli sample buffer, glycerol tetramethylethylenediamine (TEMED), 2-mercaptoethanol, ammonium persulfate (APS), agar, TAE buffer, DNA ladder, SYBR gold nucleic acid gel stain, DNA purification kits, kanamycin, carbenicillin, ampicillin, imidazole, gel code blue stain reagent, coomassie protein assay reagent, Amicon Ultra-15 centrifugal filter, and glycerol were purchased from the most reliable vendors. The WT *Mb*NHase plasmid, NEB turbo cell and BL21 cell were developed previously in the Holz lab. The genes expressing the *Mb*NHase$^{\Delta 238\text{-}257}$ mutant were synthesized by Genscript.

2.2.2 Preparation of LB-agar plates

Agar plates were prepared by mixing 7.5 g of LB media with 4.5 g of Agar in 300 mL of nano-pure water followed by sterilization by autoclaving. After cooling to room temperature, 300 μL of the antibiotics Kanamycin (50 mg/mL) and/or Carbenicillin (100 mg/mL) were added and the solution was thoroughly mixed. The mixture was carefully poured into sterile pETri dishes and left to solidify. The LB-agar plates were stored at 4 ºC.

2.2.3 Buffer preparation

Buffer **A1** is 50 mM NaH_2PO_4, 500 mM NaCl and 10 mM imidazole at pH 8.0. Buffer **B1** is 50 mM NaH_2PO_4, 500 mM NaCl and 500 mM imidazole at pH 8.0. Buffer **C** is 50 mM HEPES and 300 mM NaCl at pH 8.0. The protein storage buffer is 50 mM HEPES, pH 7.5. Metal analysis solutions consisted of 144 mM HCl and 32.4 mM HNO_3.

2.2.4 Gene modification

To remove histidine rich region, the β- and α-genes for *Mb*NHase$^{\Delta 238\text{-}257}$ (absent the histidine rich insert) were designed for co-expression using a gene overlap model (Figure 23).[51] A His_6 tag was introduced at the 3' terminal of the α-gene and the new β- and α-genes of *Mb*NHase$^{\Delta 238\text{-}257}$ was synthesized by Genescript with *E. coli* codon usage. The β- and α-genes of *Mb*NHase$^{\Delta 238\text{-}257}$ were then cloned into a pET28a+ plasmid between the NcoI and HindIII restriction enzyme sites.

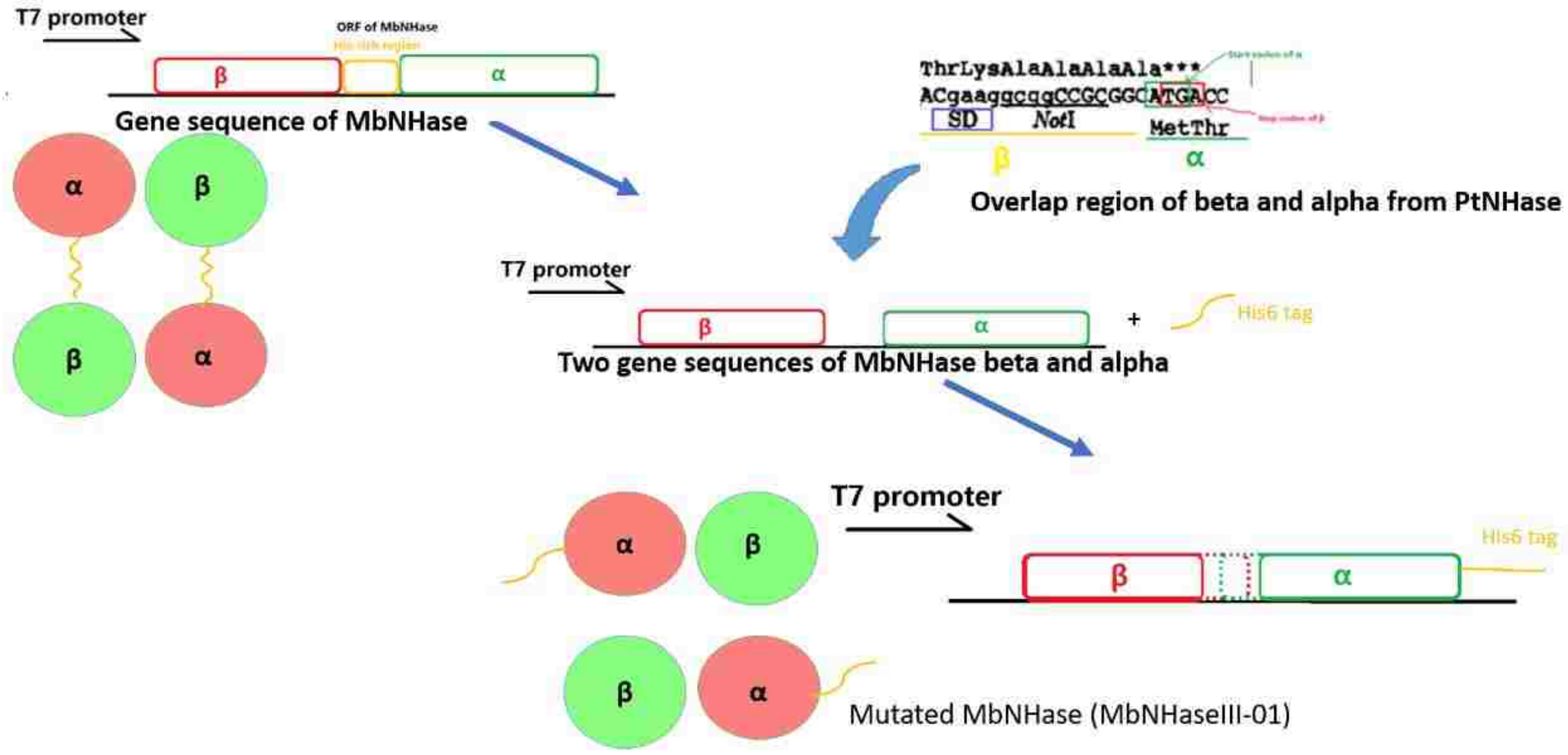

Figure 23. Gene design for *Mb*NHase$^{\Delta 238\text{-}257}$ by overlap model. The start codon of α-gene and stop codon of β- were overlapped by sharing “TG”

To remove the entire insert region, the α- and β-subunit genes where the entire insert region was deleted (*Mb*NHase$^{\Delta 219-272}$), were obtained by polymerase chain reaction (PCR) using the primers (Sense primer: CAACCATGGGTACCG AGCAGGCGGCGGTG; Anti-sense primer: CATAAGCTTTTAGTGGTGGTGGTGATGATGATCAACACGCGGCA) for the α-subunit and (Sense primer: ACG CATATG ATGCACCTGT TCA CCTACGACCTGCA; Anti-sense primer: AGTCCTCGAGTTACGCTTG CGGCGGGTTGCTA) for the β-subunit. His6 tag gene was designed at the end of antisense primer. The α-subunit gene was sub-cloned between *NcoI* and *HindIII* sites, while the β-subunit gene was sub-cloned between *NdeI* and *XhoI* sites within the pCOLADuet-1 expression vector (Novagen). The sequences were confirmed by Functional Biosciences. The plasmids containing the *Mb*NHase$^{\Delta 238-257}$ and *Mb*NHase$^{\Delta 219-272}$ deletion mutant genes were transformed into BL21 magic cells for the soluble expression of the *Mb*NHase$^{\Delta 238-257}$ and *Mb*NHase$^{\Delta 219-272}$ enzymes. Expression and purification of these deletion mutant enzymes was carried out in an identical manner to that described above for WT *Mb*NHase. [56]

2.2.5 Plasmid transformation

The WT *Mb*NHase gene within a pET21a vector, was previously cloned in the Holz lab. Autoclaved LB media was warmed to 37 ºC and 1-5 µL of a solution containing 50 ng of plasmid DNA were added into recombinant NEB Turbo *E. coli* cells and gently mixed. The mixture was incubated on ice for 30 min followed by heat shock at 42 °C for 30 sec. The mixture was then incubated on ice for 5 min, after which 950 µL of LB media was added followed by a 1 hr incubation period at 37 °C with stirring at 220 rpm after which 300μL of an NEB Turbo cell culture was spread onto an LB Agar plate with the appropriate antibiotic (Kanamycin or Carbenicillin) and incubated at 37 °C for 18 h. The plate was sealed and stored at 4 °C for 1 month. A single colony was extracted under sterile conditions and placed in 5 mL of LB media containing 5 μL of the corresponding antibiotic (1:1000). The mixture was inoculated at 37 °C and stirred at 220 rpm for 16 h. A glycerol stock was prepared by mixing 1.4 mL of this cell culture with 0.7 mL of LB media containing 50% glycerol. The culture mixture was flash-frozen and stored in -80 °C.

2.2.6 WT MbNHase expression and purification

Protein sequences for the α- and β-subunit genes of the putative WT *Mb*NHase were obtained from ORF 37534 (UniProt ID A9V2C1.1) of *M. brevicollis* and the predicted gene was synthesized by Integrated DNA Technologies, Inc. with optimized *E. coli* codon usage. This gene was cloned into the kanamycin resistant pET21a$^+$ (EMD Biosciences) expression vector to create the plasmid pSMMαβ, as previously reported [56].

A single colony was selected to inoculate separate starter cultures of 50 mL LB Miller media containing the appropriate antibiotics (pET28a+: 50 mg/mL kanamycin) and allowed to grow at 37 °C with constant shaking overnight. These cultures were used to inoculate 6 L of LB Miller media containing the appropriate antibiotics and allowed to grow at 37 °C with constant shaking until an optical density of ~0.8-1.0 at 600 nm was reached. The cultures were cooled on ice to 20 °C and induced with 0.1 mM Isopropyl-β-D-1- thiogalactopyranoside (IPTG), supplemented with 0.25 mM of $CoCl_2$, and shaken for an additional 16 hours at 20 °C.

Cells were pelleted by centrifugation at 6,370 × *g* for 10 minutes at 4 °C in a Beckman Coulter Avanti JA-10 rotor and resuspended in buffer **A** (50 mM sodium phosphate buffer, pH 7.5, containing 300 mM NaCl, 5% glycerol, and 10 mM imidazole) at a ratio of 5 mL per gram of cells. Cells were lysed by ultrasonication (Misonix Sonicator 3000) for 4 min (alternating 30 s on and 45 s off) at 21 W. Cell lysate was separated from cell debris by centrifugation in a JA-20 rotor at 31,000 × *g* at 4 °C for 20 min. Cell lysate was purified using immobilized metal affinity chromatography (IMAC; 100 mg protein/5mL column) on a GE ÄKTA Fast Protein Liquid Chromatography (FPLC) system at 4 °C. The column was washed with 50 mL of buffer **A** followed by 50 mL of buffer **A** containing additional imidazole (35 mM). The protein was eluted using a linear gradient (0-100%) of buffer **B** (50 mM NaH_2PO_4 pH 7.5, 300 mM NaCl, 10% glycerol, 525 mM imidazole) at a flow rate of 1 mL/min resulting in *Mb*NHase being eluted between 150 to 240 mM imidazole.

Fractions containing WT *Mb*NHase were pooled and concentrated to ~1 mL using an Amicon Ultra-15 (Millipore) and loaded onto a 16/60 Superdex 200 prep grade (GE Healthcare) polishing column using buffer **C** (50 mM HEPES and 300 mM NaCl at pH 8.0). Pure WT *Mb*NHase was concentrated using an Amicon Ultra-15 (Millipore) and analyzed by SDS-PAGE with a 12.5% polyacrylamide SPRINT NEXT GEL™ (Amresco). Gels were stained with Gel Code Blue (Thermo-Fisher Scientific). The protein concentration of purified WT *Mb*NHase was determined by measuring the absorbance at 280 nm on a Shimadzu UV-2450 spectrophotometer. The calculated molecular weight for the WT *Mb*NHase homodimer is 111,207 g/mol with an extinction coefficient of 143,700 cm^{-1} M^{-1}. The molecular weight is in good agreement with SDS-PAGE data [56].

2.2.7 *Mb*NHase variants expression and purification

The plasmids containing the *Mb*NHase$^{\Delta 238\text{-}257}$ and *Mb*NHase$^{\Delta 219\text{-}272}$ mutant genes were transformed into BL21 magic cells for the soluble expression of the *Mb*NHase$^{\Delta 238\text{-}257}$ and *Mb*NHase$^{\Delta 219\text{-}272}$ enzymes. Expression and purification of these mutant enzymes was carried out in an identical manner to that described above for WT *Mb*NHase [56].

The gene encoding the Co-type activator (ε) protein from *Pseudonocardia thermophila* JCM 3095 (*Pt*NHase^{act}) was synthesized by Integrated DNA Technologies, Inc. with optimized *E. coli* codon usage and cloned into the kanamycin resistant pET21a^{+} (EMD Biosciences) expression vector to create the pSPT^{act} plasmid. The pSPT^{act} plasmid was co-expressed with the previously reported pSMMαβ plasmid encoding recombinant *MbNHase* [56] that had been freshly transformed into BL21(DE3) (Stratagene) competent cells. In addition, the pSPT^{act} plasmid was co-expressed with the plasmids containing the *Mb*NHase$^{\Delta 238\text{-}257}$ and *Mb*NHase$^{\Delta 219\text{-}272}$ mutant genes in BL21 magic cells. Expression and purification of WT *Mb*NHase, *Mb*NHase$^{\Delta 238\text{-}257}$ and *Mb*NHase$^{\Delta 219\text{-}272}$ co-expressed with *Pt*NHase^{act} was carried out in an identical manner to that described above for WT *Mb*NHase. [56]

2.2.8 SDS-PAGE

Sodium dodecyl polyacrylamide gel electrophoresis (SDS-PAGE) was used to determine the size and purity of each protein. A typical gel was prepared by mixing 5 mL of acrylamide (12.5%), 6 μL of TEMED and 45 μL of APS followed by gel casting. A comb was inserted into the top of the gel, which was the allowed to polymerize over an ~15 min. period. Once cast, 95 μL of Laemmli sample buffer and 5 μL of 2-mercaptoethanol were mixed, as a loading dye, with the protein sample and heated to 90 °C for 7 min. The denatured protein was loaded in the comb site of the SDS-PAGE gel along with protein standards in lane 1, which contained conalbumin (MW:75000 Da) and aldolase (MW:158000 Da) and run at 200 V for 55 min. After electrophoresis, the resulting SDS-PAGE gel was cleaned by boiling in water three times and stained with coomassie blue.

2.2.9 Kinetic assays

The enzymatic activity of WT *Mb*NHase and each variant was determined using acrylonitrile as the substrate (acrylamide; $\Delta\varepsilon_{225} = 2.9$ mM^{-1} cm^{-1}). The rate of nitrile hydration was determined by continuously monitoring the formation of acrylamide at 225 nm using a Shimadzu UV-2450 spectrophotometer equipped with a TCC-240A temperature controlled cell holder [62]. A typical 1 mL reaction consisted of 50 mM Tris-HCl buffer pH 7.0 at 25 °C and various concentrations of acrylonitrile (0 to 450 mM). One unit (U) of *Mb*NHase activity is defined as the formation of 1 μmol of acrylamide per minute. To obtain the kinetic parameters, V_{max} and K_m, the initial velocities from at least three independent measurements were fitted to the Michaelis- Menten equation using OriginPro 9.0 (OriginLab, Northampton, MA). Kinetic data for each *Mb*NHase variant was determined more than 3 times for multiple purifications, all of which provided consistent results.

2.2.10 Inhibition assays

Butylboronic acid and phenylboronic acid were selected as inhibitors of *Mb*NHase. Inhibition assays were performed using at least four different inhibitor concentrations in 50 mM Tris-HCl buffer pH 7.0 at 25 °C. Inhibition data for *Mb*NHase enzymes were obtained on a Shimadzu UV-2600 spectrophotometer equipped with a TCC-240A temperature controlled cell holder. Inhibition constants (K_i) along with the type of inhibition was determined using Sigmaplot 12.5.

2.2.11 Metal Analysis

The metal content of WT *Mb*NHase and each variant, expressed in the presence and absence of $CoCl_2$, was determined by inductively-coupled plasma mass spectrometry (ICP-MS). For comparison purposes, the Co-type NHase from *Pseudonocardia thermophila* JCM 3095 (*Pt*NHase) was expressed and purified as previously described [27b], and the metal content determined along with a buffer control that contained no protein. All protein samples were pretreated with 1 M urea and digested with concentrated nitric acid (0.863 mL) followed by heating at 70 °C for 1 h, allowed to cool to room temperature, and then diluted to a final concentration of 5% nitric acid. Samples were submitted for analysis at the Water Quality Center in the College of Engineering at Marquette University (Milwaukee, WI, USA).

2.2.12 Electronic Absorption Spectra

Electronic absorption spectra were recorded on a Shimadzu UV-2450 spectrophotometer equipped with a TCC-240A temperature-controlled cell holder. Spectra for WT *Mb*NHase and each variant as well as *Pt*NHase were obtained at 25 °C in a 1 cm quartz cuvette in 50 mM HEPES buffer containing 300 mM NaCl, pH 8.0.

2.2.13 Homology modeling

Homology models of putative protein sequences were prepared based on a protein structure which with the highest sequence identity and structural similarities. The first step is to compare the sequence of the target protein with sequences of corresponding crystallographically characterized template proteins. The template sequence and structure provides information regarding the alpha helix and beta sheet regions allowing corresponding alpha helix and beta sheet regions of target sequence to be identified. Next, secondary structure fragments of the target protein are created for the corresponding alpha helix and beta sheet regions. The remaining regions of the target sequence, i.e. those that are not aligned with the template, are constructed by loop modeling. These secondary structure fragments are assembled into a tertiary structures by homology modelling programs and the final quaternary structure is constructed based on the three-dimensional crystal structure of template. After homology structure construction, global optimization and model assessment are performed by energy minimization.

Sequence comparison of only the α- and β-subunits of *Mb*NHase with those of *Pt*NHase revealed that these proteins are of similar length, with a sequence identity of ~29%, and exhibit no significant sequence gaps. Therefore, a homology model of the *Mb*NHase α- and β-subunits was developed using the X-ray crystal structure of *Pt*NHase (PDB code:1IRE) as the template. The YASARA homology-building program was used to construct the structural homology model of *Mb*NHase. Comparison of the energy minimized *Mb*NHase α- and β-subunit homology model to the X-ray crystal structure of *Pt*NHase, using the MatchMaker in UCSF Chimera, reveals that the *Mb*NHase α- and β-subunit homology model displays the typical dimerization and catalytic domains of *Pt*NHase with a Needleman-Wunsch score of 285 and an average RMSD of 1.129 Å over the aligned 354 Cα atom pairs.

2.3 Results and Discussions

2.3.1 Sequence alignment of MbNHase with prokaryotic NHases

The putative gene was reported to exist in several eukaryotic organisms that encodes putative NHase α- and β-subunits fused by a special insert region (Figure 24) . [18, 28] The protein encoded by *M. brevicollis* contains 495 amino acids and alignment of with the amino acid sequences of the α and β subunits from various prokaryotic NHases revealed that the N-terminus aligns with the β subunit of theseNHases (Figure 24A), while the C-terminus aligns with and has high similarity (35-45%) to the α subunits (Figure 24A). Both α and β subunits in the hypothetical *Mb*NHase are connected by an insert region containing seventeen histidines, and the C-terminus contains the signature Co-type NHase metal-binding domain (Figure 24B)[61].

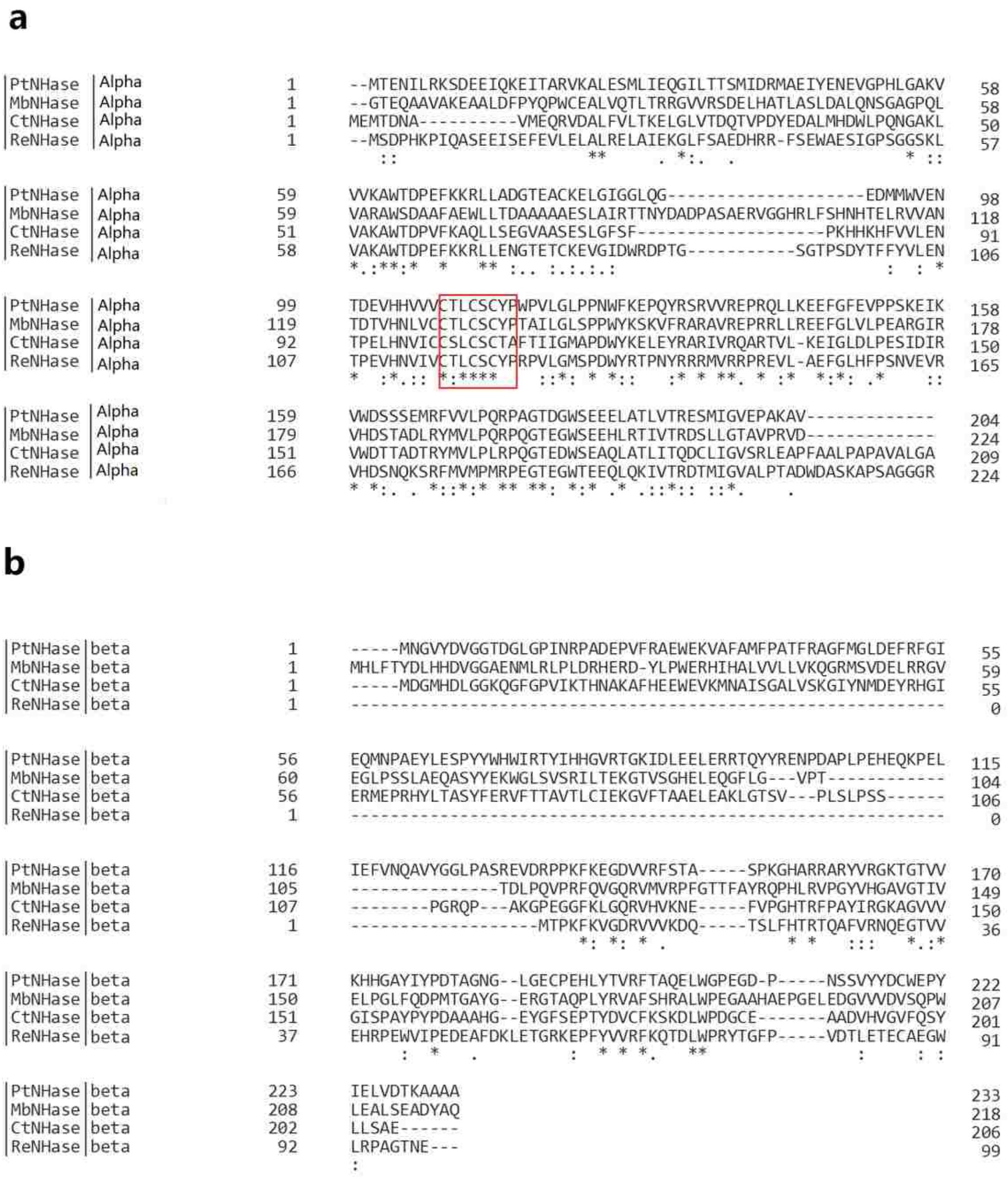

a

```
PtNHase |Alpha    1   --MTENILRKSDEEIQKEITARVKALESMLIEQGILTTSMIDRMAEIYENEVGPHLGAKV   58
MbNHase |Alpha    1   --GTEQAAVAKEAALDFPYQPWCEALVQTLTRRGVVRSDELHATLASLDALQNSGAGPQL   58
CtNHase |Alpha    1   MEMTDNA----------VMEQRVDALFVLTKELGLVTDQTVPDYEDALMHDWLPQNGAKL   50
ReNHase |Alpha    1   --MSDPHKPIQASEEISEFEVLELALRELAIEKGLFSAEDHRR-FSEWAESIGPSGGSKL   57
                         ::                   **     . *:.  .                 * ::

PtNHase |Alpha   59   VVKAWTDPEFKKRLLADGTEACKELGIGGLQG--------------------EDMMWVEN   98
MbNHase |Alpha   59   VARAWSDAAFAEWLLTDAAAAAESLAIRTTNYDADPASAERVGGHRLFSHNHTELRVVAN  118
CtNHase |Alpha   51   VAKAWTDPVFKAQLLSEGVAASESLGFSF-------------------PKHHKHFVVLEN   91
ReNHase |Alpha   58   VAKAWTDPEFKKRLLENGTETCKEVGIDWRDPTG-----------SGTPSDYTFFYVLEN  106
                      *.:**:*  *   ** :.. :.:.:.:                           :  : *

PtNHase |Alpha   99   TDEVHHVVVCTLCSCYPWPVLGLPPNWFKEPQYRSRVVREPRQLLKEEFGFEVPPSKEIK  158
MbNHase |Alpha  119   TDTVHNLVCCTLCSCYPTAILGLSPPWYKSKVFRARAVREPRRLLREEFGLVLPEARGIR  178
CtNHase |Alpha   92   TPELHNVICCSLCSCTAFTIIGMAPDWYKELEYRARIVRQARTVL-KEIGLDLPESIDIR  150
ReNHase |Alpha  107   TPEVHNVIVCTLCSCYPRPVLGMSPDWYRTPNYRRRMVRRPREVL-AEFGLHFPSNVEVR  165
                      *  :*.:: *:****    ::*: * *::   :* * **. * :*  *:*: .*    ::

PtNHase |Alpha  159   VWDSSSEMRFVVLPQRPAGTDGWSEEELATLVTRESMIGVEPAKAV-------------  204
MbNHase |Alpha  179   VHDSTADLRYMVLPQRPQGTEGWSEEHLRTIVTRDSLLGTAVPRVD-------------  224
CtNHase |Alpha  151   VWDTTADTRYMVLPLRPQGTEDWSEAQLATLITQDCLIGVSRLEAPFAALPAPAVALGA  209
ReNHase |Alpha  166   VHDSNQKSRFMVMPMRPEGTEGWTEEQLQKIVTRDTMIGVALPTADWDASKAPSAGGGR  224
                      * *:. . *::*:* ** **: *:* .* .::*:: ::*.    .
```

b

```
PtNHase |beta     1   -----MNGVYDVGGTDGLGPINRPADEPVFRAEWEKVAFAMFPATFRAGFMGLDEFRFGI   55
MbNHase |beta     1   MHLFTYDLHHDVGGAENMLRLPLDRHERD-YLPWERHIHALVVLLVKQGRMSVDELRRGV   59
CtNHase |beta     1   -----MDGMHDLGGKQGFGPVIKTHNAKAFHEEWEVKMNAISGALVSKGIYNMDEYRHGI   55
ReNHase |beta     1   ------------------------------------------------------------    0

PtNHase |beta    56   EQMNPAEYLESPYYWHWIRTYIHHGVRTGKIDLEELERRTQYYRENPDAPLPEHEQKPEL  115
MbNHase |beta    60   EGLPSSLAEQASYYEKWGLSVSRILTEKGTVSGHELEQGFLG---VPT------------  104
CtNHase |beta    56   ERMEPRHYLTASYFERVFTTAVTLCIEKGVFTAAELEAKLGTSV---PLSLPSS------  106
ReNHase |beta     1   ------------------------------------------------------------    0

PtNHase |beta   116   IEFVNQAVYGGLPASREVDRPPKFKEGDVVRFSTA-----SPKGHARRARYVRGKTGTVV  170
MbNHase |beta   105   ---------------TDLPQVPRFQVGQRVMVRPFGTTFAYRQPHLRVPGYVHGAVGTIV  149
CtNHase |beta   107   --------PGRQP---AKGPEGGFKLGQRVHVKNE-----FVPGHTRFPAYIRGKAGVVV  150
ReNHase |beta     1   -------------------MTPKFKVGDRVVVKDQ-----TSLFHTRTQAFVRNQEGTVV   36
                                             *: *: * .            * *   :::   *.:*

PtNHase |beta   171   KHHGAYIYPDTAGNG--LGECPEHLYTVRFTAQELWGPEGD-P-----NSSVYYDCWEPY  222
MbNHase |beta   150   ELPGLFQDPMTGAYG--ERGTAQPLYRVAFSHRALWPEGAAHAEPGELEDGVVVDVSQPW  207
CtNHase |beta   151   GISPAYPYPDAAAHG--EYGFSEPTYDVCFKSKDLWPDGCE-------AADVHVGVFQSY  201
ReNHase |beta    37   EHRPEWVIPEDEAFDKLETGRKEPFYVVRFKQTDLWPRYTGFP-----VDTLETECAEGW   91
                           :  *   .         :  * * *.   **               :     : :

PtNHase |beta   223   IELVDTKAAAA                                                  233
MbNHase |beta   208   LEALSEADYAQ                                                  218
CtNHase |beta   202   LLSAE------                                                  206
ReNHase |beta    92   LRPAGTNE---                                                   99
                      :
```

Figure 24. Sequence alignment of: a) α-subunits and b) β-subunits of various NHases. An “ * ” (asterisk) indicates positions which have a single, fully conserved residue; A “ : ” (colon) indicates conservation between groups of strongly similar properties - scoring > 0.5 in the Gonnet PAM 250 matrix; A “ . ” (period) indicates conservation between groups of weakly similar properties - scoring =< 0.5 in the Gonnet PAM 250 matrix. Conserved active site motifs are highlighted in red.

2.3.2 Characteristics of purified WT *Mb*NHase

*Mb*NHase was expressed in *E. coli* without accessory protein and purified by IMAC Ni-NTA column.[61] SDS-PAGE exhibits single peptide band corresponding to the α-insert region-β (55kDa).

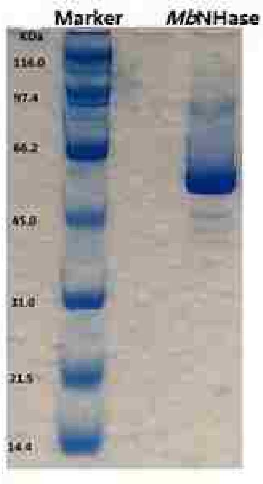

Figure 25. SDS-PAGE analysis of WT *Mb*NHase: lane 1 molecular weight standards, lane 2 purified *Mb*NHase.

Size-exclusion chromatography shows that *Mb*NHase exists primarily as an $(\alpha\beta)_2$ homodimer in solution, with a small a monomer fractions (αβ). (Figure. 26).

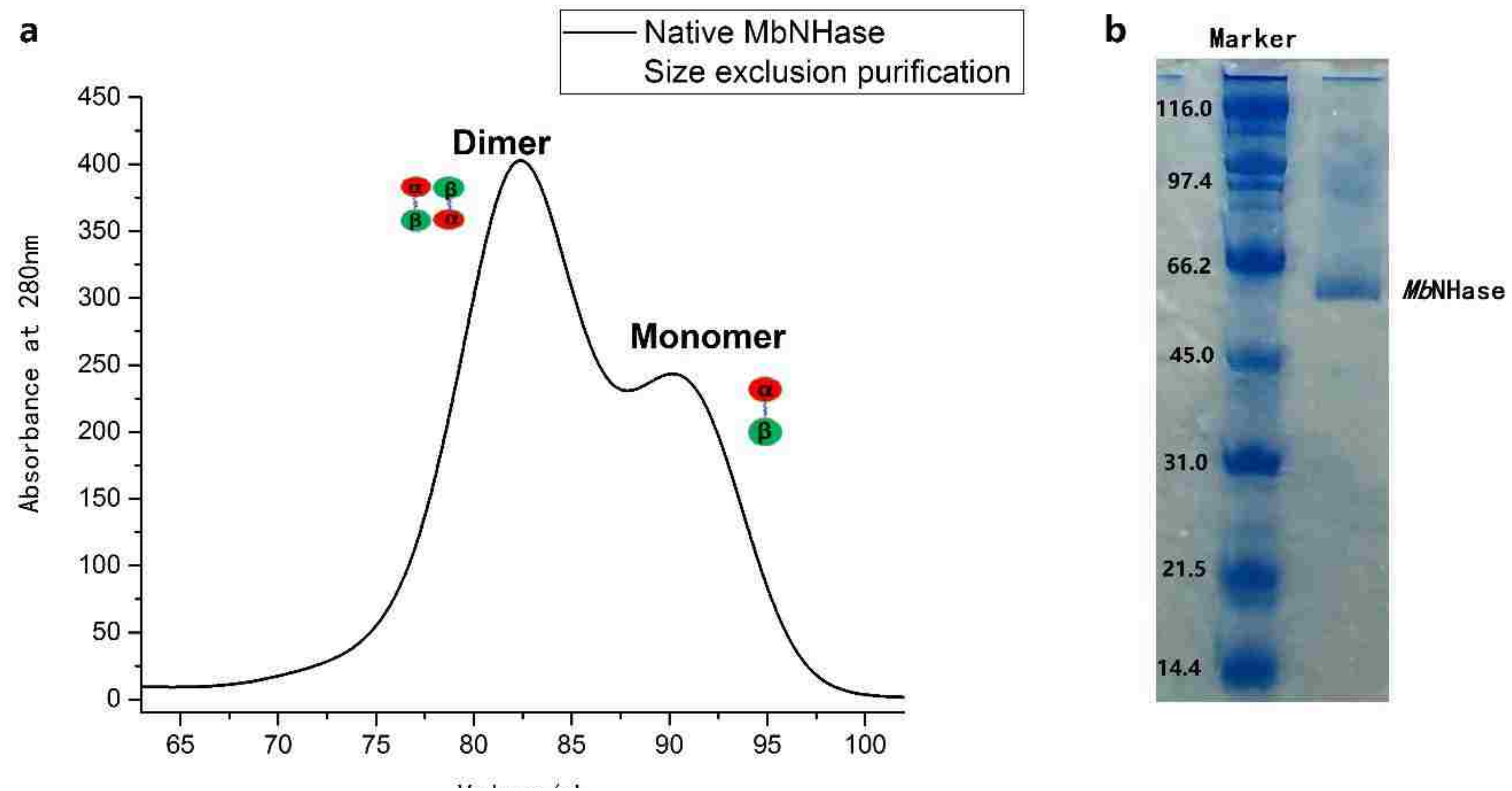

Figure 26. Size exclusion purification of WT *Mb*NHase. a) FPLC graph of size exclusion chromatography of WT *Mb*NHase; b) SDS gel of WT *Mb*NHase.

A three dimensional homology model of WT MbNHase was developed by using the X-ray crystal structure of the *Pt*NHase (PDB code: 1IRE) as a template (Figure 27a). The modeling results suggested the α- and β-subunits of *Mb*NHase and *Pt*NHase are similar. The classical "claw-setting" active site is determined at acive site, containing Co(III) ion with C400, C403, and C405 ligands(Figure 27b). The oxidation of cysteine residues at active site that due to the post translational modification was also predicted. However, the mechanism of cysteine oxidation after translation still remains to be determined. Two amide nitrogen atoms and the oxidized sulfur atoms are roughly in the same plane as the metal ion. The sulfur atom from C400 forms a coordination bond roughly perpendicular to this plane, which results in a slightly distorted square-based pyramidal geometry. On the opposite side of C400, no sixth ligand such as water was modeled but is often observed for Co-type NHase enzymes. The β-Arg56 and β-Arg167 residues were found to form second coordination sphere with active site residues.

The insert region containing histidine rich region at active site was found to be at the out sphere of αβ subunits, which is different from *Pt*NHase. The "flappy" loop of insert region could be vulnerable for the cleavage in the solution.

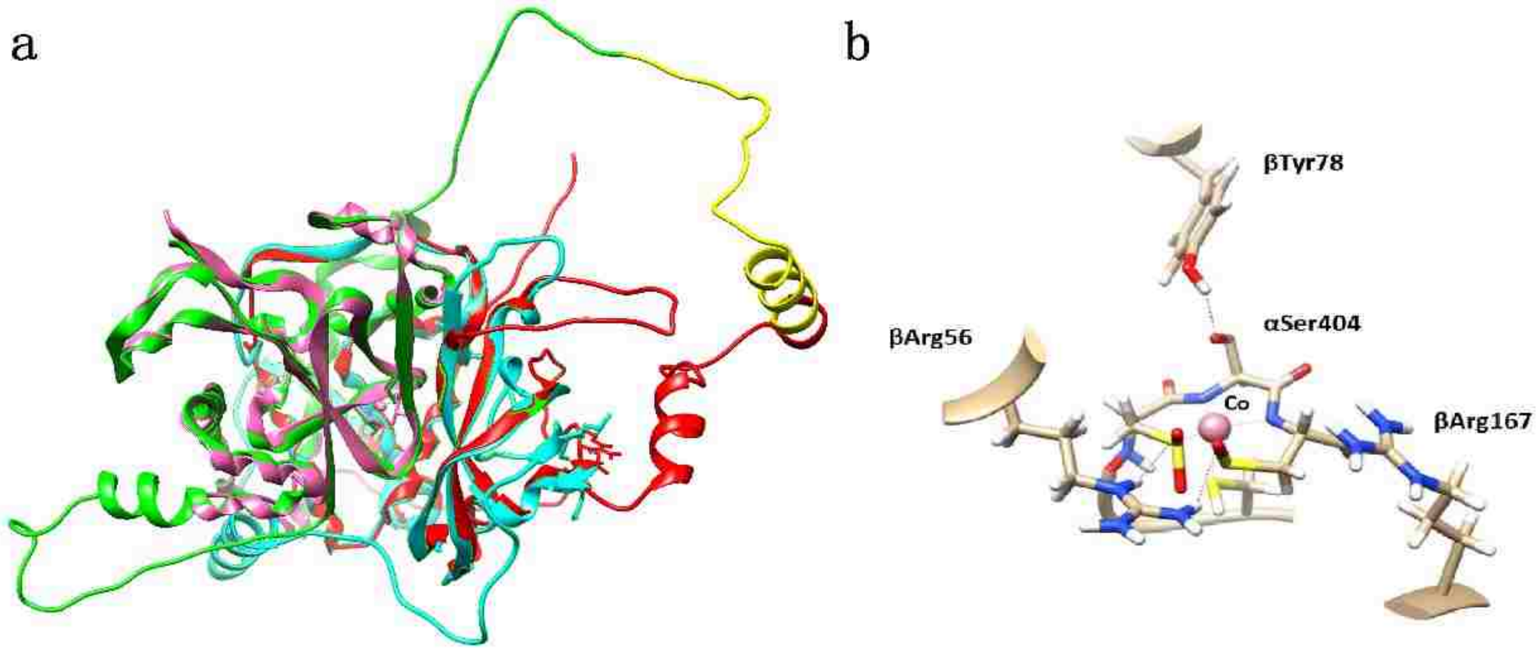

Figure 27. a) Homology model of *Mb*NHase. a) *Mb*NHase homology model for the α domain(green) and β domain(Red) overlaid with α subunit(green) and β subunit(cyan) of the *Pt*NHase X-ray crystal structure (PDB:1IRE; Green). b) The active site of *Mb*NHase derived from the homology.

The UV-Vis spectrum of *Mb*NHase was recorded in 50 mM Tris-HCl buffer, pH 7.0 at 25 °C. An intense peak at 280 nm with a shoulder at 320 nm was observed, with no other detactable absorption bands in the visible region (Figure 28). The absorption at 320 nm is characteristic of prokaryotic NHase enzymes and suggest that *Mb*NHase contains a low-spin Co(III) ion in its active site.[63] ICP-MS confirmed that *Mb*NHase binds ~1.9 equivalents of cobalt per mole of$(\alpha\beta)_2$ dimer, indicating that 0.9 equivalents of cobalt are bound per active site.

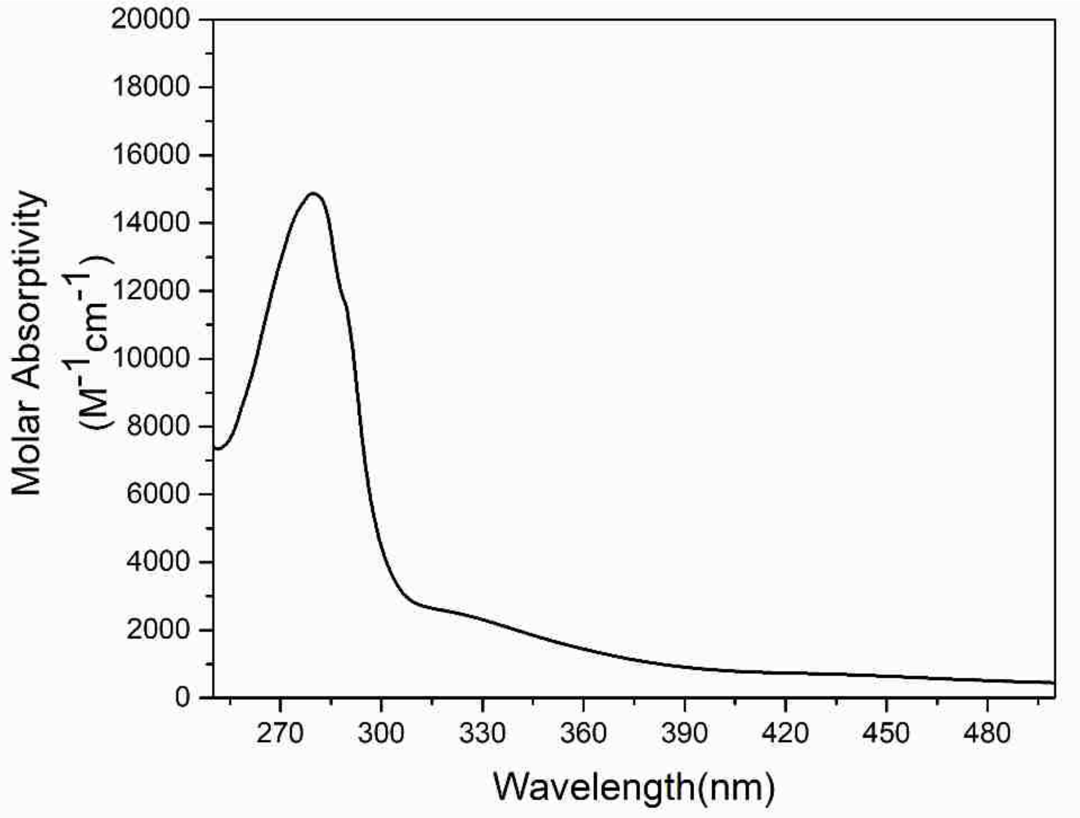

Figure 28. UV-Visible absorption spectrum of the WT *Mb*NHase

Kinetic analysis *Mb*NHase in 50 mM Tris-HCl buffer, pH 7.0 at 25 °C using acrylonitrile as the substrate indicates that *Mb*NHase does indeed possess NHase activity ($k_{cat} = 131.6 \pm 3$ s^{-1}, $K_m = 78 \pm 3$ mM) providing a catalytic efficiency k_{cat}/K_m of 1.7 s^{-1} mM^{-1} (Figure 29). Since the turnover rate is in line with other reported Co-type NHase enzymes (k_{cat} = 50 to 1,500 s^{-1}), it was hypothesized that the metal ion was properly inserted and that both active site Cys residues (Cys403 and Cys405) are properly oxidized in the absence of an activator protein, which is typically required for full NHase enzymatic activity. *Mb*NHase is also capable of hydrating benzonitrile (k_{cat} = 33 ± 1 s^{-1}, K_m=18.3 ± 0.5mM), providing a catalytic efficiency k_{cat}/K_m of 1.8 s^{-1} mM^{-1} (Figure 29). These data suggest that *Mb*NHase exhibits a higher affinity for aromatic nitrile substrates compared to aliphatic substrates, following the trend observed for most Co-type NHases.

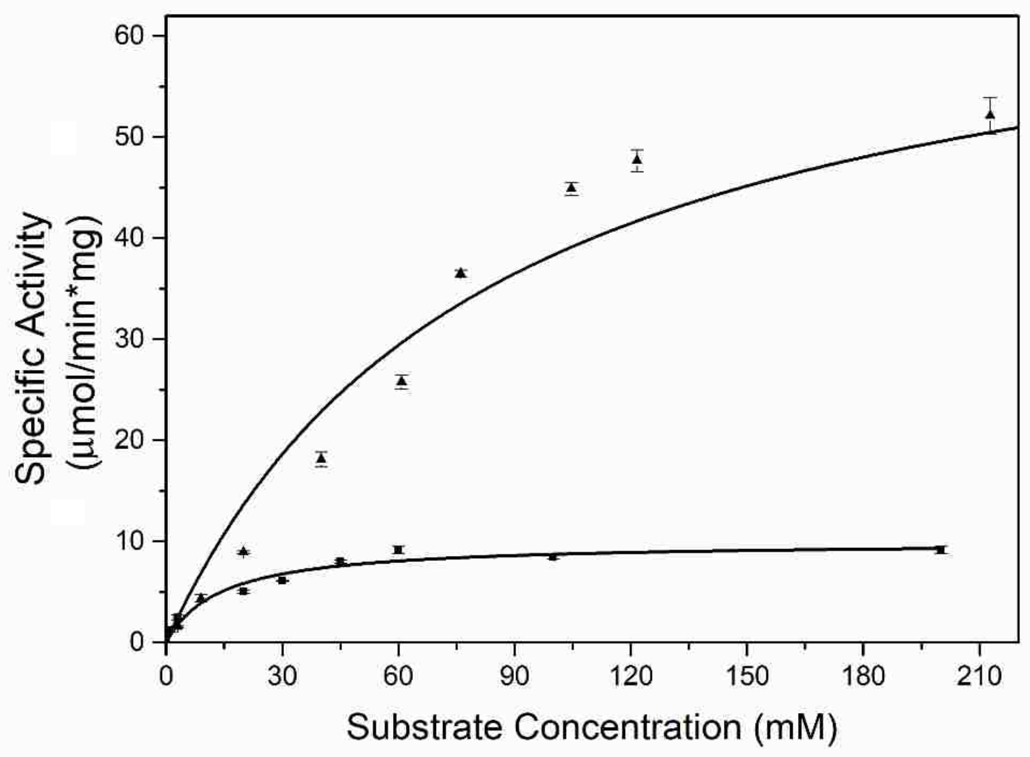

Figure 29. Michaelis-Menten assay curve of WT *Mb*NHase activity assay. Triangle: acrylonitrile; square: benzonitrile. Error bars are smaller than the symbols used.

Inspection of the reaction time course for the hydration of acrylonitrile at pH 7.0 and 25 °C by *Mb*NHase in the presence of 1-Butaneboronic acid (BuBA) and phenylboronic acid (PBA), indicate that both boronic acids function as competitive inhibitors of *Mb*NHase (Figure 30). For BuBA, the K_i is 8.1 ± 0.81 mM and K_i for PBA is 0.3 ± 0.04 mM. The smaller K_i value for PBA may be attributable to non-covalent interactions between two aromatic groups of PBA and β-Tyr-78.

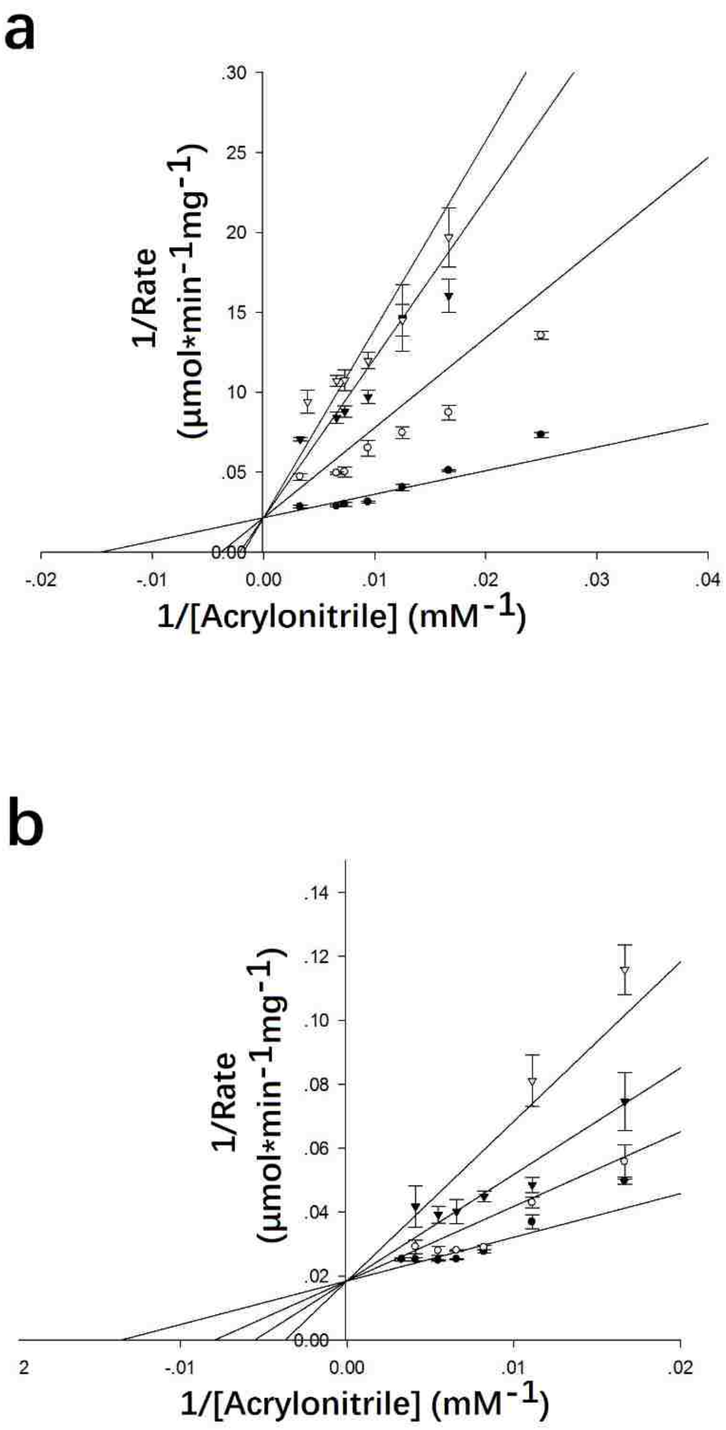

Figure 30. Inhibition assays. a) Lineweaver Burk graph of 1-Butaneboronic acid (BuBA), The solid circles represent 0mM BuBA, the hollow circles represent 23mM BuBA, solid triangle represent 47mM BuBA, hollow triangle represent 57mM BuBA. b) Lineweaver-bulk graph of phenylboronic acid (PBA). The solid circles represent 0mM PBA, the hollow circles represent 0.25mM PBA, solid triangle represent 0.51mM PBA, hollow triangle represent 0.94mM PBA

2.3.3 Proteolytic cleavage of *Mb*NHase

Storage of WT *Mb*NHase at 4°C in 50 mM Tris-HCl buffer, pH 7.0 for approximately two weeks, followed by size-exclusion chromatography, provided an *Mb*NHase enzyme with an elevated k_{cat} value of 163 ± 4 s^{-1} and a K_m value of 93 ± 15 mM. The observed increase in k_{cat} represents an ~20% increase in rate over WT *Mb*NHase with no meaningful change in K_m. Kinetic data for each *Mb*NHase variant was determined more than 3 times for multiple purifications, all of which provided constant k_{cat} values resulting in a calculated error of ± 4 s^{-1}. SDS-PAGE analysis of aged *Mb*NHase revealed two polypeptides of ~24 and ~26 kDa (Figure 31), and the size exclusion chromatography elution profile was consistent with an $\alpha_2\beta_2$ heterotetramer, identical to that observed for prokaryotic NHases.

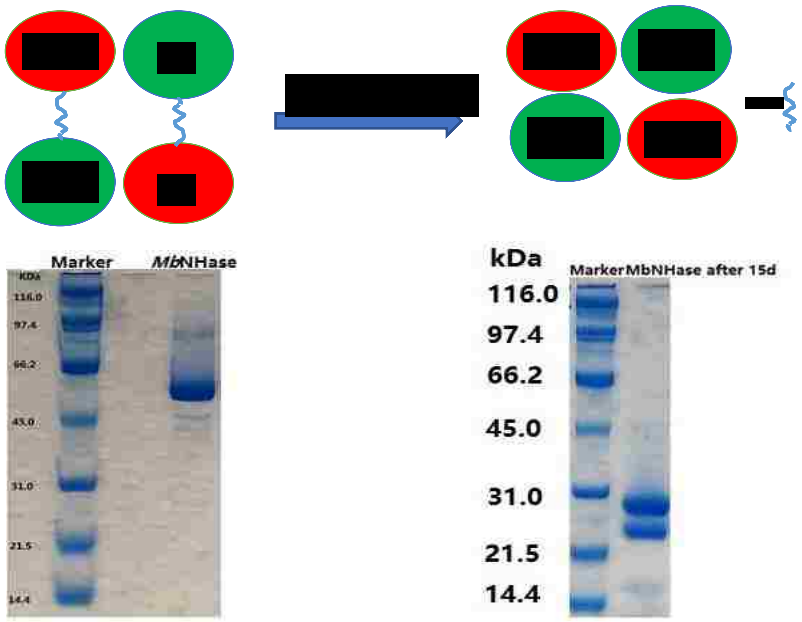

Figure 31. The SDS-PAGE of (a) WT *Mb*NHase and (b) the proteolytically cleaved *Mb*NHase enzyme.

These data indicate that the single polypeptide of freshly isolated WT *Mb*NHase, which contains fused α- and β-subunits linked by an insert region, was cleaved into separate α- and β-subunits upon ageing, likely by trace amounts of proteases.

Proteolytic cleavage was found to be inhibited by an additional gel-filtration purification step performed directly after IMAC; however, the addition of protease inhibitor cocktails, such as AEBSF, resulted in the precipitation of the protein. The addition of metal ion inhibitors such as EDTA and 1,10-phenanthroline had no effect on *Mb*NHase cleavage. The observed increase in activity for the proteolytically cleaved *Mb*NHase enzyme is perhaps due to an easing of conformational stress induced by the insert region in and around the active site, although structural characterization will be required to confirm this. Confirmation of the proteolytic cleavage of WT *Mb*NHase into separate α- and β-subunits was obtained by MALDI-TOF mass spectroscopy (Figure 32). Two masses were clearly observed at 24,848 Da and 25,530 Da, values that confirmed the SDS-PAGE estimates (Figure 31) and correspond to the α- and β-subunits of *Mb*NHase based on sequence comparison with the prototypical Co-type *Pt*NHase enzyme (Figure 24). The two MALDI-TOF MS peaks were of similar intensities, indicating a ~1:1, α:β ratio. These data are consistent with a functional $\alpha_2\beta_2$ heterotetramer, as suggested by size exclusion chromatography, and corresponds to the quaternary structure of prokaryotic NHases. Interestingly, the observed molecular masses from MALDI-TOF MS (Figure 32) suggests that a 5,226 Da peptide is lost after proteolytic cleavage, comparable to the size of the complete insert region of WT *Mb*NHase. Attempts to isolate the cleaved fragment were unsuccessful. It may be due to further cleavage of the fragment into smaller peptides by the protease contaminants.

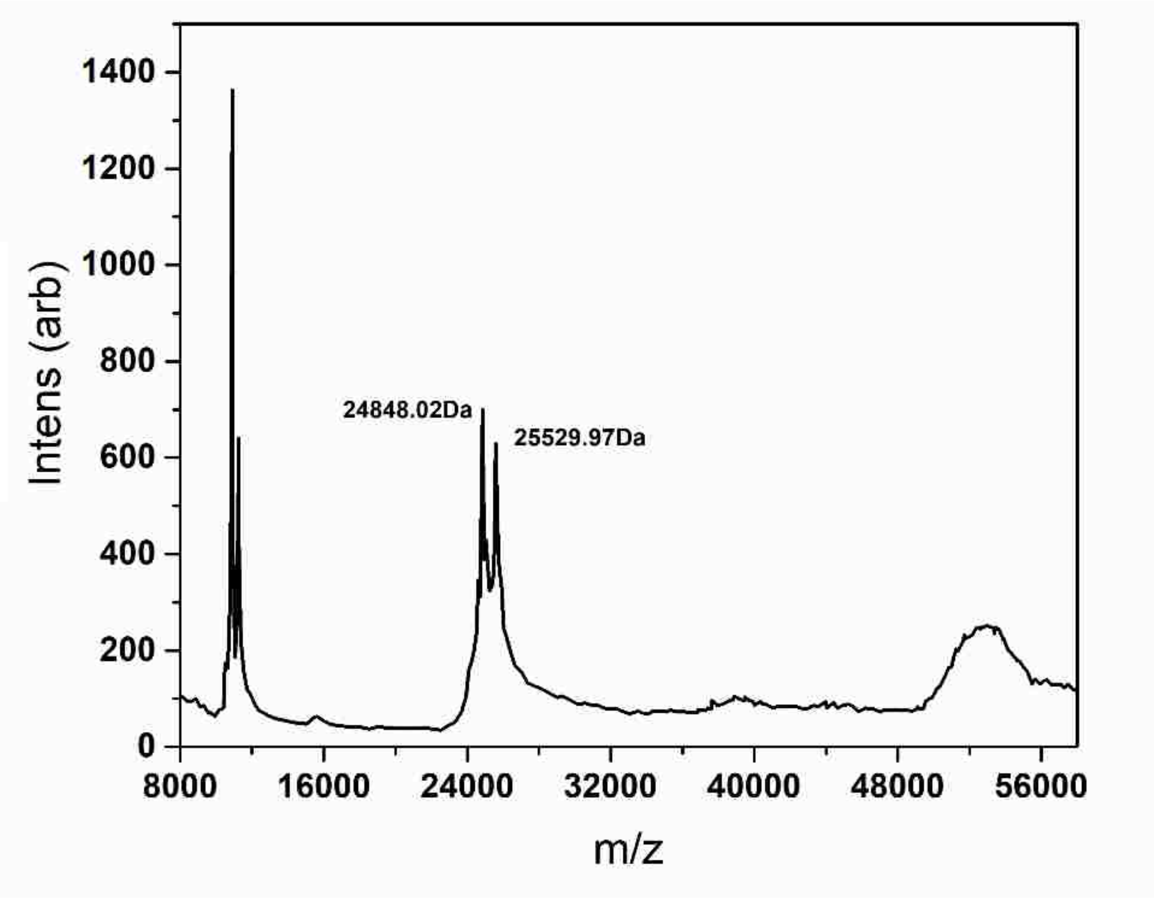

Figure 32. MALDI-TOF Mass Spectra of proteolytically cleaved *Mb*NHase revealing two peaks at 24.8 and 25.5 kDa corresponding to independent α- and β-subunits.

2.3.4 Examination of the functional role of the (His)$_{17}$ insert found between α and β-subunits of *Mb*NHase

Kinetic analyses of proteolytically cleaved *Mb*NHase provide unambiguous evidence that neither the insert region nor the (His)$_{17}$ motif is involved in the catalytic reaction of *Mb*NHase. To investigate whether either has a role in enzyme activation, *Mb*NHase$^{\Delta 238\text{-}257}$ and *Mb*NHase$^{\Delta 219\text{-}272}$ variants, for which the protein is expressed devoid of the (His)$_{17}$ motif and insert region, respectively, were characterized. SDS-PAGE analysis revealed two bands at ~25.5 and 28.5 KDa for *Mb*NHase$^{\Delta 238\text{-}257}$ while size-exclusion chromatography indicated that *Mb*NHase$^{\Delta 238\text{-}257}$ exists primarily as an $\alpha_2\beta_2$ heterotetramer with a molecular weight of ~108 kDa, like prokaryotic Co-type NHases (Figure 33).

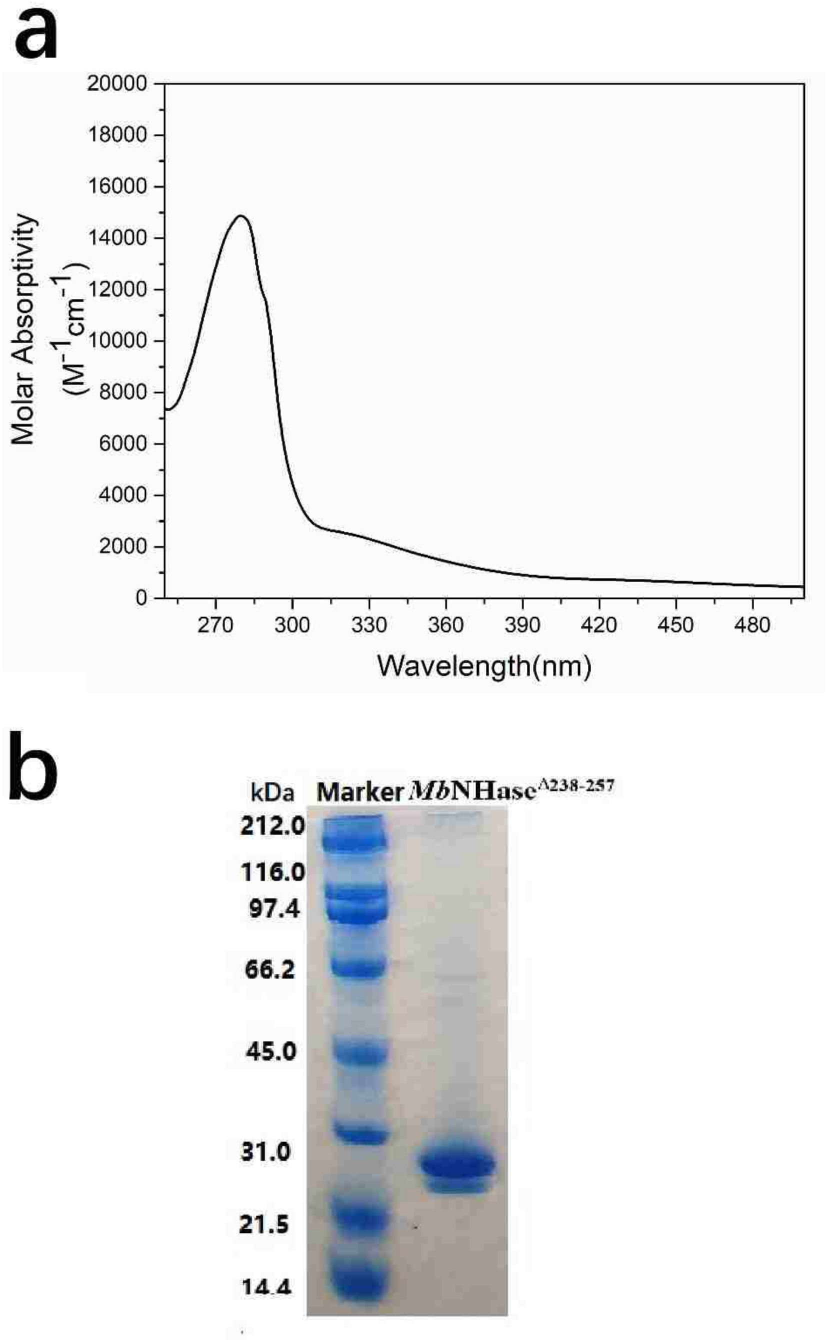

Figure 33. Purification of the *Mb*NHase$^{\Delta 238-268}$ mutant. a) size-exclusion column indicating a single peak corresponding to an $\alpha_2\beta_2$ heterotetramer; b) SDS-PAGE gel page showing that the purified α and β-subunits are two independent proteins.

Kinetic analysis of the *Mb*NHase$^{\Delta 238\text{-}257}$ (His)$_{17}$ mutant expressed in the absence and presence of *Pt*NHase^{act} were determined more than 3 times for multiple purifications yielding k_{cat} values of 71 ± 4 s^{-1} and 166 ± 5 s^{-1}, and K_m values of 104 ± 17 mM and 125 ± 17 mM, respectively, for acryonitrile. The *Mb*NHase$^{\Delta 238\text{-}257}$ (His)$_{17}$ mutant expressed in the absence and presence of *Pt*NHase^{act} contained 1.8 ± 0.1 and 2.3 ± 0.2 equivalents of cobalt per $\alpha_2\beta_2$ heterotetramer, respectively, with no other metal ions detected above the background level of <10ppb. *Mb*NHase$^{\Delta 238\text{-}257}$ expressed in either the absence or presence of *Pt*NHase^{act} exhibited the characteristic S → Co(III) LMCT band at ~320 nm (ε=2,563 M^{-1} cm^{-1}) (Figure 34), nearly identical to WT *Mb*NHase.[56] These data provide evidence that the prokaryotic *Pt*NHase^{act} protein somewhat enhances activation of *Mb*NHase but is by no means required for metal uptake or active site maturation.

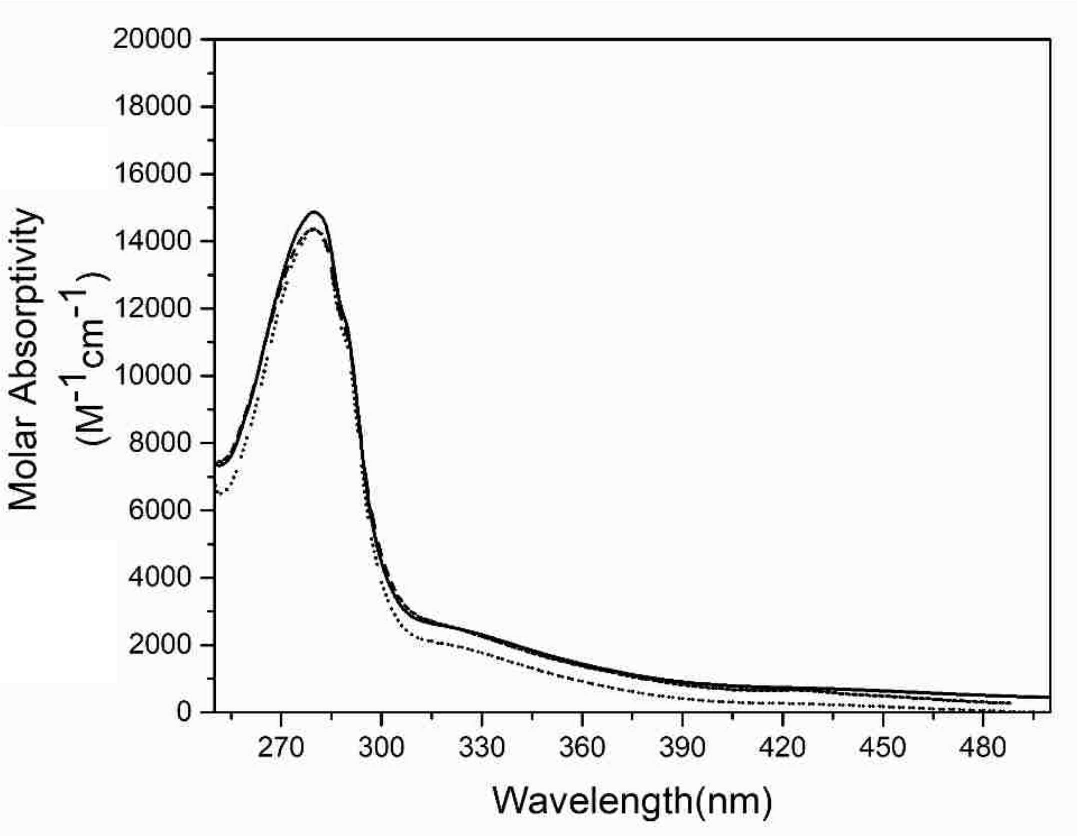

Figure 34. UV-Vis spectra of WT *Mb*NHase (solid line), *Mb*NHase$^{\Delta 238\text{-}257}$ (His)$_{17}$ mutant (dot line), and *Mb*NHase$^{\Delta 238\text{-}257}$ (His)$_{17}$ from *Pt*NHase^{act} co-expression.

2.3.5 Investigation of the insert region insert found between α and β-subunits of *Mb*NHase

The *Mb*NHase$^{\Delta 219\text{-}272}$ mutation removes the entire insert region that does not correspond to any sequence in prokaryotic NHase enzymes. Removal of this region essentially converts the eukaryotic *Mb*NHase into a prokaryotic NHase analog, allowing apposite comparison of *Mb*NHase$^{\Delta 219\text{-}272}$ and *Pt*NHase. *Mb*NHase$^{\Delta 219\text{-}272}$ expressed in the absence of *Pt*NHase^{act} exhibited two bands on SDS-PAGE at ~25.5 and ~26.5 kDa. Size-exclusion chromatography indicated that *Mb*NHase$^{\Delta 219\text{-}272}$ exists primarily as an $\alpha_2\beta_2$ heterotetramer with a molecular weight of ~104 kDa, indistinguishable from proteolytically cleaved WT *Mb*NHase and prokaryotic Co-type NHases. Surprisingly, co-expression of *Mb*NHase$^{\Delta 219\text{-}272}$ in the presence of *Pt*NHase^{act} yielded a single band at ~52 kDa on SDS-PAGE. Attempts to separate the α- and β-subunits with 8M urea, 1M dichlorodiphenyltrichloroethane (DDT) or SDS at 95 °C for 10 min, were unsuccessful (Figure 35).

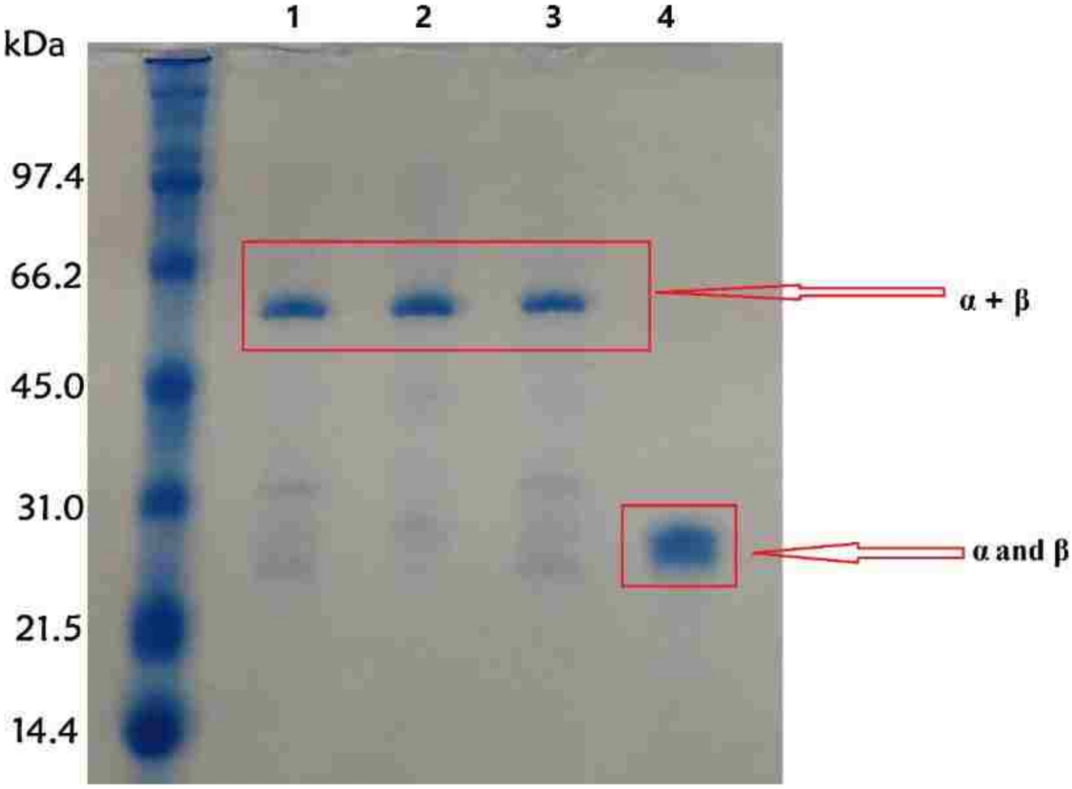

Figure 35. SDS-PAGE gel of *Mb*NHase$^{\Delta 219\text{-}272}$. Column 1: *Mb*NHase$^{\Delta 219\text{-}272}$ from activator co-expression; Column 2: *Mb*NHase$^{\Delta 219\text{-}272}$ from *Pt*NHase activator co-expression treated by 8mM Urea; Column 3: *Mb*NHase$^{\Delta 219\text{-}272}$ from activator co-expression treated by 8M urea and 1M DDT; Column 4: *Mb*NHase$^{\Delta 219\text{-}272}$ without activator.

Kinetic analysis of *Mb*NHase$^{\Delta 219\text{-}272}$ expressed in the absence and presence of *Pt*NHase^{act} provided k_{cat} values of 75 ± 8 s^{-1} and 117 ± 10 s^{-1}, respectively, for acrylonitrile (Table 1).

Table 1. Kinetic constants for the wild-type and mutant *Mb*NHases[a]

	k_{cat} (s^{-1})	K_m (mM)	k_{cat}/K_m (s^{-1}mM^{-1})	Metal Content
Wild-type[b]	131 ± 3	83 ± 10	1.6	1.8 ± 0.1
Cleaved	163 ± 4	93 ± 15	1.8	1.9 ± 0.1
Δ238-257	71 ± 4	104 ± 17	0.7	1.8 ± 0.1
Δ238-257 + *Pt*NHase^{act}	166 ± 5	125 ± 17	1.3	2.3 ± 0.2
Δ219-272	75 ± 8	73 ± 14	1.0	1.7 ± 0.1
Δ219-272 + *Pt*NHase^{act}	117 ± 10	149 ± 23	0.8	1.7 ± 0.1

[a] Acrylonitrile was used as the substrate. [b] Reference [56].

It was observed that the *Mb*NHase$^{\Delta 219\text{-}272}$ mutant is not particularly stable and loses > 95% of its activity over the course of a few hours, indicating that the insert region plays a role, probably structural, in stabilizing the functional protein.

The *Mb*NHase$^{\Delta 219\text{-}272}$ mutant contained 1.7 ± 0.1 equivalents of cobalt per $\alpha_2\beta_2$ heterotetramer, irrespective of the co-expression of *Pt*NHase^{act}, a value close to that obtained for WT *Mb*NHase (Table 1). UV-Vis spectra of *Mb*NHase$^{\Delta 219\text{-}272}$ expressed in the absence or presence of *Pt*NHase^{act} were indistinguishable from each other and WT *Mb*NHase (Figure 36).

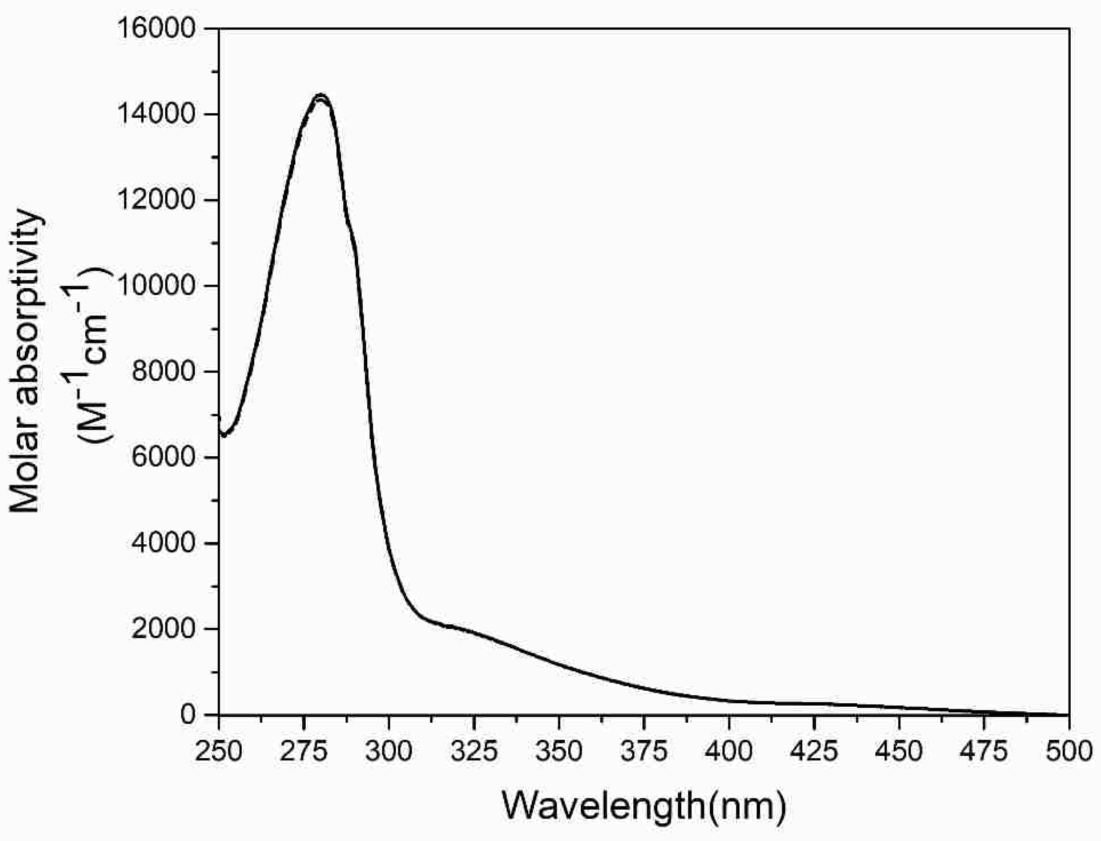

Figure 36. UV-Vis spectra of WT *Mb*NHase (solid line), *Mb*NHase$^{\Delta 219\text{-}272}$ mutant (dot line), and *Mb*NHase$^{\Delta 219\text{-}272}$ from *Pt*NHaseact co-expression.

Therefore, *Mb*NHase$^{\Delta 219\text{-}272}$ binds a full complement of Co(III) ions without the assistance of an (ε) protein, indicating that the insert region is not required for metal ion binding or active site maturation.

2.4 Summary

Characterization of the constructs described herein of the eukaryotic NHase from *Monosiga brevicollis* confirm that *Mb*NHase does not require an NHase activator protein or the *E. coli* chaperone proteins GroEL/ES for metallocentre assembly, including metal ion insertion and active site post-translational maturation. In addition, these data indicate that the $(His)_{17}$ region found within the insert that links the α- and β-subunits is not required for metal ion incorporation or active site maturation. The fact that the proteolytically cleaved WT *Mb*NHase enzyme and the *Mb*NHase$^{\Delta 238\text{-}257}$ variant each exhibit a modest increase in activity compared to WT *Mb*NHase, suggests that the insert region likely induces a structural strain on the active site that has a limiting effect on the catalytic rate of hydration. The lack of the need for either an intrinsic or an extrinsic activator polypeptide for *Mb*NHase is in stark contrast to the absolute requirement for an activator for assembly and activation of the otherwise similar prokaryotic NHases. The pertinent and related outstanding questions are, "How can the *Mb*NHase metallocentre self-assemble and self-activate?" and, "Why do the prokaryotic NHase metallocenters require activators for assembly and activation?" The genetically engineered functional constructs of *Mb*NHase described herein represent an important new tool with which to further address these questions using structural and spectroscopic methods.

CHAPTER THREE: INVESTIGATING THE REACTION OF A UNIQUE METALLO- DEHALOGENASE FROM *PSEUDOMANAS SP. CTN-3*

3.1 Introduction

Chlorothalonil (TPN; 2,4,5,6-tetrachloroiso-phtalonitrile) is one of the most commonly used fungicides in the US with more than five million kilograms sprayed on crops and fruits each year [37-38, 64]. TPN has a low solubility in water (100 mg L^{-1}) but it is strongly absorbed in soil, particularly soil with high organic matter such as those found in aquatic environments. It is stable to hydrolysis between pH 5 to 7, with a half-life of 30 to 60 days, and it can remain in soil for over a year [65]. It is highly toxic to fish and aquatic species including birds and invertebrates and is emerging as a major environmental issue [66]. TPN is also a human skin and eye irritant that can cause severe gastrointestinal issues. Animal studies involving mice have shown that TPN can cause kidney cancer so it has been classified by the U.S. Environmental Protection Agency (EPA) as a probable human carcinogen [37]. Given the widespread use of TPN and its toxicity, its biodegradation and environmental clean-up has become a topic of significant importance [41].

Characterized pathways for biological dehalogenation of organics include oxidative, reductive, and thiolytic mechanisms [42-44]. However, selective partial dehalogenation of TPN can also be catalyzed by a hydrolytic process that converts TPN to 4-hydroxytrichloroisophthalo-nitrile (4-OH-TPN) and chloride (Figure 22) [45, 66b]. Several bacterial strains harbor a gene that has been shown to be responsible for TPN dehalogenation [67]. All gene products exhibit remarkable (>95%) identity and require Zn(II) as a cofactor for catalysis (Figure 37).

```
Rhodococus sp. XF-6   ------------------MPPGCSGLCSFVGLTMPLKFSGVLCASLLTITLSVAAHATELILDFNKVQMRSQQLAPGV 60
Rhodococus sp. XF-3  -------------------MPPGCSGLCSFVGLTMPLKFSGVLCASLLTITLSVAAHATELILDFNKVQMRSQQLAPGV 60
Pseudomonas sp. CTN-3-------------------MPPGCSGLCSFVGLTMPLKFSGVLCASLLTITLSVAAHATELILDFNKVQMRSQQLAPGV 60
Rhodococcus sp. XF-8--------------------MPPGCSGLCSFVGLTMPLKFSGVLCASLLTITLSVAAHATELILDFNKVQMRSQQLAPGV 60
Rhizobium sp. CTN-15-----------------------------------MPLKFSGVLCASLLTITLSVAAHATELILDFNKVQMRSQQLAPGV 45
Ochrobactrum lupini------------------------------------MPLKFSGVLCASLLTITLSVAAHATELILDFNKVQMRSQQLAPGV 45
Bordetella sp. CTN-10----------------------------------MPLKFSGVLCASLLTITLSVAAHATELILDFNKVQMRSQQLAPGV 45
Ochrobactrum sp. CTN-11--------------------------------MPLKFLGVLCASLLTITLSVAAHATELILDFNKVQMRSQQLAPGV 45
Caulobacter sp. CTN-14---------------------------------MPLKFLGVLCASLLTITLSVAAHATELILDFNKVQMRSQQLAPGV 45
                                                       *********************************************

Rhodococus sp. XF-6---------------------YAHLPADSAELNAKGGVAGTSGGLIVGTRGAMLIETMLNRRLFDQVQALAKKEALGLPLL 120
Rhodococus sp. XF-3---------------------YAHLPADSAELNAKGGVAGTSGGLIVGTRGAMLIETMLNRRLFDQVQALAKKEALGLPLL 120
Pseudomonas sp. CTN-3-------------------YAHLPADSAELNAKGGVAGTSGGLIVGTRGAMLIETMLNRRLFDQVQALAKKEALGLPLL 120
Rhodococcus sp. XF-8--------------------YAHLPADSAELNAKGGVAGTSGGLIVGTRGAMLIETMLNRRLFDQVQALAKKEALGLPLL 120
Rhizobium sp. CTN-15--------------------YAHLPADSAELNAKGGVAGTSGGLIVGTRGAMLIETMLNRRLFDQVQALAKKEALGLPLL 105
Ochrobactrum lupini---------------------YAHLPADSAELNAKGGVAGTSGGLIVGTRGAMLIETMLNRRLFDQVQALAKKEALGLPLL 105
Bordetella sp. CTN-10-------------------YAHLPADSAELNAKGGVAGTSGGLIVGTRGAMLIETMLNRRLFDQVQALTKKEALGLPLL 105
Ochrobactrum sp. CTN-11-----------------YAHLPADSAELNAKGGVAGTSGGLIVGTRGAMLIETMLNRRLFDQVQALAKKEALGLPLL 105
Caulobacter sp. CTN-14------------------YAHLPADSAELNAKGGVAGTSGGLIVGTRGAMLIETMLNRRLFDQVQALAKKEALGLPLL 105
                                        *************************************************:**********

Rhodococus sp. XF-6---------------------YAVNTSYHGDHSYGNMYLKAPTRVIQSTKTRDYVDGHLADDKAFMVKNFGAGRGVEQITA 180
Rhodococus sp. XF-3---------------------YAVNTSYHGDHSYGNMYLKAPTRVIQSTKTRDYVDGHLADDKAFMVKNFGAGRGVEQITA 180
Pseudomonas sp. CTN-3-------------------YAVNTSYHGDHSYGNMYLKAPTRVIQSTKTRDYVDGHLADDKAFMVKNFGAGRGVEQITA 180
Rhodococcus sp. XF-8--------------------YAVNTSYHGDHSYGNMYLKAPTRVIQSTKTRDYVDGHLADDKAFMMKNFGAGRGVEQITA 180
Rhizobium sp. CTN-15--------------------YAVNTSYHGDHSYGNMYLKAPTRVIQSTKTRDYVDGHLADDKAFMVKNFGAGRGVEQITA 165
Ochrobactrum lupini---------------------YAVNTSYHGDHSYGNMYLKAPTRVIQSTKTRDYVDGHLADDKAFMVKNFGAGRGVEQITA 165
Bordetella sp. CTN-10-------------------YAVNTSYHGDHSYGNMYLKAPTRVIQSTKTRDYVDGHLADDKAFMVKNFGAGRGVEQITA 165
Ochrobactrum sp. CTN-11-----------------YAVNTSYHGDHSYGNMYLKAPTRVIQSTKTRDYVDGHLADDKAFMVKNFGAGRGVEQITA 165
Caulobacter sp. CTN-14------------------YAVNTSYHGDHSYGNMYLKAPTRVIQSTKTRDYVDGHLADDKAFMVKNFGAGRGVEQITA 165
                                        *********************************************:**************

Rhodococus sp. XF-6---------------------RTGDILVPPGGRVSVDLGGKTVEIIDFGFAQTGGDLFVWEPQSKVMWTGNAVVASKPALP 240
Rhodococus sp. XF-3---------------------RTGDILVPPGGRVSVDLGGKTVEIIDFGFAQTGGDLFVWEPQSKVMWTGNAVVASKPALP 240
Pseudomonas sp. CTN-3-------------------RTGDILVPPGGRVSVDLGGKTVEIIDFGFAQTGGDLFVWEPQSKVMWTGNAVVASKPALP 240
Rhodococcus sp. XF-8--------------------RTGDILVPPGGRVSVDLGGKTVEIIDFGFAQTGGDLFVWEPQSKVMWTGNPVVASKPALP 240
Rhizobium sp. CTN-15--------------------RTGDILVPPGGRVSVDLGGKTVEIIDFGFAQTGGDLFVWEPQSKVMWTGNAVVASKPALP 225
Ochrobactrum lupini---------------------RTGDILVPPGGRVSVDLGGKTVEIIDFGFAQTGGDLFVWEPQSKVMWTGNSVVASKPALP 225
Bordetella sp. CTN-10-------------------RTGDILVPPGGRVSVDLGGKTVEIIDFGFAQTGGDLFVWEPQSKVMWTGNAVVASKPALP 225
Ochrobactrum sp. CTN-11-----------------RTGDILVPPGGRVSVDLGGKTVEIIDFGFAQTGGDLFVWEPQSKVMWTGNAVVASKPALP 225
Caulobacter sp. CTN-14------------------RTGDILVPPGGRVSVDLGGKTVEIIDFGFAQTGGDLFVWEPQSKVMWTGNSVVASKPALP 225
                                        ************************************************** *********

Rhodococus sp. XF-6---------------------WLLDGKLVETLATLQKVYDFLPPDATIVPGHGVPMAREGLRWHLDYLAAVQAGVKDALAR 300
Rhodococus sp. XF-3---------------------WLLDGKLVETLATLQKVYDFLPPDATIVPGHGVPMAREGLRWHLDYLAAVQAGVKDALAR 300
Pseudomonas sp. CTN-3-------------------WLLDGKLVETLATLQKVYDFLPPDATIVPGHGVPMAREGLRWHLDYLAAVQAGVKDALAR 300
Rhodococcus sp. XF-8--------------------WLLDGKLVETLATLQKVYDFLPPDATIVPGHGVPMAREGLRWHLDYLAAVQAGVKDALAR 300
Rhizobium sp. CTN-15--------------------WLLDGKLVETLATLQKVYDFLPPDATIVPGHGVPMAREGLRWHLDYLAAVQAGVKDALAR 285
Ochrobactrum lupini---------------------WLLDGKLVETLATLQKVYDFLPPDATIVPGHGVPMAREGLRWHLDYLAAVQAGVKDALAR 285
Bordetella sp. CTN-10-------------------WLLDGKLVETLATLQKVYDFLPPDATIVPGHGVPMAREGLRWHLDYLAAVQAGVKDALAR 285
Ochrobactrum sp. CTN-11-----------------WLLDGKLVETLATLQKVYDFLPPDATIVPGHGVPMAREGLRWHLDYLAAVQAGVKDALAR 285
Caulobacter sp. CTN-14------------------WLLDGKLVETLATLQKVYDFLPPDATIVPGHGVPMAREGLRWHLDYLAAVQAGVKDALAR 285
                                        ** *********************************************************

Rhodococus sp. XF-6---------------------------------------KLSLEQTVTELKMPEFRGYVLFDWVHPDLNVPAAYKDLAARP 342
Rhodococus sp. XF-3---------------------------------------KLSLEQTVTELKMPEFRGYVLFDWVHPDLNVPAAYKDLAARI 342
Pseudomonas sp. CTN-3-------------------------------------KLSLEQTVTELKMPEFRGYVLFDWVHPDLNVPAAY------- 335
Rhodococcus sp. XF-8--------------------------------------KLSLEQTVTELKMPEFRGYVLFDWVHPDLNVPAAYKDLAARP 342
Rhizobium sp. CTN-15--------------------------------------KLSLEQTVTELKMPEFRGYVLFDWVHPDLNVPAAYKDLAARP 327
Ochrobactrum lupini---------------------------------------KLSLEQTVTELKMPEFRGYVLFDWVHPDLNVPAAYKDLAARP 327
Bordetella sp. CTN-10-------------------------------------KLSLEQTVTELKMPEFRGYVLFDWVHPDLNVPAAYKDLAARP 327
Ochrobactrum sp. CTN-11-----------------------------------KLSLEQTVTELKMPEFRGYVLFDWVHPDLNVPAAYKDLAARP 327
Caulobacter sp. CTN-14------------------------------------KLSLEQTVTELKMPEFRGYVLFDWVHPDLNVPAAYKDLAARP 327
                                                          ***********************************
```

Figure 37. Chd sequence alignments from nine selective bacteria species obtained from *Uniport*. yellow: proposed active site motif.

The best characterized enzyme within this group is the chlorothalonil (TPN) dehalogenase from *pseudomonas sp*. CTN-3 (Chd, EC:3.8.1.2) [66b, 68]. Chd contains a conserved Zn(II)-binding domain similar to enzymes in the metallo-β-lactamase superfamily and was proposed to be monomeric in solution [66b]. At least two His residues (H128 and H157) along with three Asp (D45, D130, and D184), a Ser (S126) and a Trp (W241) were reported to be catalytically essential based on site-directed mutagenesis studies. In addition, it was reported that the Zn(II) ions associated with Chd could be substituted with Cd(II), Co(II), Ca(II), or Mn(II) and provide active or even hyperactive enzymes [68]. While the initial biological characterization of Chd has provided some insight into how molecular structure controls enzyme function, the mechanism of action remains entirely unknown.

Herein a new continuous spectrophotometric assay was reported for Chd that has allowed the detection of a Chd reaction intermediate using stopped-flow spectroscopy with TPN as the substrate. From these stopped-flow data, along with metal binding and kinetic studies including pH and solvent isotope effect studies, the first catalytic mechanism for Chd was proposed.

3.2 Materials and Methods

3.2.1 Materials

Synthesized genes and primers were purchased from Genscript (Piscataway, NJ 08854). All other chemicals were purchased from commercial sources and were of the highest quality available

3.3.2 Pseudomonas sp. CTN-3 chlorothalonil dehalogenase (Chd) plasmid construction

Chd sequences were obtained by BLAST search using Uniprot (Uniport ID: C9EBR5). Proposed active site motifs for Chd were identified based on the metallo-β-lactamase superfamily. The predicted gene was synthesized with optimized *E. coli* codon usage by Genscript Inc (Piscataway, NJ 08854). A polyhistidine (His_6) affinity tag was engineered onto the C-terminus with a TEV cleavage site using Phusion DNA polymerase (New England Biolabs) and subcloned into a $pET28a^+$ (EMD Biosciences) expression vector. The sequence was confirmed using automated DNA sequencing at *Functional Biosciences* (Madison, WI).

3.2.3 Expression and Purification of Chd

The Chd plasmid was freshly transformed into BL21(DE3) competent cells (Stratagene), and a single colony was used to inoculate 50 ml of LB-Miller culture containing 50 μg/mL kanamycin with shaking overnight at 37 °C. This culture was used to inoculate a 1 L culture and the cells were grown at 37 °C until the OD_{600nm} reached 0.8-1.0. The culture was cooled on ice, induced with 0.1 mM isopropyl β-D-1-thiogalactopyranoside (IPTG) supplemented with 0.05 mM $ZnCl_2$, and expressed at 25 °C for 16 hours.

Cells were harvested by centrifugation at 6370 x *g* and 4 °C for 10 min in a Beckman Coulter Avanti JA-10 rotor. Cell pellets were resuspended in 20 mM Tris-HCl buffer containing 50 mM NaCl and 25 mM imidazole at a ratio of 5 ml per gram of cells, then sonicated for 4 min (30 s on 45 s off) at 21W using a

Misonix sonicator 3000. The crude extract was obtained after centrifugation in a JA-20 rotor at 31,000 x *g* and 4 °C for 20 min.

Crude extracts of Chd (100 mg) were loaded onto a 5 ml Ni-NTA (nitrilotriacetic acid) Superflow Cartridge (Qiagen) for immobilized metal affinity chromatography (IMAC) using an ÄKTA FPLC P-960. The column was washed with 50 mL of 20 mM Tris-HCl buffer containing 50 mM NaCl and 25 mM imidazole, followed by 50 mL of 20 mM Tris-HCl buffer containing 50 mM NaCl and 75 mM imidazole. The protein was eluted using a linear imidazole gradient (75 to 500 mM) at a flow rate of 2 mL/min. Active protein fractions were pooled and concentrated using 50 mM Tris buffer containing 1 mM EDTA with an Amicon Ultra-15 10,000 MWCO centrifugal filter unit (Millipore) resulting in ~12 mg/L of soluble Chd-His$_6$.

The His$_6$-tag was removed by treating His$_6$-tagged Chd with His$_6$-tagged TEV protease (EC 3.4.22.44) for 16 h at 4 ˚C in 50 mM Tris, pH 8.0. Cleaved protein was concentrated with a Centricon (15,000-MW cutoff; Amicon) to 3 mL and loaded on IMAC to remove the remaining cleaved His$_6$-tag, uncut protein and the His$_6$-tagged TEV protease, while the flow through containing Chd was collected and washed with 50 mM HEPES buffer containing 10% glycerol at pH 7.0. Purified protein samples were analyzed by SDS-PAGE with a 12.5% polyacrylamide SPRINT NEXT GEL™ (Amresco). Gels were stained with Gel Code Blue (Thermo-Fisher Scientific). Protein concentration of crude extracts was determined using a Coomassie (Bradford) Protein Assay Kit (Pierce) and pure protein by measuring the absorbance at 280 nm with a Shimadzu UV-2450 spectrophotometer equipped with a TCC-240A temperature-controlled cell holder.

Theoretical molecular weights and protein extinction coefficients were calculated with the ExPASy compute pI/Mw tool. The molecular weight for the Chd was 36,107 g/mol with an extinction coefficient of 42,525 cm^{-1} M^{-1}. These molecular weights are in good agreement with SDS-PAGE.

3.2.4 Chd Spectrophotometric Assay

The enzymatic activity of Chd towards TPN was measured using a Shimadzu UV-2450 spectrophotometer equipped with a TCC-240A temperature-controlled cell holder in 1 mL quartz cuvettes. A 1 mL reaction consisted of 50 mM HEPES buffer, pH 7.0 at 25 °C and various concentrations of TPN. The rate of TPN dehalogenation was determined by continuously monitoring the formation of 4-OH-chlorothalonil at 345 nm ($\Delta\varepsilon_{345} = 3.5$ $mM^{-1}cm^{-1}$). (Figure 38) Data analysis was performed using OriginPro 9.0 (OriginLab, Northampton, MA). The kinetic constants V_{max} and K_m were calculated by fitting these data to the Michaelis-Menten equation. One unit of enzyme activity was defined as the amount of enzyme that catalyzed the production of 1 μmol of the TPN minute at 25 °C.

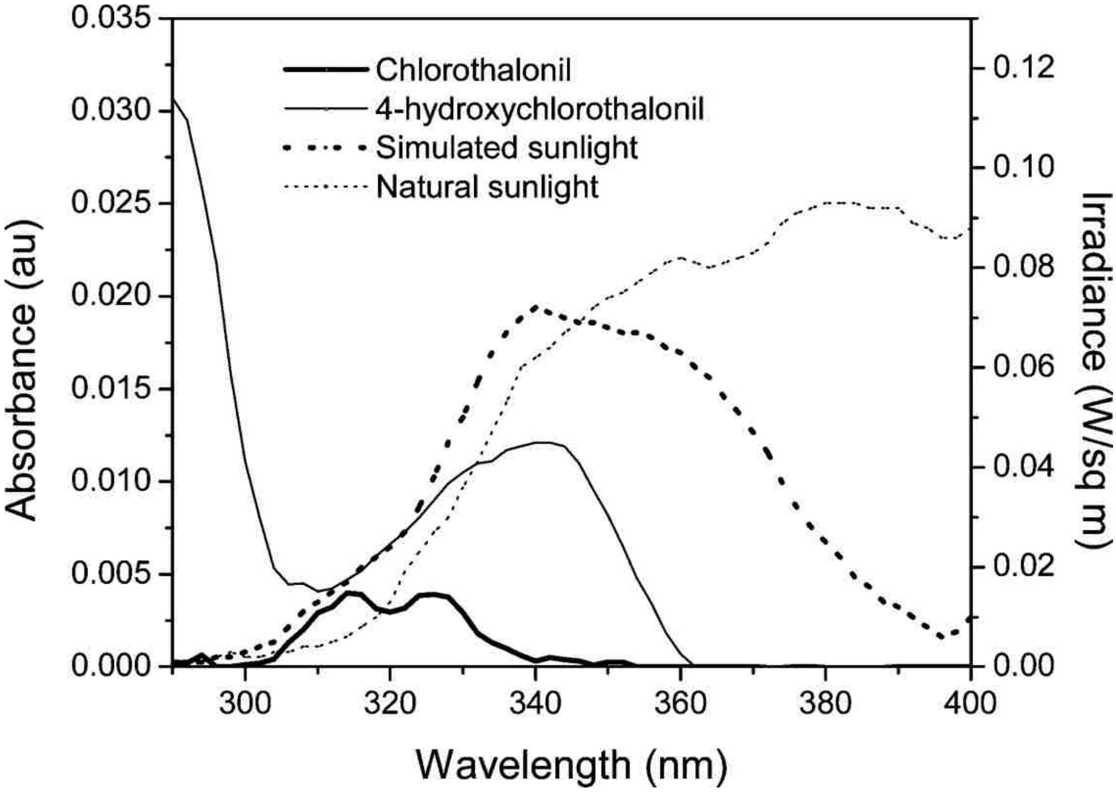

Figure 38. The UV-Vis absorption spectra of TPN and 4-OH-TPN (2μM).

3.2.5 Metal Analysis

As purified enzyme samples of Chd were digested with concentrated nitric acid at 70 °C for 10 minutes and then cooled to room temperature. These samples were diluted to 5 ml total volume with deionized water to give a final nitric acid concentration of 5% and were filtered using 0.2 μm Supor membrane syringe filters (Pall). A nitric acid blank was also prepared. The samples were analyzed using inductively coupled atomic emission spectroscopy (*ICP-AES*) at the Water Quality Center in the College of Engineering at Marquette University (Milwaukee, WI, USA).

3.2.6 Apo-Enzyme Preparation and Zn(II) Kd Determination

Apo-Chd was obtained by incubating as purified enzyme in a 15 mM 1,10-Phenanthroline/40 mM EDTA solution under anaerobic condition for ~24h. The metal chelators were removed via a PD-Minitrap G10 desalting column followed by dialysis using a Slide-A-Lyzer dialysis cassette for 16 h with Chelex 100 treated 50 mM HEPES at pH 7.0. Titration of Zn(II) into apo Chd was performed on a Shimadzu UV-2450 spectrophotometer equipped with a TCC-240A temperature-controlled cell holder in 1 mL quartz cuvettes in 50 mM HEPES buffer, pH 7.0 at 25 °C. The rate of hydrolysis of TPN (0.25 mM) was monitored as a function of [Zn(II)].

3.2.7 pH Profiles

The enzymatic activity of Chd at pH values between 4.0 and 10.2 were measured using TPN as the substrate. The concentration of each buffer used was 50 mM and the following buffers were used: borate (pH 8.50-10.50); Tris HCl (pH 7.00-8.50); HEPES (pH 6.8-7.2); MOPS (pH 6.50-7.00); MES (pH 5.50-6.50); acetate (pH 3.23-5.50). No additional Zn(II) was included in any of the buffers listed above pH 8.50. The kinetic parameters k_{cat}, K_{m} and k_{cat}/K_{m}, were determined using 8-12 different substrate concentrations ranging from 0.2-10.0 times the observed K_{m} value at each pH studied. Kinetic parameters and fits to the kinetic curves were obtained using OriginPro 9.0 (OriginLab, Northampton, MA).

3.2.8 Solvent Isotope effect

All buffers were prepared from a freshly opened bottles of 99.9% [^{2}H]

H_2O and CH_3OH (Aldrich). The buffers used in the preparation of all deuterated buffers were in the anhydrous form. The pH of each buffer used was adjusted by the addition of NaOD or DCl (both 99%+ deuterium content; Acros Organics, Geel, Belgium) and corrected for deuteration by adding 0.4 to the reading of the pH electrode.[21]

3.2.9 Stopped-flow experiment

Chd activity towards TPN was examined in triplicate using a single mixing Applied Photophysics SX-20 stopped-flow UV-vis spectrophotometer with a 20 μm cell. Chd activity was monitored at 345 nm by acquiring stopped-flow data from 0.005 to 1 second at 4 ºC using 10 μM enzyme and 250 μM TPN in deuterated 50 mM acetate buffer pH 5.0. All data were fit using OriginPro 9.0 (OriginLab, Northampton, MA).

3.2.10 TPN Electron Density Calculation

The structures of TPN was drew by *Gaussian view 5.0.8* software. The bond length and entire structure were optimized by DFT calculations at ground state (basis set: 3-21G), carrying out electron density distribution of free TPN by Gaussian 9-win.

3.3 Results and Discussions

3.3.1 Protein Expression and Purification

The gene from *pseudomanas sp. CTN-3* that encodes for Chd was synthesized with optimized E. coli codon usage that includes a polyhistidine (His6) affinity tag coupled to a TEV protease cleavage site engineered onto the C-terminus. 12 mg/L of soluble Chd enzyme was routinely obtained after purification. SDS gel page revealed a single polypeptide band at ~36 kDa (Figure 39), consistent with previous studies [66b, 68]. Size-exclusion chromatography indicated that Chd exists primarily as a dimer (~72 kDa) in solution in 50 mM HEPES buffer, pH 7.0, at 25 °C. Steady-state kinetic analysis of the product returned a kcat value of 24 ± 2 s-1 and a Km value of 110 ± 30 μM in 50 mM HEPES buffer, pH 7.0, at 25 °C.

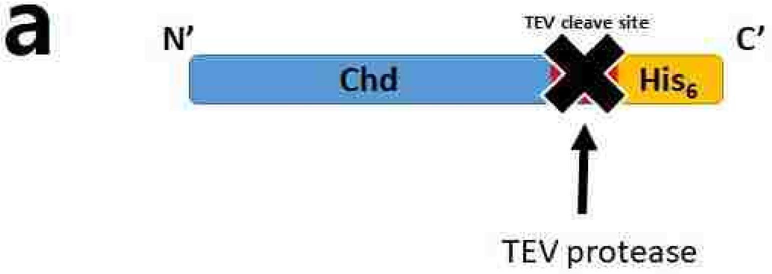

Protein sequence of Chd-His_6

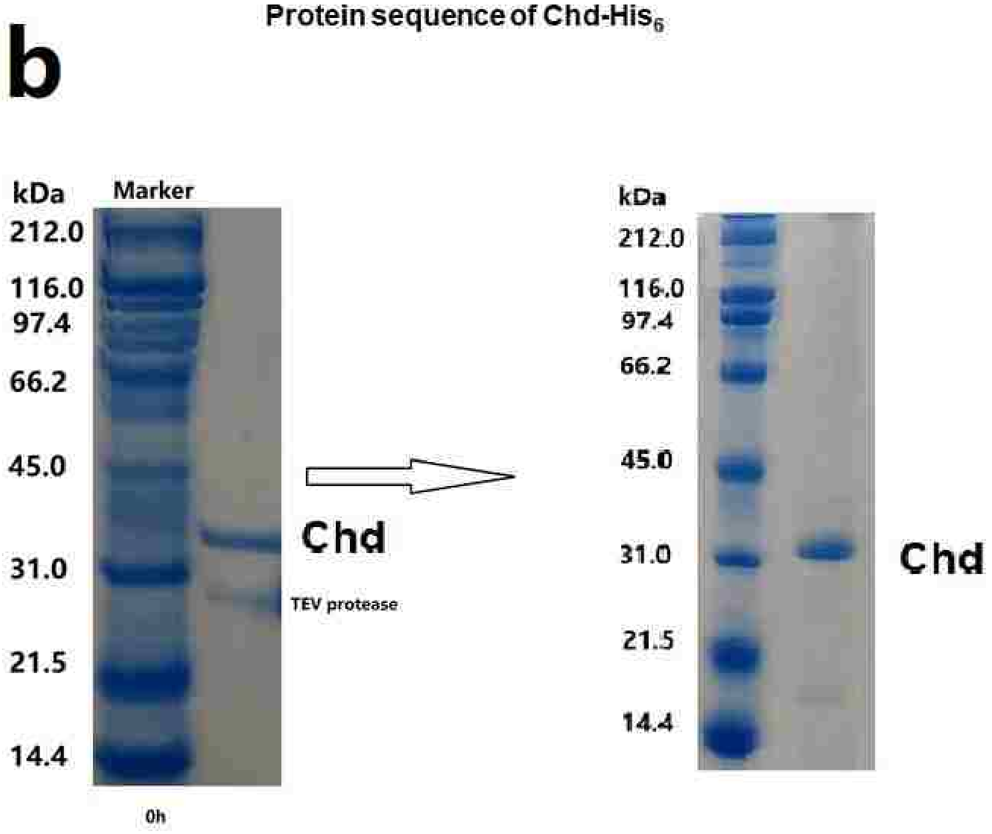

Chd-His_6 cleavage by TEV protease.

Figure 39. TEV treatment and Chd purification. SDS gel shows single band at ~36kDa size.

3.3.2 Spectrophotometric Enzymatic Assay

A new continuous spectrophotometric enzymatic assay for Chd was developed by directly detecting 4-OH-chlorothalonil, the product of TPN hydrolysis by Chd, at 345 nm ($\varepsilon_{345} = 3500 M^{-1}cm^{-1}$). This region contains no detectable substrate absorption [65]. All kinetic data were recorded on a temperature-controlled Shimadzu UV-2450 spectrophotometer in 50 mM HEPES buffer, pH 7.0, at 25 °C, over a 60 s time period. Plots of the initial rate of hydrolysis of various concentrations of TPN were fit to the Michaelis-Menten equation, which provide a k_{cat} value of 24 ± 2 s^{-1} and a K_m value of 110 ± 30 μM.

3.3.3 Metal Binding Properties of Chd

The intrinsic dissociation constant (K_d) was determined by titrating apo-Chd at pH 7.0 in 50 mM HEPES buffer at 25 °C with $Zn(II)_{aq}$ and monitoring the catalytic activity as a function of [Zn(II)]. K_d, and the number of binding sites, p, were determined by fitting these titration data to equation 1 [69], where r, the binding function, is defined by the fractionation saturation f_a and number of binding sites (equation 2) [70].

$$\mathrm{r} = \mathrm{pC}_S/(\mathrm{K}_d + \mathrm{C}_S) \qquad \text{(Eq. 1)}$$

$$r = f_a p \qquad \text{(Eq. 2)}$$

Where C_s is the concentration of free Zn(II),which was calculated from the total concertation of zinc added to the reaction (C_{TS}) by equation 3 [71] where C_A is the total molar concentration of enzyme (0.25 μM).

$$C_{TS} = C_S + rC_A \qquad \text{(Eq. 3)}$$

These data were plotted as *r* vs. [Zn(II)] (Figure 40).

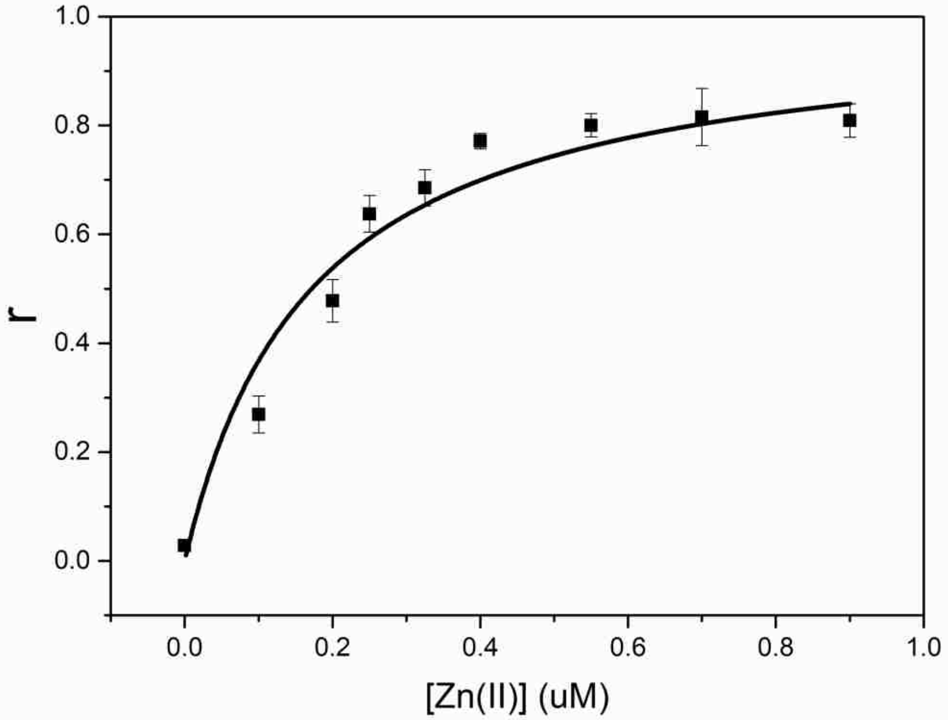

Figure 40. Zn titration to Apo Chd by spectrophotometric methods at pH=7, providing p values of ~1 and K_d values of 0.17 ± 0.01. Each data point was obtained triplicate by 1 mL reaction consisted of 50 mM HEPES buffer at pH 7.0 at 25 °C, 0.25 mM chlorothalonil, and various concentrations of metal ions.

These data are plotted as *r* vs. [Zn(II)] in Figure 40. The best fits indicated a single Zn(II) binding site (p = 1.03 ± 0.01) with an intrinsic K_d value of 0.17 ± 0.01 μM. These data are consistent with inductively coupled atomic emission spectroscopy (*ICP-AES*) data obtained on as purified Chd, which revealed that ~0.9 equivalent zinc bind tightly to Chd per monomer.

3.3.4 pH Dependence of the Kinetic Parameters

The kinetic parameters K_{m}, k_{cat}, and $k_{\mathrm{cat}}/K_{\mathrm{m}}$ were determined as a function of pH using TPN as the substrate. Chd was found to exhibit a bell-shaped curve for plots of activity *vs*. pH over the pH range 4 to 10. The maximum catalytic activity occurred in the range of pH 6.5 to 9.2. Log(k_{cat}) and log($k_{\mathrm{cat}}/K_{\mathrm{m}}$) were fit to equations 4 and 5 [72], respectively, where: k'_{cat} is the theoretical maximal velocity; $k'_{\mathrm{cat}}/K'_{\mathrm{m}}$ is the theoretical maximal catalytic efficiency; K_{ES1} is the ionization constant of the ES complex, which affects the acidic side of the pH curve while K_{ES2} reflects the basic side; and K_{E1} and K_{E2} are ionization constants for an acidic and basic group, respectively, on the free enzyme or free substrate.

$$\log k_{cat} = \log(\frac{k'_{kcat}}{1+10^{pK_{ES1}-pH}+10^{pH-pK_{ES2}-pH}}) \qquad \text{(Eq.4)}$$

$$\log k_{cat}/K_m = \log(\frac{(\frac{k'_{cat}}{K'_m})}{1+10^{pK_{E1}-pH}+10^{pH-pK_{E2}}}) \qquad \text{(Eq.5)}$$

Inspection of a plot of log(K_{m}) *vs*. pH (Figure 41) reveals that K_{m} exhibits a broad minimum over pH 5.5 to 7.5. A plot of log(k_{cat}) *vs*. pH provided a bell-shaped curve that was fit to equation 4 providing a pK_{ES1} value of 5.4 ± 0.2, a pK_{ES2} value of 9.9 ± 0.1, and a k'_{cat} value of 24 ± 2 $\mathrm{s^{-1}}$. Similarly, plots of log($k_{\mathrm{cat}}/K_{\mathrm{m}}$) *vs*. pH were fit to equation 5 providing a pK_{E1} value of 5.4 ± 0.3, a pK_{E2} value of 9.5 ± 0.1, and a $k'_{\mathrm{cat}}/K'_{\mathrm{m}}$ value of 220 ± 10 $\mathrm{s^{-1}mM^{-1}}$ (Figure 41). The goodness of the fits to the kinetic data ($R^2 = 0.98$) indicates that the dependence of the kinetic parameters on pH are consistent with the proposed model for hydrolysis.

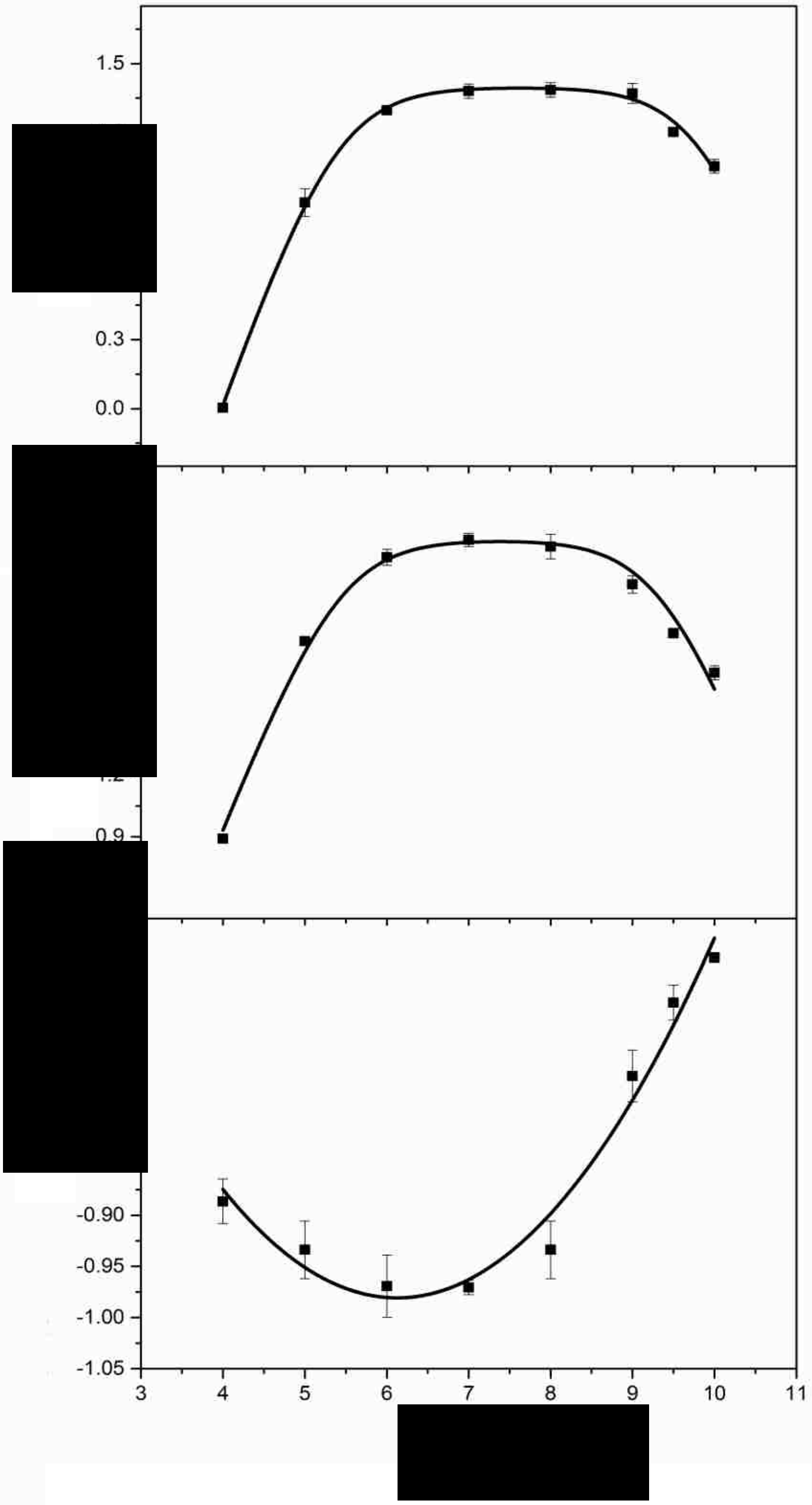

[redacted]

[redacted]

[redacted]

[redacted]

Figure 41. pH-dependence of the kinetic parameters for dechlorination of chlorothalonil by Chd between pH 4.0 and 10.0. Each data point was obtained triplicate by 1 mL reaction consisted of 50 mM HEPES buffer at various pH at 25 °C, 0.25 mM chlorothalonil. The pH dependence of Log k_{cat} fit to Equation 2, and the pH dependence of Log k_{cat}/K_m fit to Equation 3. The pH vs Log Km exhibited "V" shape with polynomial curve. Error bars are smaller than the symbols used.

3.3.5 Solvent Isotope Effect Studies

k_{cat} for TPN was measured, at several ratios of D_2O (^2H_2O):^1H_2O and the results are plotted in Figure 42 as atom fraction of deuterium *vs*. V_n/V_0, where V_n is the observed velocity at n fraction of deuterium and V_0 is the observed velocity in 100 % ^1H_2O. Proton inventories and fractionation factors were obtained by fitting the experimental values for V_n/V_0 to equations derived from the Gross-Butler equation (equation 6)[73], where υ_t is the number of protons transferred in the transition-state, while υ_R is the number of protons transferred in reactant state, and ϕ is the fractionation factor.

$$V_n/V_0 = \frac{\prod_j^{v_t}(1-n+n\phi_i^T)}{\prod_j^{v_R}(1-n+n\phi_i^R)} \qquad \text{(Eq. 6)}$$

Fitting revealed a linear relationship ($\upsilon_t = 1$, $\upsilon_R = 0$), indicating that one proton is transferred in the transition-state when $\phi_R = 1$ (equation 7) [74], where the experimental ϕ_T value is 0.17 while the theoretical value of ϕ_T is 0.18 ($R^2 = 0.99$) (Figure 42).

$$V_n = V_0 * (1 - n + \phi_T * n) \qquad \text{(Eq.7)}$$

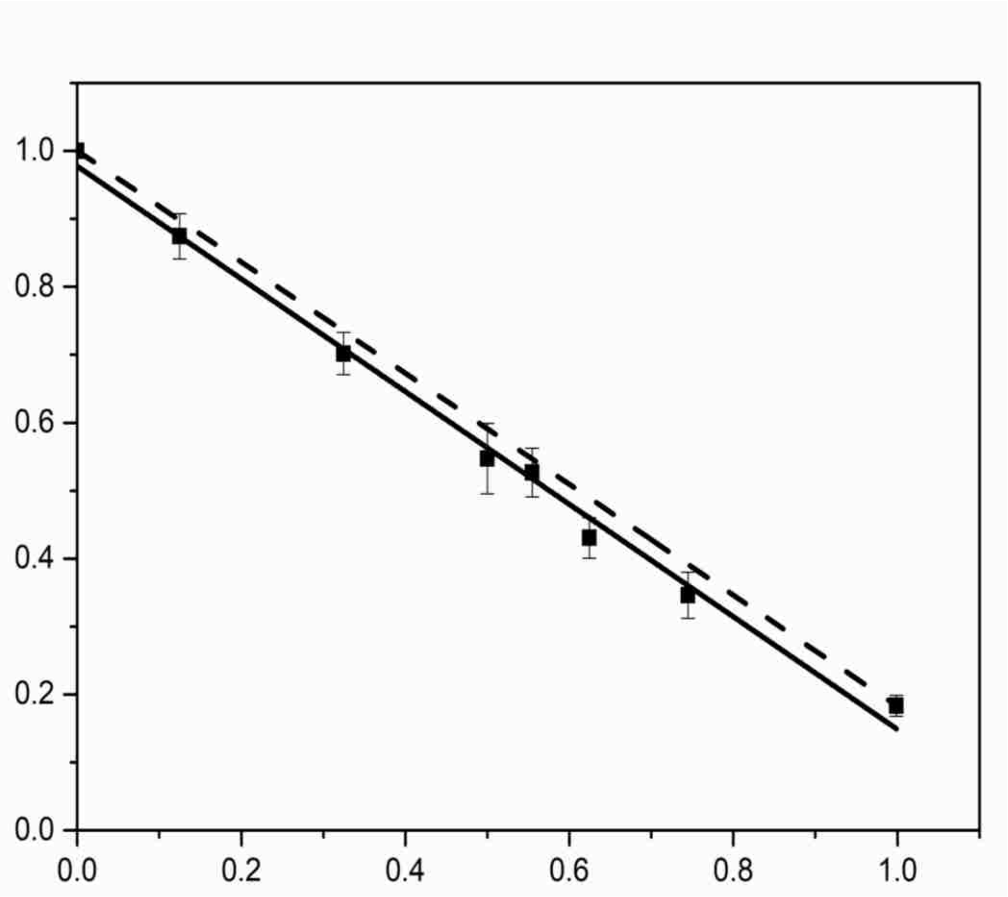

[redacted]

[redacted]

Figure 42. graph of V_n/V_0 vs atom fraction of deuterium for Chd at pH 7.0. Each data point was obtained triplicate by 1 mL reaction consisted of 50 mM HEPES buffer under different ratio of D_2O/H_2O at 25 °C, 0.25 mM chlorothalonil. Solid line: Data fitting by linear equation; Dash line: Direct fit to Equation 4 with fractionation $\phi_R=1$, $\phi_T=0.18$. Error bars are smaller than the symbols used.

Calculation of the partial solvent isotope effect provides an alternative way to determine the number of protons transferred in the transition-state [21]. At $n = 0.5$, the theoretical solvent isotope effect for a process involving N protons can be estimated using equation 8, a generalization of equations 6 & 7 of Schowen and coworkers [75], where V_1, V_0, $V_{0.5}$ are the specific activities at 100% D_2O, 0% D_2O, and 50% D_2O, respectively:

$$V_{0.5}/V_1 = \left[(1 - n_{0.5})(V_{0.5}/V_1)^{1/N} + n_{0.5}\right]^N \qquad \text{(Eq.8)}$$

Where $V_{0.5}/V_1$ represents the midpoint partial solvent isotope effect at 50 % D_2O , while V_0/V_1 is the total isotope effect, [(velocity in 100% ^1H_2O) ÷ (velocity in 100% D_2O)]. The experimental midpoint partial isotope effect was 2.98 and the calculated midpoint partial isotope effect for a one proton transfer (Equation 8) was found to be 2.99 (Table 2). For comparison purposes, the midpoint partial isotope effect calculated for a two-proton transfer in the transition-state is 4.03.

Table 2. Kinetic Parameters from solvent isotope study

	Experimental value	**One proton (Calculated)**	**Two protons (Calculated)**	**General solvation (Calculated)**
$\upsilon_{0.5}/\upsilon_1$	2.98	2.99	4.03	2.34

3.3.6 Stopped-flow experiments

Pseudo-first-order steady-state kinetic data were obtained using a solubility-limited [TPN] of 0.25 mM, at pH 7.0 and 4 °C. Because of the diminished activity at lower pH values, stopped-flow spectrophotometric data were also collected at 4 °C and pH 5.0 as only pseudo-first-order steady-state kinetic plots were observed at pH 7.0. Therefore, pre-steady state kinetic data could not be not collected for TPN hydrolysis in H_2O. However, the kinetic isotope effect studies suggested another route to pre-steady state kinetic information. When stopped-flow experiments were performed in 99% D_2O in 50 mM acetate buffer at pH 5.0 and 4 °C with 250 µM TPN, a burst of absorbance was observed (Figure 43) that could be modeled using a two-component expression containing linear and exponential terms (equation 9) [76], where [P] is the product concentration, [E] is the enzyme concentration, A_0 is the burst amplitude, k_{obs} is the overall rate constant, and k_{cat} is the turnover number (R^2=0.98).

.

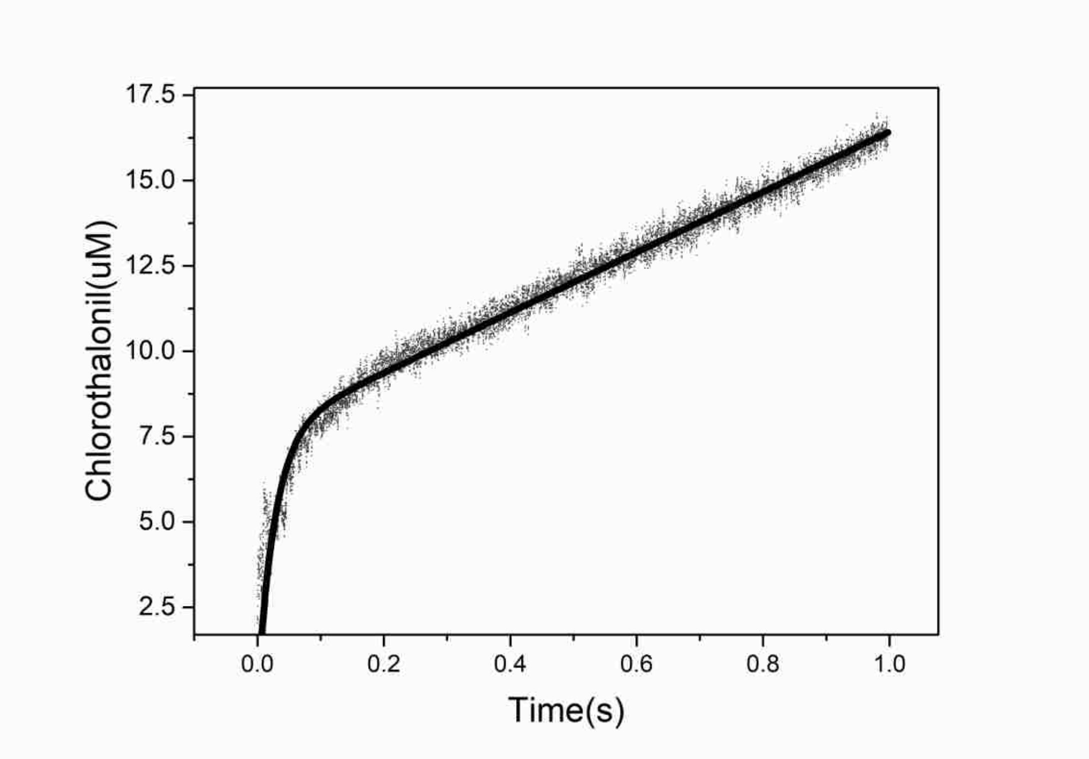

Figure 43. Stopped-flow experiment data obtained by 50mM HEPES of 99%D_2O at 4°C, pD=7.0. Data fitting of reaction in D_2O as exponential in burst phase of pre-steady state and linear equation in the steady state.

$$\frac{[P]}{[E]_0} = A_0 * (1 - e^{k_{obs}*t)}) + k_{cat} * t \qquad \text{(Eq. 11)}$$

As this experiment is performed under saturating substrate concentrations, k_1' for formation of the Michaelis complex is so high that it does not influence the multiple turnover kinetics and theoretical modeling of the data returns information only on k_2' for formation of a post-Michaelis intermediate, and k_3' for product release (equations 10 and 11). (Table 2) [76a].

$$A_0 = (\frac{k_2}{k_2+k_3})^2 \qquad \text{(Eq.12)}$$

$$k_{obs} = k_2 + k_3 \qquad \text{(Eq. 13)}$$

Fits of these data (Figure 43) provided apparent rate constants k_2' of 35.2 ± 0.1 s^{-1}, and k_3' of 1.1 ± 0.2 s^{-1}. The k_{cat} of the overall reaction was calculated to be 1.1 ± 0.1 s^{-1} in good agreement with the value calculated using equation 12, which provided a k_{cat} value of 1.08 ± 0.02 s^{-1}. These data were compared to experimentally determined steady-state kinetic data obtained at 4 °C for Chd using 250 μM TPN as the substrate at pH 5.0 in 99% D_2O acetate buffer. Under these conditions, $k_{cat} = 1.08 \pm 0.01\ s^{-1}$ and $K_m = 71 \pm 3\ \mu M$ (Table 3).

$$k_{cat} = \frac{k_2 k_3}{k_2+k_3} \qquad \text{(Eq.14)}$$

Table 3. Kinetic Parameters from stopped-flow experiment

	A_0	**K_{obs}/s**	**k_{cat} (fitting)**	**k_2/s**	**k_3/s**	**k_{cat}/s (observed)**
Value	0.93	36.34	1.08	35.20	1.13	1.10
Standard Error	0.01	0.29	0.01	0.10	0.19	0.06

3.3.7 Discussion

The prevailing dogma is that biological dechlorination reactions are catalyzed by oxidative, reductive, or thiolytic dehalogenation processes [42-44]. A relatively unknown biological dehalogenation process involves hydrolysis of a C-Cl bond [77]. Chd, a Zn(II)-dependent enzyme, has been shown to catalyze the hydrolytic dehalogenation of TPN to 4-OH-TPN and chloride (Figure 22) under ambient conditions [66b, 68]. As Chd can hydrolyze an aromatic C-Cl bond, understanding the inorganic and biological chemistry of Chd will provide insight into its catalytic mechanism, which in turn will the assist in the development of biocatalysts or small biomimetic catalysts that can be used in the environmental clean-up of TPN. To date, no catalytic mechanism has been proposed for Chd, in part because of the lack of an enzymatic assay that allows for the direct detection of product, which has prevented detailed kinetic studies.

To overcome this obstacle, a spectrophotometric kinetic assay was developed that directly detects the formation of 4-OH-chlorothalonil at 345 nm, a wavelength where there is little or no TPN absorbance [65]. Initial control reactions were performed with saturating amounts of TPN (250 μM) in 50 mM HEPES buffer at pH 7 and 25 °C in the absence of Chd by monitoring absorptions between 300 and 400 nm to determine if any TPN hydrolysis occurred under the experimental conditions used. With no increase in absorbance observed, 10 μM of Chd was added to the reaction resulting in a steady increase in absorption at 345 nm. The rate of increase at 345 nm was highly reproducible and dependent on the concentration of Chd and TPN as well as the temperature and pH of the reaction mixture. At temperatures above 30 °C gradual inactivation occurs, which is indicative of Chd denaturation. Having established the viability of directly detecting the product of TPN hydrolysis, the kinetic parameters k_{cat} and K_m were determined at pH 7.0 and 25 °C over a 60 s time period. Plots of [TPN] vs initial rate were fit to the Michaelis-Menten equation, which provided a k_{cat} value of 24 ± 2 s^{-1} and a K_m value of 110 ± 30 µM, in good agreement with values previous reported using a non-continuous assay performed under similar reaction conditions [66b, 68].

The development of a continuous spectrophotometric assay for Chd, has allowed us to ask and answer several basic biological and mechanistic questions, such as: How many active site metal ions are required for full enzymatic activity? How many ionizable groups are required for catalysis? How many protons are transferred in the transition-state? What is the rate-limiting step in the reaction? It has been suggested that Chd requires two Zn(II) ions to be fully active and that these Zn(II) ions form a dinuclear active site [66b, 68]. However, inductively coupled atomic emission spectroscopy (*ICP-AES*) data obtained on as purified Chd revealed that ~0.9 Zn(II) ions bind per monomer and size exclusion chromatography indicates that Chd exists primarily as a dimer (~72 kDa) in solution.

Activity titrations indicated that maximum catalytic activity is observed with only one Zn(II) ion per monomer of Chd with an intrinsic K_d value of 0.17 µM, suggesting that any other Zn(II) binding is unrelated to catalysis. It should be noted that in previous studies, the His_6-tag was not removed before kinetic data were obtained [66b, 68]. As His_6-tags have high affinity for Zn(II) ions [78], it is entirely possible that adventitious metal binding to the His_6-tag led to the suggestion that more than one metal ion is required for catalysis.

Quantitative analysis of the pH-dependence of Chd activity suggested [c.f.[79]] that one catalytically competent ionizable group with $pK_{ES1} \approx 5.4$ must be deprotonated in the ES complex, and another with $pK_{ES2} \approx 9.9$ must be protonated, respectively, to facilitate catalysis. Assignment of the observed pK_{ES} values is difficult in the absence of an X-ray crystal structure, but likely candidates for pK_{ES1} are the deprotonation of an active site His residue [80] (whose putative pK_a is 5-7 [57b]) while pK_{ES2} might be due to the deprotonation of the leaving group or an active site residue such as an Arg or Lys [66b]. Alternatively, pK_{ES2} may be due to the deprotonation of Ser126, which was shown to be required for catalysis [66b] or a metal-bound water molecule depending on which catalytic mechanism is operable.

Analysis of the pH-dependence of $\log(k_{cat}/K_m)$ [c.f. (35)] provided a pK_{E1} value of 5.4 and a pK_{E2} value of 9.5 for two enzyme-centered ionizable groups, respectively, that are involved in catalysis. pK_{E1} is most likely due to an active site histidine residue but could also be the deprotonation of the metal-coordinated water molecule. Moreover, the enzyme-centered pK_{E2} value, like pK_{ES2}, is most likely due to the deprotonation of an active site residue such as an Arg or Lys but could also be Ser126 or further deprotonation of the metal bound water molecule.

Kinetic isotope effect studies are an excellent way to gain an understanding of the nature of the rate-limiting step as well as probe the transition-state of catalytic reactions [81]. Primary isotope effects are observed if a bond to the labeled atom is made or broken during the reaction whereas secondary isotope effects describe processes at other positions. I examined the $^1H/^2H$ solvent isotope effect of Chd using TPN as the substrate at pH 7.0, ($p^2H = p^1H$ meter reading + 0.4) [82]. The intrinsic primary isotope effect, k_H/k_D, is related to the symmetry of the transition-state for that step (*i.e.* the larger the isotope effect, the more symmetrical the transition-state) with the theoretical limit being 9 at 37°C in the absence of tunneling effects.[83] For the simplest case, in which a single proton produces the solvent isotope effect, a plot of atom fraction of deuterium *vs.* V_n/V_0 is linear, where V_n is k_{cat} at a particular fraction of deuterium and V_0 is k_{cat} in buffer containing 0% D_2O. [84] The presence of D_2O lowers the catalytic activity of Chd and results in a solvent isotope effect of 2.98. This normal isotope effect suggests that an O-H bond is broken in the transition-state.[83, 85]

For Chd, V_n/V_0 is a linear function of n indicating that one proton is transferred during catalysis with a fractionation factor of 0.17. Analysis of the midpoint solvent isotope effect also supports involvement of a single proton transferred in the transition-state. Therefore, the Zn(II) ions appear to be responsible for the proper positioning of the hydroxyl group relative to the substrate and this hydroxyl group likely interacts with a general base, such an His or Asp/Glu residue. Based on these data and the observed pK_{E1} and pK_{ES2} values, a His residue appears most likely to facilitate the transfer of a proton and likely reflects the transfer of a proton from an active site water molecule to an active site His residue forming a more nucleophilic hydroxide.

Based on these data, the simplest model was used that describes the observed changes in ionization states of active site residues with changing pH and the number of protons transferred in the transition-state (Scheme 1).

Scheme 1. Proposed kinetic model for Chd where $E(H_2O)$ is enzyme containing water molecule at active site, E^P is the enzyme at protonated, E^D is the enzyme at deprotonated, S represents substrate, $ES(H_2O)$ represent the enzyme-substrate complex containing water molecule at active site, E^PS is the enzyme-substrate complex at protonated state, E^DS is the enzyme-substrate comple at deprotonated state, [I] is an intermediate state with deprotonated water and [P] is product.

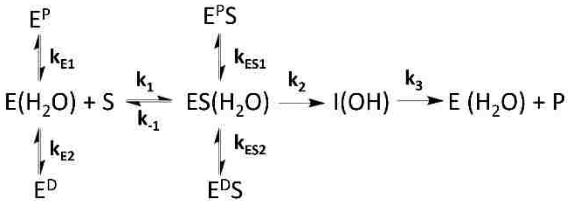

This model assumes that: i) the substrate-binding step leading to the formation of an enzyme-substrate complex following steady-state kinetics (*e.g.* the enzyme, substrate and enzyme-substrate complex are at equilibrium) and k'_{-1} is larger than k'_2 as neither the substrate or the product are sticky and k'_2+k'_3contains the rate-limiting step (*i.e.* C-Cl bond breaking or product release).[86]

An important question in understanding the hydrolysis of TPN by Chd is: "What is the rate-limiting step in the catalytic reaction?" Pre-steady-state kinetic data indicated that formation of the Michaelis complex is very fast compared to the hydrolysis and product-release steps and, therefore, the rate constants for the latter two could be estimated from multiple-turnover stopped-flow spectrophotometry. Based on the results, a minimal three-step kinetic model is proposed that allows for fast reversible substrate binding, the formation of a post-Michaelis pre-transition-state intermediate, and the post-transition-state release of product (Scheme 2).

Scheme 2. Proposed pre-steady state model for the dechlorination of TPN by Chd.

$$E(H_2O) + S \underset{k_{-1}}{\overset{k_1}{\rightleftharpoons}} ES(H_2O) \xrightarrow{k_2} I(OH) \xrightarrow{k_3} E\,(H_2O) + P$$

Based on the data presented herein, the electron density distribution of free and Zn(II) bound TPN calculated using Gaussian 9-win (Figure 44), and the previously reported kinetic and site-directed mutagenesis data [66b, 68], two possible catalytic mechanisms are proposed for the hydrolysis of TPN by Chd (Figure 45). I propose the initial catalytic step involves the binding of the nitrile nitrogen, to the active site Zn(II) ion, which results in the removal of electron density from the aromatic ring activating the ortho carbon for nucleophilic attack (Figure 45; B) [27a, 87]. The significantly enhanced electrophilic character of the ortho carbon upon nitrile binding to Zn(II) suggests that Zn(II) binding activates the ortho carbon towards nucleophilic attack and may also help to position the ortho carbon relative to the nucleophile, thus pre-organizing the transition-state.

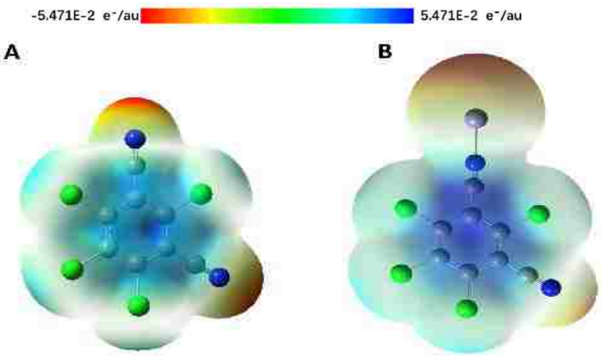

Figure 44. Gaussian-9 derived electron density map of TPN (A) and TPN bound

to a Zn(II) ion (B). (carbon: gray; nitrogen: blue; chlorine: green; zinc: dark gray).

Based on our kinetic data, an active site His residue needs to be deprotonated so it can accept a single proton from a Zn(II)-bound water molecule providing the catalytic nucleophile, which is pre-organized adjacent to the activated ortho carbon of TPN. His128, which is strictly conserved, is proposed to play the role of the general acid/base. Once nucleophilic attack occurs, Cl^- and 4-OH-TPN are formed and released from the active site, which is the rate-limiting step in catalysis. Finally, a water molecule binds to the active site Zn(II) thus reforming the active catalyst (Figure 45).

Even though the mechanistic proposal involving nitrile binding to the active site Zn(II) ion is logical and has advantages in that binding activates the ortho carbon for nucleophilic attack and pre-organizes the transition-state by positioning the Zn(II) bound hydroxide near the ortho carbon, there is no experimental evidence to support TPN binding to the active site Zn(II) ion at this time. Therefore, an alternative pathway involving substrate binding near the active site but not directly to the Zn(II) ion, must also be considered (Figure 44B). Under such a scenario, a protonated active site residue (R_1) would form a hydrogen bond with the nitrile nitrogen. Previous studies as well as our pH dependent assay suggest Ser126 might play such a role but Trp241 was also found to be essential for the reaction and cannot be ruled out. The existence of an R1 residue is supported by the loss of catalytic activity at high pH values. Moreover, the electron density map of TPN in the absence of nitrile Zn(II) binding reveals some electrophilic character at the ortho carbon (Figure 44; A), suggesting susceptibility to nucleophilic attack. This active site residue would pre-organize the ortho carbon with the Zn(II)-bound hydroxide nucleophile, which like in pathway A, would transfer a proton to the active site acid/base His residue in the transition-state. Once nucleophilic attack occurs, like pathway A, Cl^- and 4-OH-TPN are formed and released from the active site, which is the rate-limiting step in catalysis. A water molecule would then bind to the active site Zn(II), reforming the active catalyst.

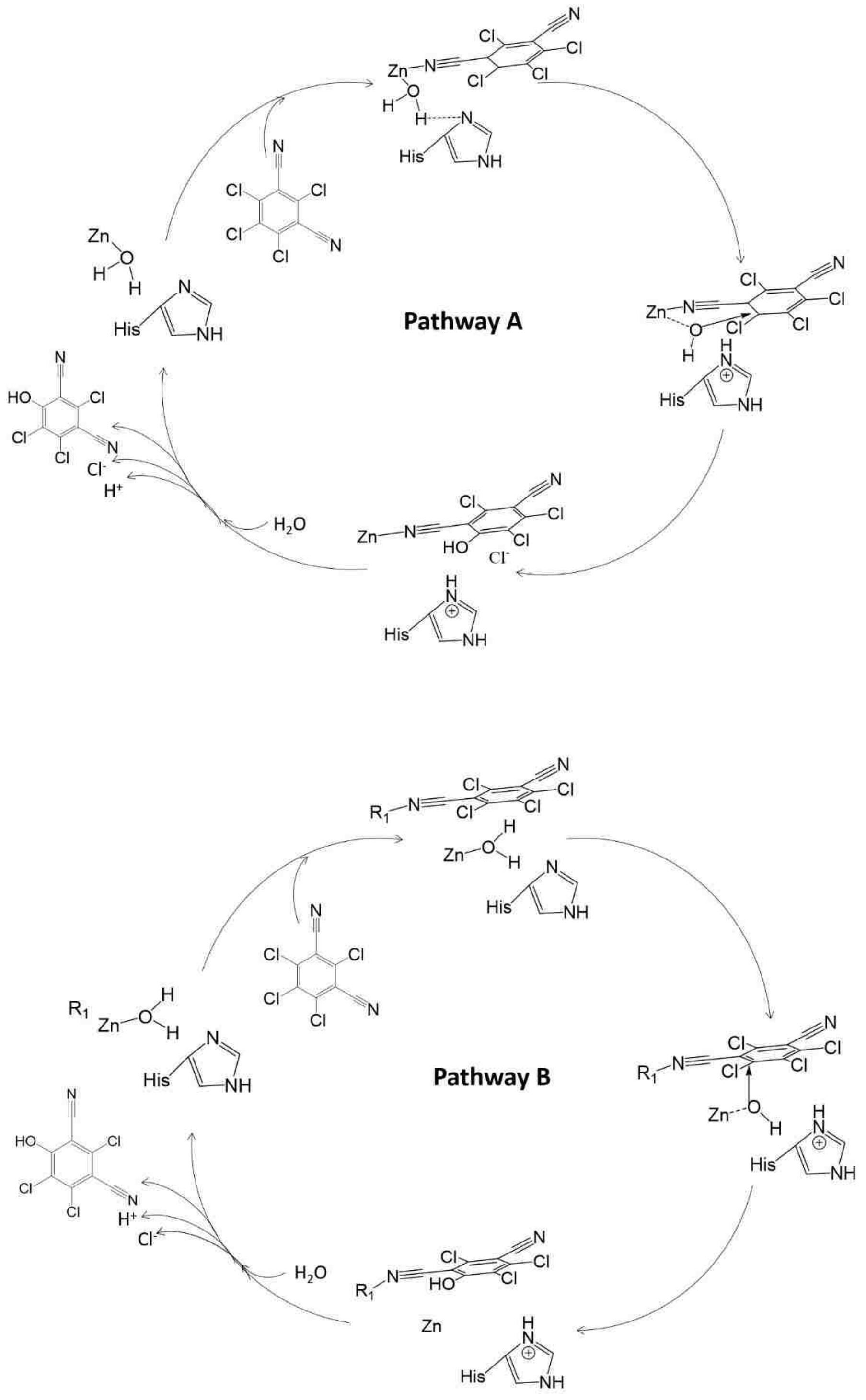

Figure 45. General mechanism of chlorothalonil dechlorination reaction by direct binding and indirect binding pathways. The histidine residue plays role as proton acceptor for Zn(II)- bound water deprotonation. Cl^- at ortho carbon was substituted by the nucleophilic attack of OH^- at final step. In the pathway B, TPN was stabilized by the putative π-π interactions and H bond with protonated residue (R_1) at active site.

3.5 Summary

In conclusion, the development of a spectrophotometric assay that allows for the direct detection of the product 4-OH-TPN, has allowed the first mechanistic studies to be carried out on the hydrolytic dehalogenase, Chd. Metal titration data indicate that a single metal ion is required for catalytic activity so Chd can be classified as a mononuclear hydrolytic Zn(II)-dependent enzyme. Chd is a dimer in solution and exhibits a broad kinetic pH dependence with the maximum velocity dependent on two ionizable groups, one with $pK_a \approx 5.4$ and one with a $pK_a \approx 9.9$. Solvent kinetic isotope effect studies indicate that one proton is transferred in the transition-state, likely due to the breaking of a water O-H bond. Pre-steady state kinetic studies performed under saturating substrate conditions revealed a burst phase followed by a linear, steady-state phase. Determination of k_2' and k_3' revealed that the product release step is the slow-step in the catalytic cycle. Taken together, along with density functional calculations on TPN in the absence and presence of Zn(II), have allowed two potential catalytic mechanisms to be proposed. Further studies will be required to distinguish between mechanistic pathways A or B (Figure 45).

CHAPTER FOUR X-RAY CRYSTAL STRUCTURE OF THE CHLOROTHALONIL HYDROLYTIC DEHALOGENASE FROM *PSEUDOMONAS* SP. CTN-3

4.1 Introduction

Hydrolytic dehalogenases are one of four types of dehalogenases that have recently gained attention for their possible applications in environmental bioremediation processes.[88] These enzymes function to remove halides from highly toxic compounds under ambient conditions, resulting in less toxic metabolites.[52b, 89] A two-step mechanism was proposed for serine- and aspartate-type hydrolytic dehalogenases, where the first step involved nucleophilic attack by an aspartic acid[90] or serine[91] residue on a halogenated carbon, producing an ester intermediate. Within the second step, a water molecule hydrogen bound to an active site histidine residue, is activated and hydrolyzes the ester intermediate (Figure 46).[52b] Trans-3-chloroacrylic acid dehalogenase is an exception to this proposed mechanism as it utilizes an activated water molecule that is hydrogen bound to an adjacent base for direct nucleophilic attack on an sp^2 halogenated carbon atom.[92] Serine/aspartate-type hydrolytic dehalogenases only hydrolyze aliphatic substrates while enzymatic dehalogenation reactions of aromatic compounds typically require co-enzymes such as CoA in 4-Chlorobenzoyl coenzyme A dehalogenase,[90a] glutathione in tetrachlorohydroquinone reductive dehalogenase (PcpC),[93] NADPH in pentachlorophenol-4-monooxygenase (PcpB),[94] and FAD and NADH in iodotyrosine deiodinase[95] and chlorophenol-4-monooxygenase.[90] In each of these enzymes, the active site motif provides substrate binding pockets that stabilize the aromatic substrates. In addition, the required co-enzymes are prosed to not only play a role as a redox reagent but also to assist in substrate stabilization.[52b]

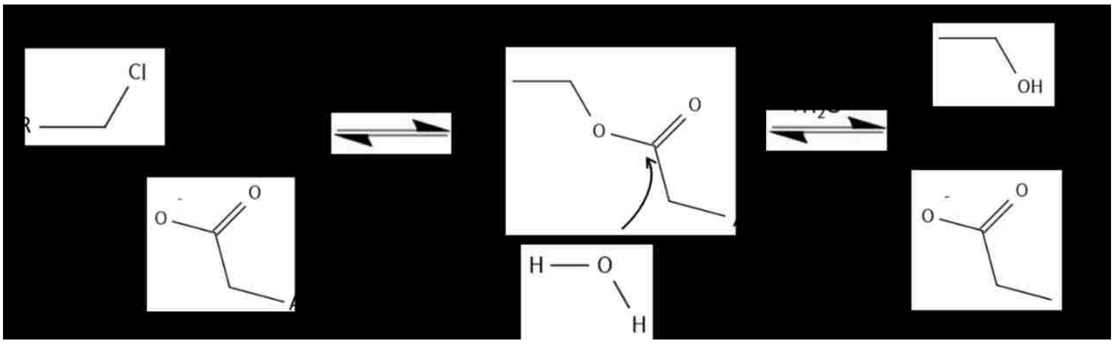

Figure 46. Two-step mechanism for non-metallo hydrolytic dehalogenases where B: represents the active site base that functions to activate a water molecule.

Chlorothalonil dehalogenase (Chd) from *Pseudomonas sp.* CTN-3 is a Zn(II)-dependent hydrolytic dehalogenase that selectively converts one of the most widely used fungicides in the US, chlorothalonil (TPN; 2,4,5,6-tetrachloroisophtalonitrile) to the less toxic metabolite, 4-hydroxytrichloroisophthalonitrile (4-OH-TPN) (Figure 22).[6] Given *Pseudomonas sp.* is predominately found in soil and water, it is not surprising that the organism expresses Chd to cope with residual TPN present in the environment. The only aromatic hydrolytic dehalogenase that has been structurally characterized to date is atrazine chlorohydrolase from *Pseudomonas sp.* (AtzA; PDB: 4V1X at 2.2 Å), which contains an iron ion coordinated by four histidine residues, an aspartate and a water molecule.[96] While both AtzA and Chd hydrolytically dehalogenate aromatic compounds, they have relatively low sequence identity (>19%), different metal ion requirements, and biochemical properties. Chd requires Zn(II), which was proposed to reside in a binding motif commonly found in metallo-β-Lactamses (MBL) and is proposed to be dimeric in solution vs. hexameric for AtzA.[6, 96] While Zn(II) is required for Chd activity, its catalytic role remains unknown.

A major limitation in understanding the catalytic mechanism of Chd and in developing small molecule catalysts that specifically target TPN, is a lack of knowledge regarding its structure and active site architecture. Herein, the 1.96 Å X-ray crystal structure of a fifteen residue N-terminal truncated Chd enzyme was reported that is fully active, using single wavelength anomalous dispersion (SAD). The structure reveals that Chd is a homodimer with a structural Zn(II) residing at the dimer interface and a mononuclear Zn(II) active site that resembles metallo-β-lactamases. Based on the X-ray crystal structure, substrate modeling, and previous kinetic studies,[97] a detailed catalytic mechanism is proposed.

4.2 Materials and Methods

4.2.1 Materials

NEB restriction enzymes, T4 DNA Ligase, Agilent QuikChange II site-directed mutagenesis kit, Ni-NTA columns, Wizard® SV gel and PCR clean-up systems, size exclusion columns 4-(2-hydroxyethyl)-1-piperazineethanesulfonic acid, potassium bromide, potassium sodium tartrate, and TPN were purchased commercially (Fisher Scientific, WI) at the highest purity available. TEV protease (EC 3.4.22.44) was obtained via previously published methods.[98]

4.2.2 N-terminal sequence modification of Chd

The first fifteen residues of the N-terminus of WT Chd were removed by PCR (sense primer: ACTCCATGGATGCCGTGAAATTTAG, antisense primer: CATAAGCTTTTAATGGTGATGGTGATGGTGATG). The modified Chd gene containing NcoI and HindIII restriction sites was amplified under standard PCR conditions for gene cloning.[99] The PCR products were purified by agarose gel electrophoresis and Wizard SV gel and subcloned into pET28a+, creating the new expression vector pET28a+-Chd^T. The modified sequence was verified by Functional Biosciences (Madison, WI.).

4.2.3 Expression and Purification of Chd^T

The plasmid containing Chd^T was freshly transformed into BL21(DE3) competent cells (Stratagene), and a single colony was used to inoculate 50 ml of LB-Miller culture containing 50 μg/mL kanamycin with shaking overnight at 37 °C as previously described.[97] Briefly, this culture was used to inoculate a 1 L culture and the cells were grown at 37 °C until the OD_{600nm} reached 0.8-1.0. The culture was cooled on ice, induced with 0.1 mM isopropyl β-D-1-thiogalactopyranoside (IPTG) supplemented with 0.05 mM $ZnCl_2$, and expressed at 25 °C for 16 hours. Cells were harvested by centrifugation at 6,370 x *g* and 4 °C for 10 min in a Beckman Coulter Avanti JA-10 rotor and resuspended in 20 mM Tris-HCl buffer, pH 7.0 containing 50 mM NaCl, 10 mM TCEP, and 25 mM imidazole at a ratio of 5 ml per gram of cells. Cells were lysed by ultrasonication (Misonix Sonicator 3000) for 4 min (30 s on 45 s off) at 21 W. The crude extract was obtained after centrifugation in a JA-20 rotor at 31,000 x *g* and 4 °C for 20 min.

Crude extracts of Chd^T (100 mg) were loaded onto a 5 ml Ni-NTA (nitrilotriacetic acid) Superflow Cartridge (Qiagen) using an ÄKTA FPLC P-960. The column was washed with 50 mL of 20 mM Tris-HCl buffer, pH 7.0 containing 50 mM NaCl and 25 mM imidazole, followed by 50 mL of 20 mM Tris-HCl buffer, pH 7.0 containing 50 mM NaCl and 75 mM imidazole. The protein was eluted using a linear imidazole gradient (75 to 500 mM) at a flow rate of 2 mL/min. Active protein fractions were pooled and concentrated using 50 mM Tris buffer, pH 7.0 containing 1 mM EDTA with an Amicon Ultra-15 10,000 MWCO centrifugal filter unit (Millipore) resulting in ~12 mg/L of soluble Chd^T-His$_6$.

The His$_6$-tag was removed by treating His$_6$-tagged Chd^T with His$_6$-tagged TEV protease (EC 3.4.22.44) for 16 h at 4 ˚C in 50 mM Tris, pH 8.0. Cleaved protein was concentrated with a Centricon (15,000-MW cutoff; Amicon) to 3 mL and loaded on IMAC to remove the remaining cleaved His$_6$-tag, uncut protein and the His$_6$-tagged TEV protease, while the flow through containing Chd^T was collected and washed with 50 mM HEPES buffer, pH 7.0 containing 10% glycerol. Purified protein was analyzed by SDS-PAGE with a 12.5% polyacrylamide SPRINT NEXT GEL™ (Amresco). Gels were stained with Gel Code Blue (Thermo-Fisher Scientific). Protein concentration of crude extracts was determined using a Coomassie (Bradford) Protein Assay Kit (Pierce) and pure protein by measuring the absorbance at 280 nm with a Shimadzu UV-2450 spectrophotometer equipped with a TCC-240A temperature-controlled cell holder. Theoretical molecular weights and protein extinction coefficients were calculated with the ExPASy compute pI/Mw tool.

4.2.4 Activity assay of Chd^T

The enzymatic activity of Chd^T towards TPN was measured using a Shimadzu UV-2450 spectrophotometer equipped with a TCC-240A temperature-controlled cell holder in 1 mL quartz cuvettes. A 1 mL reaction consisted of 50 mM HEPES buffer, pH 7.0 at 25 °C and various concentrations of TPN. The rate of TPN dehalogenation was determined by continuously monitoring the formation of 4-OH-TPN at 345 nm ($\Delta\varepsilon_{345} = 3.5\ \mathrm{mM^{-1}cm^{-1}}$). Data analysis was performed using OriginPro 9.0 (OriginLab, Northampton, MA). The kinetic constants V_{max} and K_m were calculated by fitting to the Michaelis-Menten equation. One unit of enzyme activity was defined as the amount of enzyme that catalyzed the production of 1 μmol of the TPN minute at 25 °C.

4.2.5 Crystallization

Purified Chd^T was exchanged into 50 mM HEPES buffer, pH 7.5 containing 10% glycerol for crystallization and concentrated to a final protein concentration of 10 mg/mL. Initial crystallization screens using a Gryphon Crystallization Robot (Art Robins Inc.) and Emerald Biosystems Wizard III/IV screen sets, produced crystals of Chd^T in 10% PEG 6000 and 100 mM HEPES buffer, pH 7.0. Crystallization optimization leads revealed the best quality Chd^T crystals *via* sitting drop vapor diffusion occurred by mixing 6 μL of (10 mg/mL) Chd^T with 6 μL of well solution (10% PEG 6000, 100 mM HEPES, pH 7.0). Crystals were allowed to grow at room temperature and reached optimal size and morphology for data collection after 7-10 days. Crystals were manually transferred to well solution supplemented with 30% Glycerol (cryo protectant) and flash frozen in liquid N_2.

4.2.6 X-ray diffraction data collection

Single wavelength anomalous dispersion (SAD) and monochromatic data were collected at the LS-CAT 21-ID Advanced Photon Source (APS) at Argonne National Laboratory (ANL). SAD data sets were collected at a wavelength of 1.28167 Å while monochromatic data were collected at 0.98 Å at 100 K using a Dectris Eiger 9M detector. Data sets were indexed and integrated using HKL2000[4] suite.

4.2.7 Model Building and Refinement

The structure of Chd^T was manually solved by single wavelength anomalous dispersion (SAD) using autosol in the Phenix software suite.[100] The model was rebuilt using COOT,[101] refined using Phenix, and analyzed in COOT and USCF Chimera.[102] Final refinement statistics are reported in Table 3 and structural figures were made in USCF Chimera.

Table 3. Crystallographic Parameters and Statistics for Chd^T (hOAT1).

Data Processing	
Space group	$P\,2_1\,2_1\,2_1$
Cell dimension	
α, β, γ (deg)	54.8, 105.2, 122.4
a, b, c (Å)	90, 90, 90
Processed Resolution (Å)	1.96
I/σ (I)	17.5 (1.1)
Resolution at I/σ (I) =2 [a]	1.98
R_{merge}[b] (%)	8.7 (117.6)[c]
R_{pim}[d] (%)	2.7 (35.0)
CC ½ [e] (%)	(63.1)
Completeness (%)	98.0 (87.6)
Multiplicity	7.2
No. Reflections	362,906
No. Unique Reflections	50,386
Refinement	
R_{work}[f]/R_{free}[g] (%)	15.79/19.75
No. of Atoms	
protein	4,693
ligand	3
water	379
B factors (Å^2)	
protein	23.7
RMSD [h]	
bond lengths (Å)	0.010
bond angles (deg)	1.014
Ramachandran plot (%)	
most favored	96.14
allowed	3.19
outliers	0.67

[a] Provided Resolution at $I/\sigma = 2$ for conventional assessment of data quality
[b] $R_{merge} = \Sigma|I_{obs} - I_{avg}|/\Sigma I_{avg}$
[c] The values for the highest-resolution bin are in parentheses
[d] Precision-indicating merging R
[e] Pearson correlation coefficient of two “half” data sets
[f] $R_{work} = \Sigma|F_{obs} - F_{calc}|/\Sigma F_{obs}$
[g] Five percent of the reflection data were selected at random as a test set, and only these data were used to calculate R_{free}
[h] Root-mean square deviation

4.2.8 Double mutation at the structural zinc binding site

The His143 and Asp146 ligands for the structural Zn(II) site, were mutated to Ala143 and Ala146 by a single mutagenic primer as follows: Sense primer: TTGATGGT**GC**CCTGGCGG**C**CGATAAGGCGTTCATGGT, antisense primer: ACCATGAACGCCTTATCG**G**CCGCCAGG**GC**ACCATCAA. Mutated residues are shown in bold. The sense primer had a completely complementary sequence to the corresponding antisense primer. The first PCR reaction was performed using sense primer and antisense primer in separate tubes (25 μL). Following denaturation at 98 °C for 1 min, 5 PCR cycles were carried out with each cycle comprised of incubation at 98 °C for 15 s, followed by a 30 s annealing step at 65 °C, and a 1 min. extension at 71 °C. A 50 μL solution was prepared by combining two tubes for a second PCR reaction, which was carried out under the same conditions as the first PCR reaction but for 55 cycles. The final products were transformed directly into XL10-gold ultracompetent cells. The mutated Chd^T sequence was verified by DNA sequencing by Functional Biosciences (Madison, WI.)

4.2.9 MALDI-TOF mass spectrometry

Saturated α-CHCA thin layer solution was prepared on a MALDI target.[103] A 2 μL protein sample (10 μM) was mixed with a DHB-CHCA matrix on a MALDI target by the "sandwich method".[104] Mass spectra of each sample were obtained on a Bruker microflex LRF™ MALDI-TOF Mass spectrometer.

4.2.10 Substrate docking

TPN poses were created and optimized by Molecular Operating Environment (Chemical Computing Group, Montreal, Canada). The TPN substrate was docked into the Chd^T active site pocket using the Autodock Vina program, which is a structural analysis panel of Chimera 1.13.1rc (UCSF Chimera, San Francisco, CA). The optimized TPN molecule was deemed a ligand while the active site of Chd was assigned as a receptor. The oxygen position of the active site Zn(II)-bound water/hydroxide was fixed as were the protein residue ligands. The best pose, based on the docking scoring function vs binding energy,[105] was considered the final model.

4.3 Results and Discussions

4.3.1 Overall structure of ChdT

Crystals of Chd^T were grown at 25 ^{o}C by vapor diffusion in hanging drops containing 1 mL of precipitant solution (10% PEG 6000, 100 mM HEPES, pH 7.0) and 1 μL of 10 $mgmL^{-1}$ of Chd^T. The crystals grew within 7-10 days and reached a size of 54.8 mm x 105.2 mm x 122.4 mm. The Chd^T crystals belonged to the primitive orthorhombic space group $P2_12_12_1$ with unit cell parameters a = 90 Å, b = 80 Å, c = 90 Å and the structure was solved *via* SAD using a wavelength of 1.28167 Å, close to the absorption edge of Zn. The final model was refined to a resolution of 1.96 Å with R_{free} and R_{work} values of 19.80% and 16.22%, respectively. Final data processing and refinement statistics are listed in Table 1. A single homodimer was identified in an asymmetric unit.

The two monomers of the homodimer display a two-fold non-crystallographic rotational axis that passes through a non-catalytic structural Zn(II) site (Figure 47A). From a side view (Figure 47B), the structural Zn(II) ion is close to one side of the dimer surface. For convenience purposes, we refer to this side of the dimer protein as the "top" side *i.e.* where the structural Zn(II) ion resides and the opposite side to as the "bottom". The crystallographic packing was analyzed using PISA[106] in the CCP4 suite and the observed homodimer was predicted to be the only stable quaternary structure in solution. The total predicted accessible surface area (ASA) is 23,224.0 Å^2, while the predicted buried surface area (BSA) is 1,833.3 Å^2.

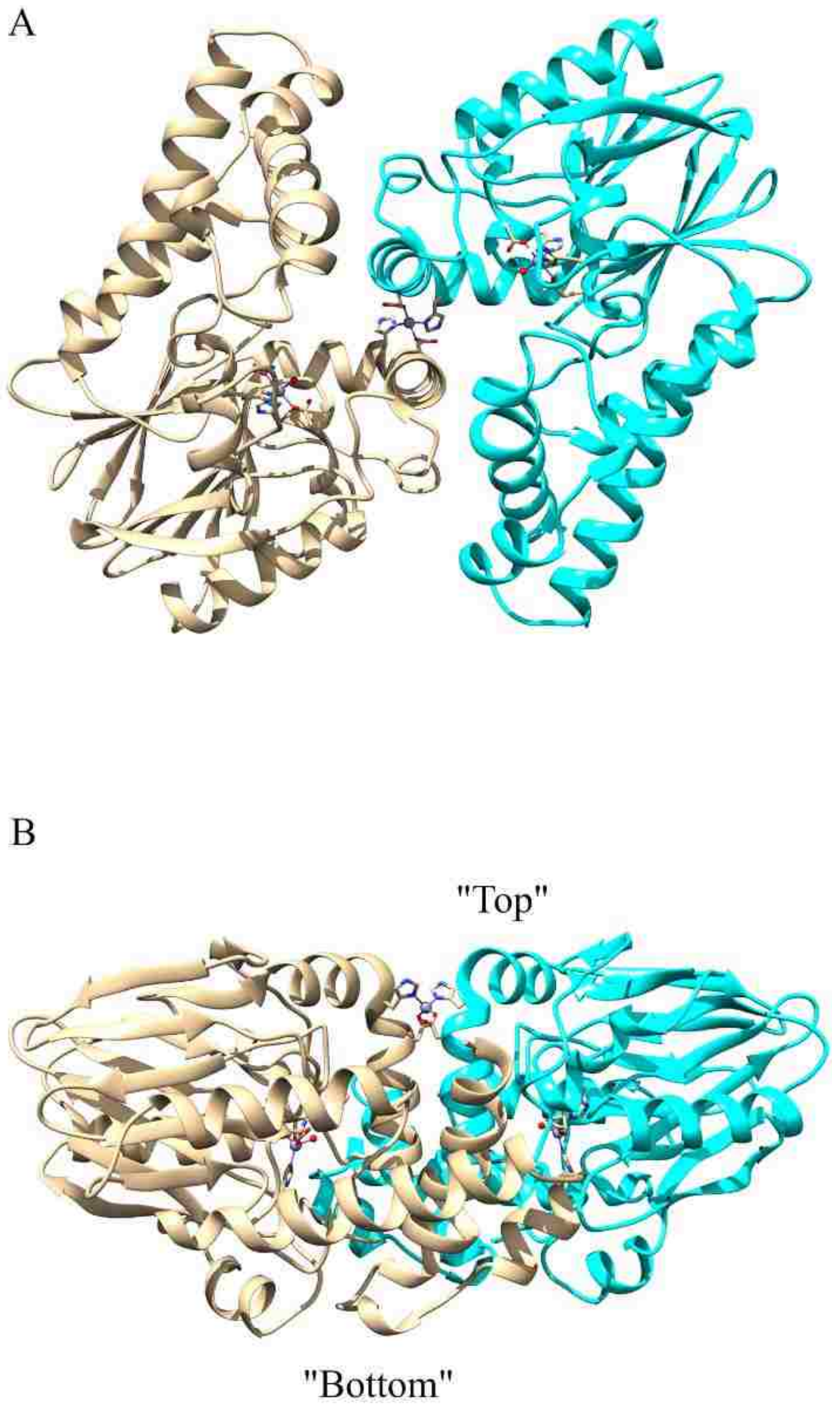

Figure 47. A**)** Homodimer of Chd^T. Three Zn(II) ions are shown as balls and the coordination residues are shown as sticks. B**)** A side view of the Chd^T homodimer, with defined “Top” and “Bottom” sides according to the relative positions to the structural Zn(II) ion.

Each monomer contains a catalytic Zn(II) ion that is solvent-accessible from both the “top” and the “bottom” side of the protein (Figure 48). From the “bottom”, a “Y” shaped channel exists with two branched channels that lead to the catalytic Zn(II) ion and share a single large (8.5 x 17.8 Å) opening to bulk solvent. On the other hand, the structural Zn(II) ion is not accessible to the bulk solvent despite being located close to the “top” side surface. From the “top” side, the structural features surrounding the structural Zn(II) ion helps to form two bent channels that provide access the catalytic Zn(II) ions.

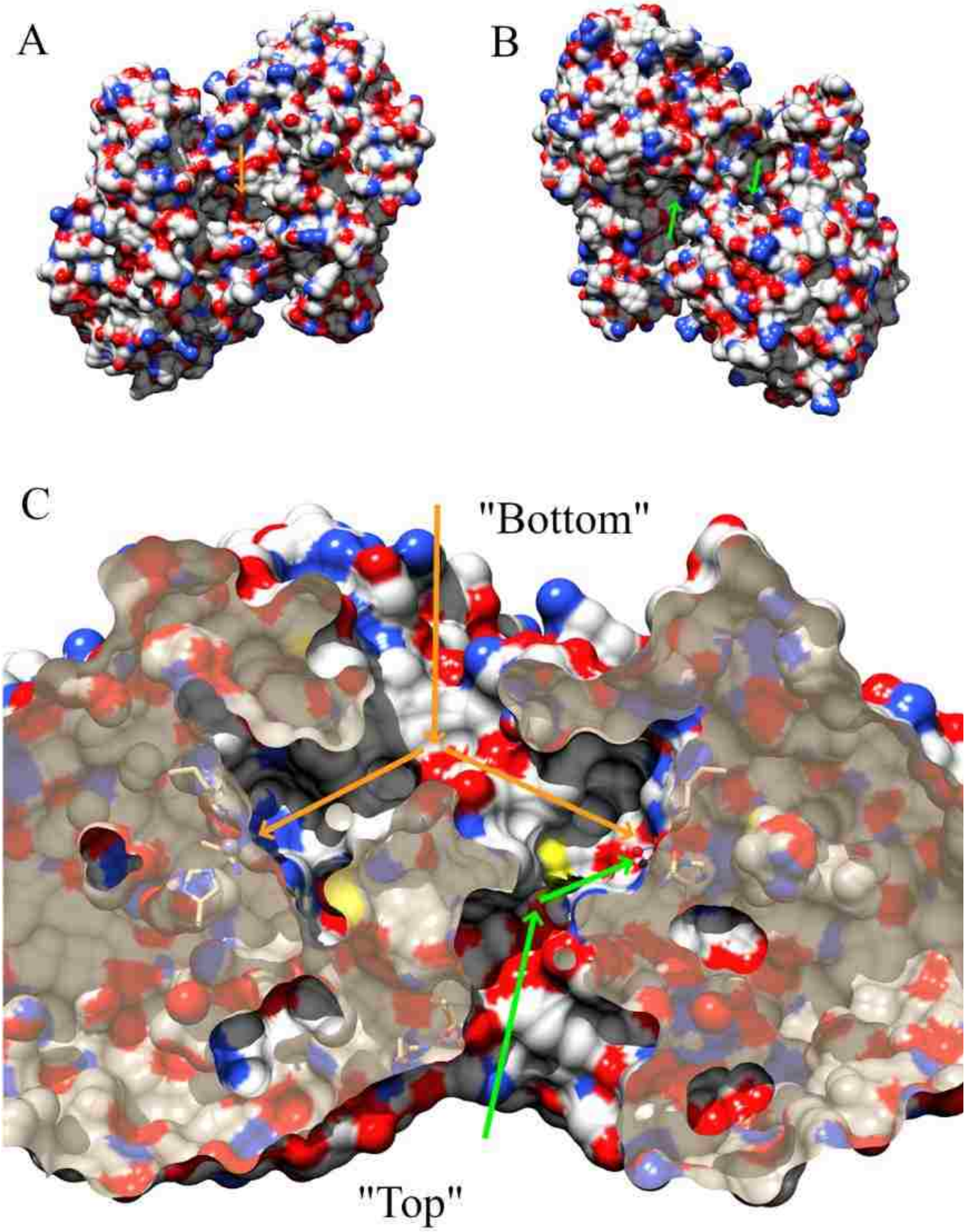

Figure 48. A) Hydrophilicity surface map of the Chd^T dimer from the “bottom” side. The orange arrow indicates a single large opening. B) Surface view of the Chd^T dimer from the “top” side. The green arrows indicate two separate openings. C) Cross sectional view of the Chd^T dimer. The orange arrows indicate a “Y” shaped channel with access to the catalytic Zn(II) ions from the bottom side while the green arrows indicate one branch of the “Y” shaped channel that

provides access to the catalytic Zn(II) from the “top”. The other “Y” shaped channel from the “top” side is on the backside of this view and was not visible.

4.3.2 The monomer protein fold is an αββα-sandwich

The overall protein fold of the Chd^T monomer (Figure 49A) was screened within the D.A.L.I. server[107] for comparison against all known structures. Interestingly, known structures with any similarity to Chd were reported as either β-lactamases or alkylsulfatases.[108] The top representative structure from each of these protein families, CphA, and Pisa1, were selected for detailed comparison and structurally aligned with Chd^T (Figures 49B and 49C). The overall fold of the Chd^T monomer aligned well with the overall structure of β-lactamases, CphA (PDB Code: 3IOG), except for an extra C-terminal motif. The N-terminal portion (residues 1-277) of Chd forms an αββα-sandwich fold that is commonly observed in the β-lactamase superfamily; however, Chd^T also possessed an additional C-terminal motif (residues 278-327) that originates in the middle of a long helix that is not found in the CphA structure. On the other hand, when Chd^T was structurally aligned with one subunit of an alkylsulfatase, Pisa1 (PDB Code: 2YHE), the additional C-terminal motif observed in Chd^T was present in Pisa1.

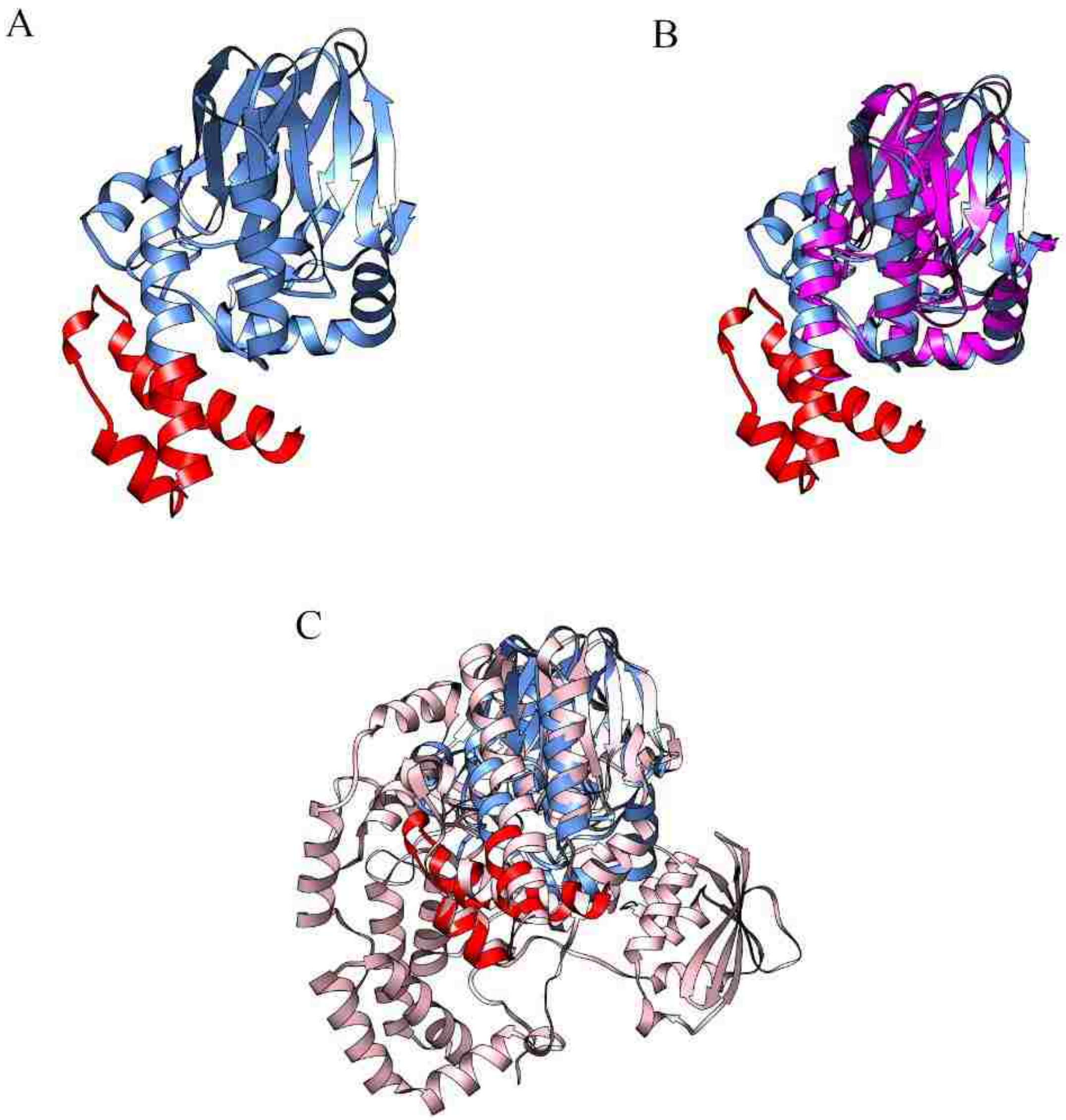

Figure 49. A) The overall protein fold of a Chd^T monomer. The β-lactamase fold (residues 1-277) is in blue. A C-terminal motif (residues 278-327) is in red. B) Chd^T is superimposed with the β-lactamase CphA (PDB code: 3IOG), which is in magenta. **C)** Chd^T is superimposed with an SEC alkyl sulfatase (PDB code: 2YHE), which is in pink.

4.3.3 Active site of Chd

The coordination geometry of the active site Zn(II) ion is identical in both monomers and the simulated annealing composite map around each metal ion and their coordinating residues are consistent with the active site Zn(II) ion residing in a slightly distorted trigonal bipyramid or TBP geometry (Figure 50). The catalytic Zn(II) ion ligands include the N nitrogen’s of His117 (2.0 Å) and His257 (2.0 Å) along with a water/hydroxide oxygen atom (2.6 Å) making up the equatorial positions while the axial component of the TBP geometry is completed by the coordination of a carboxylate oxygen atom of Asp116 (2.1 Å) and a carbonyl oxygen atom of Asn216 (2.2 Å) (Table 4; Figure 50).

Table 4. Selected Bond lengths

Atom1	**Atom2**	**Length (Å)**
Active site Zn	Carboxylate oxygen atom of Asp116	2.1
Active site Zn	N nitrogen’s of His117	2.0
Active site Zn	N nitrogen’s of His257	2.0
Active site Zn	Carbonyl oxygen atom of Asn216	2.2
Active site Zn	Metal-bound water/hydroxide	2.6
N nitrogen’s of His114	Metal-bound water/hydroxide	2.9
N nitrogen’s of His114	Nitrogen atom of Asn216	2.7
N nitrogen’s of His114 (perpendicular)	Metal-bound water/hydroxide	5.4
N nitrogen’s of His114 (perpendicular)	Nitrogen atom of Asn216	3.1
Structural Zn	N nitrogen’s of His143	2.0
Structural Zn	Carboxylate oxygen atom of Asp146	1.9

The coordinating water is likely the catalytic nucleophile as it is hydrogen bound to the axial ligands, Asp116 (2.6 Å) and Asn216 (2.9 Å). Another active site residue, H114, is observed in two alternate conformations based on composite omit maps (Figures 50B). In one conformation (a), the N nitrogen atom of the imidazole ring is hydrogen bound to the coordinated water/hydroxide oxygen atom (2.9 Å) and the nitrogen atom (2.7 Å) of the axial ligand, Asn216. The second conformation (b) places the imidazole ring perpendicular to the imidazole ring in the (a) conformation resulting in the loss of hydrogen bonding interactions with both the coordinated water/hydroxide oxygen atom (5.4 Å) and possibly the nitrogen atom (3.1 Å) of the axial ligand Asn216. The structural Zn(II) ion is coordinated by the N nitrogen atoms of His143 (2.0 Å) and the carboxylate oxygen atom of Asp146 (1.9 Å) from each subunit (Figure 50C and 50D), providing a tetrahedral coordination geometry.

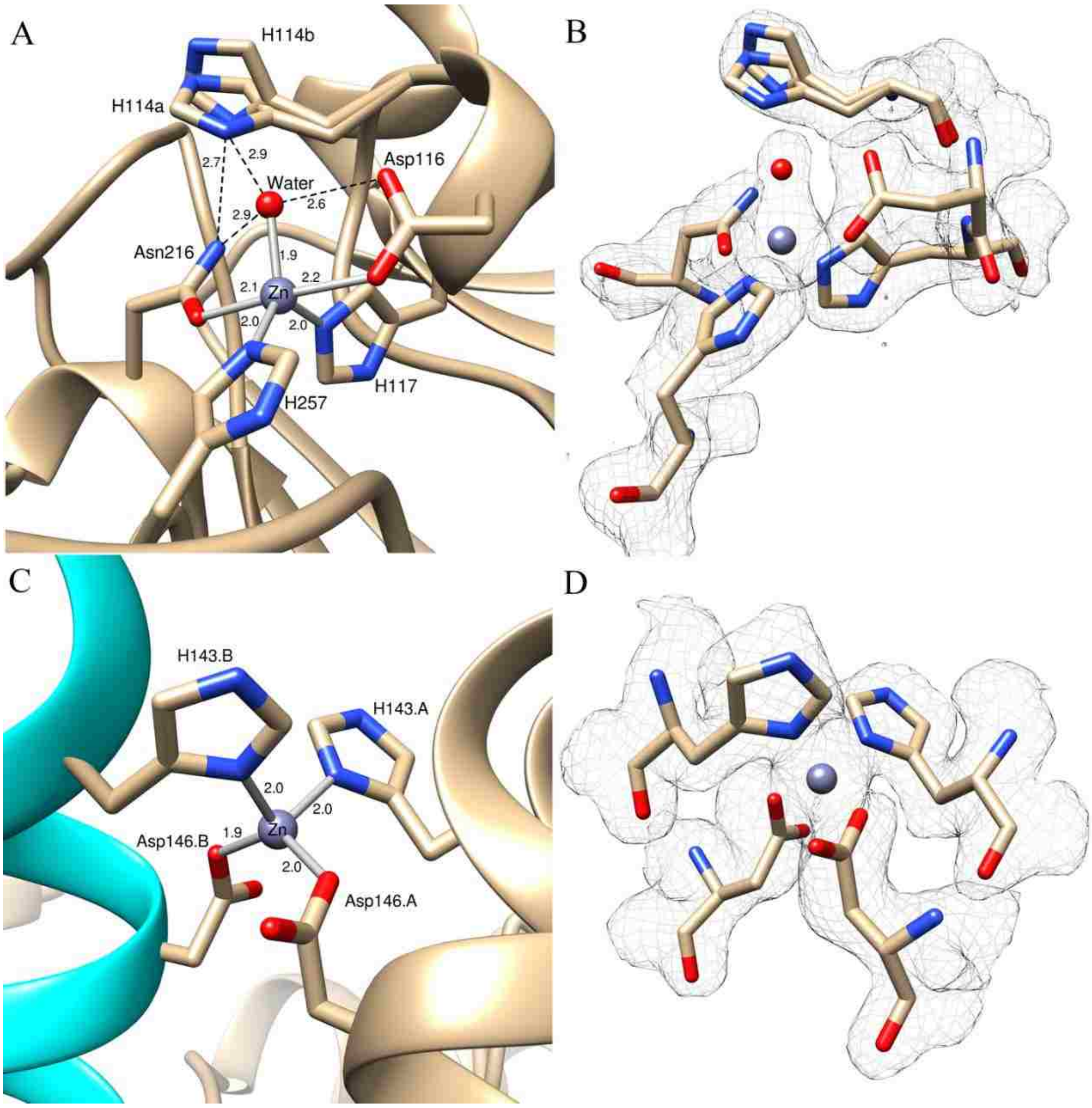

Figure 50. A) Chd^T active site. Zn(II)-ligand bonds are shown in gray sticks and hydrogen bonds are shown as black dashed lines. The key distances are shown in angstroms. The two alternate conformations of His114 are labeled as His114a and His114b. B) Simulated annealing composite omit maps (2F$_o$-F$_c$) are shown in grey mesh at the 1.0 sigma level for the coordinated residues, water, Zn(II), and His114. The residues are shown in the same orientations as that in A. C) The structural Zn(II) ion at the dimer interface. Zn(II)-ligand bonds are shown as gray sticks. One dimer is in tan, the other is in cyan. His143 and Asp146 from different subunits are indicated with “A” or “B”. D) The simulated annealing composite omit map (2F$_o$-F$_c$) is contoured at 1.0 sigma around the structural Zn(II) ion and its coordinated residues.

4.3.4 Role of the structural Zn(II) site

The structural Zn(II) site was eliminated by mutating both His143 and Asp146 to Ala. Removal of the structural Zn(II) site ligands had no apparent effect on Chd^{T} activity and the double mutant exhibited a k_{cat} of 25 ± 1, which is identical to that of wild-type Chd.[6, 97] Surprisingly, homodimer formation was also not affected based on gel filtration results (Figure 49). However, elimination of the structural Zn(II) site did increase the K_m value 2-fold ($K_m = 0.24 \pm 0.07$ μM) and severely affected protein stability as the purified mutant protein precipitated in ~2 hours when stored at room temperature.

4.3.5 Chd biological assembly in solution

The solution molecular weights of both the truncated and structural Zn(II) Chd mutants were obtained by MALDI-TOF Mass Spectrometry (Figure 51). Masses consistent with homodimer formation were observed as masses between 66 and 70 kDa.

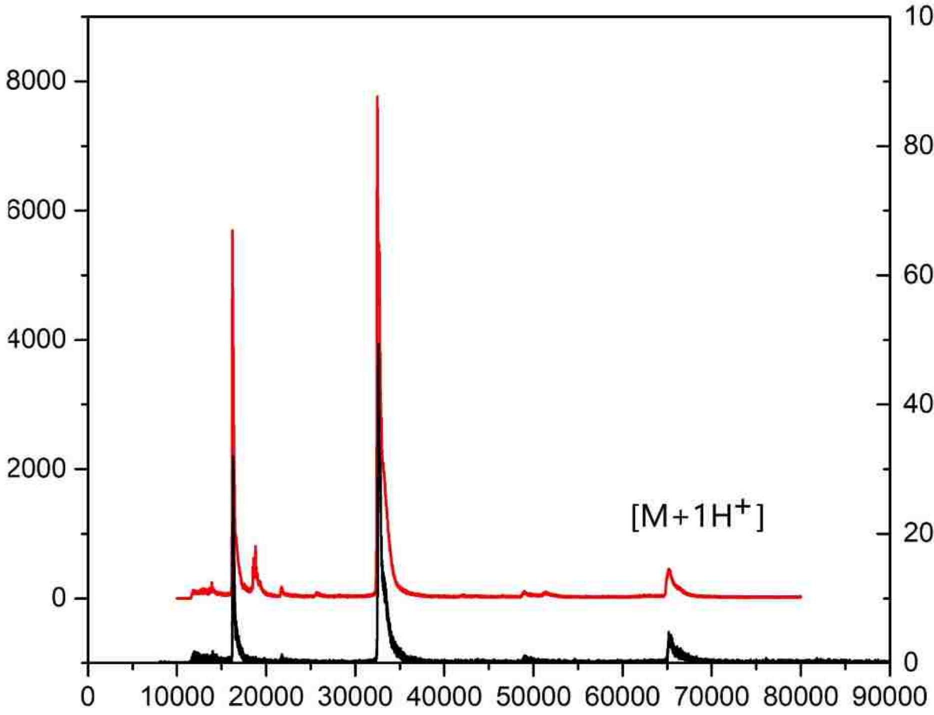

Figure 51. MALDI-TOF mass spectra of: **A)** truncated Chd^T (black) and the Chd^T double mutant (red).

These MS data are consistent with the observed molecular weight values for both samples determined by size exclusion chromatography, which indicate a molecular weight consistent with a homodimer in solution. It should also be noted that a small portion of Chd^T fragmented (<8%) during MALDI-TOF MS analysis.

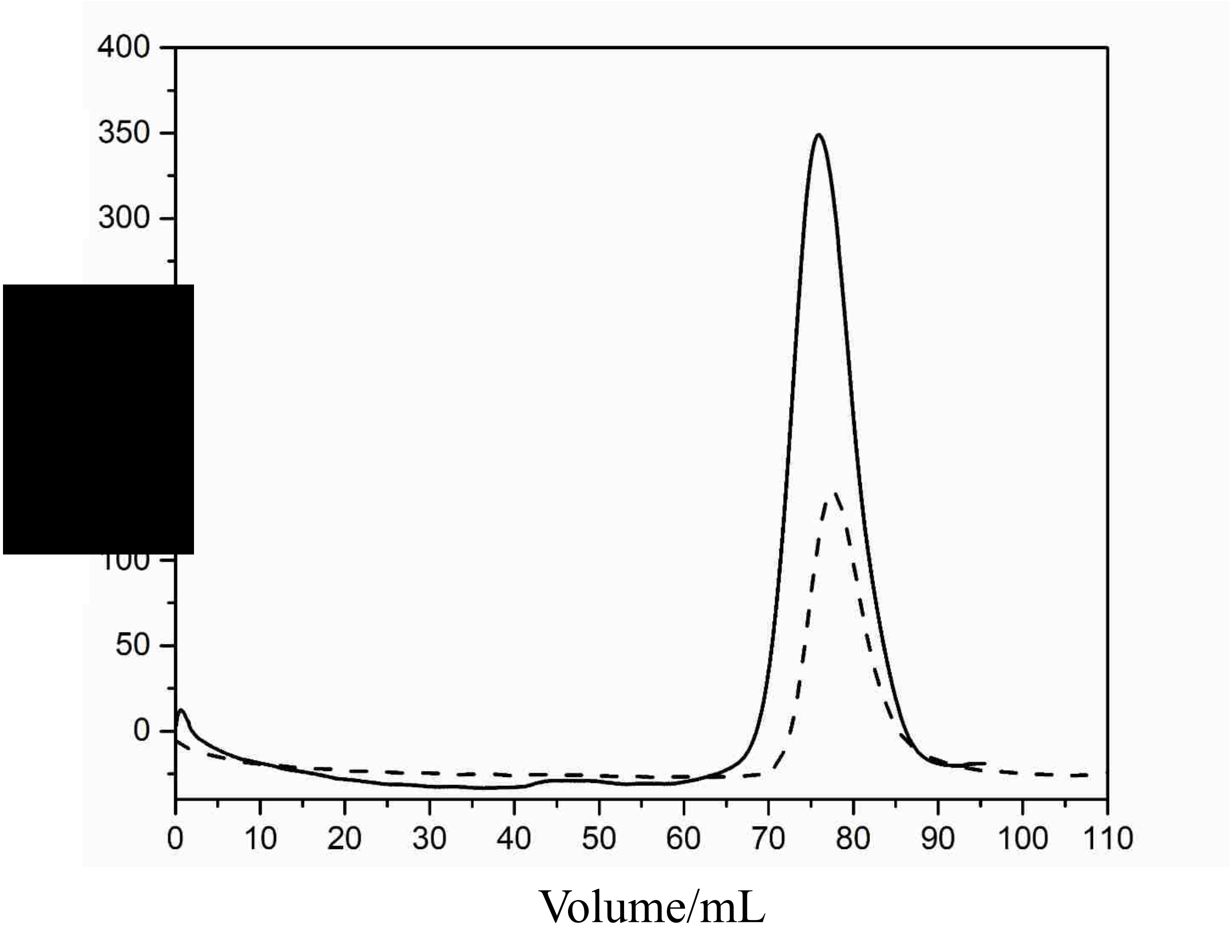

[redacted]

Figure 52. Size exclusion gel filtration chromatography curves of truncated Chd (solid line) and Chd mutant (dash line) by 50 mM HEPES buffer at pH 7 indicating both are homodimers in solution.

4.3.6 Substrate docking

Substrate docking generated four different poses ranked by the docking scoring function (Figure 53) [105]. The more negative the value indicates lower total energy after docking.[105, 109] The top ranked model (#1) suggests a binding interaction between a the nitrogen atom of a cyano nitrogen atom of TPN and the active site Zn (2.3 Å) along with an energetically favorable π- π interaction between the TPN aromatic ring and that of Trp227. Interestingly, this pose pre-organizes a possible transition state of TPN hydrolysis by placing the ortho carbon of TPN within 3.0 Å of the O atom of the bound water/hydroxide. In each of the other poses, all of the possible TPM ligating groups are too far away from the catalytic Zn(II) ion to be considered a bonding interaction (>3.5 Å). However, the model (#3) revealed a hydrogen bond between the nitrogen atom of a TPN cyano group and the amide nitrogen of the Zn(II) ligands Asn216 (2.3 Å). The resulting substrate position placed the ortho carbon of TPN within 3.1 Å of the O atom of the bound water/hydroxide. However, TPN is rotated in this pose, which abolished the energetically favorable π- π interaction between the TPN aromatic ring and that of Trp227.

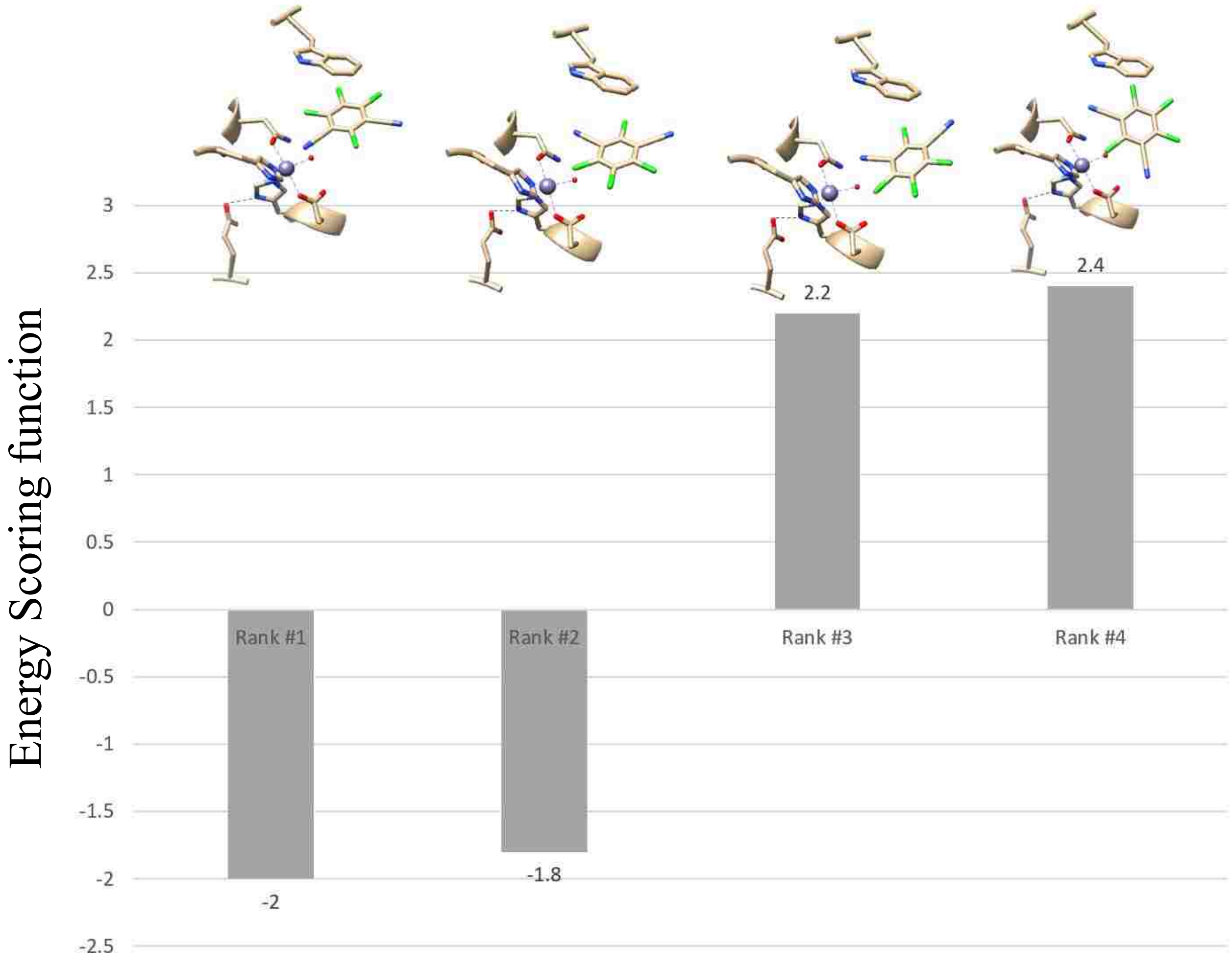

Figure 53. Four TPN docking poses for the active site of Chd^T. The best pose (#1) indicates ligation of a CN group from TPN to the active site Zn(II) ion.

4.3.7 Discussion

Chd^T is a "head-to-tail" homodimer, formed between two α-helices from each monomer, with three Zn(II) binding sites, in agreement with previous studies indicating ~1.5 Zn(II) ions bound per monomer, one of which is the active site Zn(II) while the third forms a structural site at the homodimer interface.[97] Chd^T has low sequence identity (<15%) compared to all protein structures deposited in the Protein Data Bank. According to Blast results, the most similar protein based on sequence is glyoxlase II (PDB code 1XM8) from *Arabidopsis thaliana* with a sequence identity of ~14.7% (48/327); therefore, the Chd^T structure is quite novel. Based on D.A.L.I. search results, the overall monomer protein fold largely matches those of two protein families (out of 16) and belongs to the metallo-β-lactamase (MBL) superfamily.[110] However, Chd^T contains an extra motif in each monomer that is not found in CphA, but aligned well with the dimerization domain of Pisa1.[108c] This motif had previously been reported to be part of the α-helical dimerization domain of Pisa1,[108c] which is a homodimer while most β-lactamase superfamily members are monomers. The observation of this extra C-terminal motif in Chd^T combined with the structural Zn(II) ion strongly suggests that the biologically relevant assembly of Chd^T is a homodimer. Size exclusion chromatography and MS data support a functional Chd^T homodimer with a molecular weight of ~70 kDa.

Chd^T contains a catalytic αββα-fold that is characteristic of Zn(II)-dependent MBL family members (Figure 49A). Three subgroups (B1, B2, and

B3) exist in this family that differ based on their sequence similarity and active site characteristics.[108a, b, 108d, 111] The B1 and B3 MBL subgroups contain dinuclear Zn(II) active sites,[108a, b, 111] while B2 enzymes utilize mononuclear Zn(II) active sites. However, B2 enzymes are capable of binding a second active site Zn(II) ion but this second Zn(II) ions is nonessential for catalysis. Chd most closely resembles the catalytic domain of a B2 MBL, such as ChpA,[112] which is rather selective towards a unique spectrum of substrates.[108b, 108d, 111] While Chd and CphA require a mononuclear Zn center for catalysis, Pisa1 and others in the sulfatase family require a dinuclear Zn(II) active site. It is likely that the overall fold of Chd represents an evolutionary connection between a B2 MBL and a sulfatase but has since undergone evolutionary modifications for its selective hydrolase activity towards TPN. Because Chd could not be clearly classified under any known family within the MBL superfamily, it is possible that it is a part of an unidentified subfamily belonging to the MBL superfamily. While some dehalogenases do not require co-enzymes for catalysis, such enzymes are only known to exists for alkyl and not aromatic substrates.[52b, 91]

The catalytic requirement of a mononuclear Zn(II) center in Chd is another shared characteristic with B2 MBLs and based on the X-ray crystal structure of Chd^T, only one Zn(II) ion is present in the active site. In addition, Chd^T contains a structural Zn(II) ion at the dimer interface that appears to stabilize the dimerization interaction. Two solvent accessible channels are observed in each monomer providing different routes for substrate and products to access/leave the catalytic Zn(II) site (Figure 48). As TPN is a rather hydrophobic substrate, replacement of an ortho-chlorine with an hydroxide produces more hydrophilic products, 4-OH-TPN, a chloride ion and a proton. As the products of TPN hydrolysis vary greatly in solubility and size, it would be reasonable to have two sets of solvent channels capable of shuttling different reactants and products to and from the active site. The "Y" shaped channel that originates on the "bottom" of the Chd homodimer contains a large opening (8.5 x 17.8 Å) with a channel that is largely hydrophobic. This "Y" shaped channel likely serves as a substrate recognition and binding site to guide TPN to the active site. On the other hand, water and H^+ and/or chloride ions can migrate through the second active site channel, which is more hydrophilic, and resides on the "top" side of the dimer. It has been reported that dimerization of SidA, which is an alkylsulfatase similar to Pisa1, ensures resistance to biocidic SDS at toxic concentrations.[113] Given that TPN is toxic, Chd may have evolved as a dimer with two active site channels to elicit a similar response.

The most common MBL active site binding motif (His-X-His-Asp-His) is partially present in Chd, as predicted by Wang *et al.*,[6] as the first His in the motif is replaced by a Ser (Ser112). This minor change in the MBL metal binding motif may explain why a dinuclear Zn(II) binding site does not occurr for Chd but is sometimes detected for MBLs. The active site Zn(II) ion in Chd^T resides in a solvent accessible trigonal bipyramidal (TBP) geometry that resembles the geometry of the "second" Zn(II) ion in MBL dinuclear Zn(II) active sites. On the other hand, the structural Zn(II) ion, which is coordinated by the N^{ε} nitrogen atom of a His143 and a carboxylate oxygen atom of Asp146 from each subunit (Figure 50), resides in a tetrahedral coordination geometry that is buried at the dimer interface. This structural Zn(II) ion is proposed to stabilize the homodimer.

When the coordinating residues H143 and Asp146 were eliminated by converting them to alanine's, the protein remained as a dimer in solution, based gel filtration and MS data. The catalytic capacity of the double mutant was indistinguishable from WT Chd, however, the K_m value doubled. Unfortunately, the double mutation reduced the stability of Chd^T as it precipitated within ~2 hours at room temperature. Based on these data, it is very likely that Chd^T is a homodimer in solution and that the homodimer is the biologically relevant assembly of Chd.

Several potentially important hydrogen-bonding interactions also exist in the active site of Chd^T. Perhaps most notably, there is at least one interaction between the metal bound water/hydroxide oxygen atom and the N^ε nitrogen atom of His114. His114 forms a strong hydrogen bond (~2.9 Å) with the equatorial metal bound water/hydroxide in Chd and also with the nitrogen atom of the axial Asn216 ligand (~2.7 Å). Interestingly, H114 clearly occupies two orientations, the second of which is perpendicular to the hydrogen bound confirmation, which places the N^ε nitrogen atom out of hydrogen bonding range of the metal-bound water/hydroxide (~5.4. Å) but close enough to the axial ligand Asn216 (~3.1 Å) to possibly form a hydrogen bond. The functional role of His114 and its flexibility is currently unknown but likely plays the catalytic role of general acid/base. This is consistent with both ChpA and Pisa1, as His114 is strictly conserved in both enzymes and in ChpA, it was also proposed to be the general acid to protonate the leaving group.[112] Other potentially important hydrogen bonding interactions occur between the Asn216 carboxamide nitrogen proton with the metal bound water/hydroxide (2.9 Å) and the second axial Asp116 ligand carboxylate oxygen also with the metal bound water/hydroxide (2.6 Å). These hydrogen bonding interactions likely assist in the deprotonation of the bound water to a nucleophilic hydroxide. Finally, a potentially important hydrogen bonding interaction occur between the N^{δ} proton of the His117 ligand with a side chain oxygen atom of Glu81 (~2.7 Å) forming an Glu-His-Zn triad that has been postulated to decrease the Lewis acidity of zinc ions[114] and may further assist in facilitating the coordination of substrate or water to the active site Zn(II) ion (Figure 50). Similar arrangements and a fully conserved Asp-His-Zn triads are observed for other hydrolases.[115]

The discovery of a large hydrophobic channel on the "bottom" of the Chd homodimer that provides access to the catalytic Zn(II) ion, suggests that it may serve as the substrate recognition and biding site. To properly position an aromatic substrate, such as TPN, for catalysis the substrate would need to either bind to or near the active site Zn(II) ion. Interestingly, Trp227 resides in the hydrophobic channel ~9.1 Å from the active site metal ion. Previous mutagenesis studies indicated that Trp227 is catalytically essential,[6] suggesting that it may be involved in recognizing and positioning TPN near the active site Zn(II) ion via a π-π interaction. To test this hypothesis, TPN was docked into the hydrophobic channel with the most energetically favorable pose occurring for a TPN orientation that maximizes the π-π interaction with Trp227, places a CN nitrogen atom within a bonding distance to the active site Zn(II) (~2.3 Å), and expands its coordination geometry to octahedral. As the C4 and C6 chlorines in TPN are chemically equivalent (homotopic) given the symmetry arising from the positions of the two CN substitutes, it does not matter which CN group binds to the active site Zn(II) ion. H114, which was proposed to function as the general acid/base during catalysis likely stabilizes the nucleophilic water/hydroxide and orients it for nucleophilic attack on TPN. In this pose, the C4/C6 chlorine would be positioned so that once the hydrolysis reaction occurs, the newly formed chloride ion would be oriented towards the small backend channel for expulsion to the bulk solvent. While a second pose was reasonably energetically favorable TPN was rotated which abolished the energetically favorable π- π interaction between the TPN aromatic ring and that of Trp227. While this pose is not as energetically favorable as the ligand TPN pose, it does reveal a hydrogen bond between the nitrogen atom of a TPN cyano group and the amide nitrogen Asn216, which places the ortho carbon of TPN within 3.1 Å of the O atom of the bound water/hydroxide.

4.4 Summary

In conclusion, to the best of our knowledge, the crystal structure of Chd^{T} is the first structure of a Zn(II)-dependent aromatic dehalogenase that does not require a coenzyme. The X-ray crystal structure of Chd^{T} also provides a structural, when used in connection with the previously reported kinetic studies on Chd, allows us to refine the recently proposed catalytic mechanism (Figure 45).[97] The first step in catalysis for Chd is likely recognition of TPN by the large hydrophobic channel that leads to the Zn(II) active site. TPN is proposed to be positioned by a π-π interaction with the catalytically essential active site residue Trp227 and supported by substrate docking studies.[6] Next, a CN nitrile nitrogen atom of TPN coordinates to Zn(II), expanding its coordination number from five to six. Binding of the substrate nitrile nitrogen has a two-fold impact. First, it removes electron density from the aromatic ring activating the ortho carbon for nucleophilic attack[95-97] and second, it activates the coordinated water/hydroxide for nucleophilic attack. Deprotonation of the metal-bound water molecule by His114, with assistance from the Zn(II) ligands Asp116 and Asn227, forms a nucleophilic hydroxide moiety, which is consistent with the postulated pK_a of the zinc-bound water molecule.[97, 116] Once the zinc-bound hydroxide is formed, it can attack the activated ortho carbon of TPN, forming an η-1-μ-transition-state complex (Figure 54).[117]

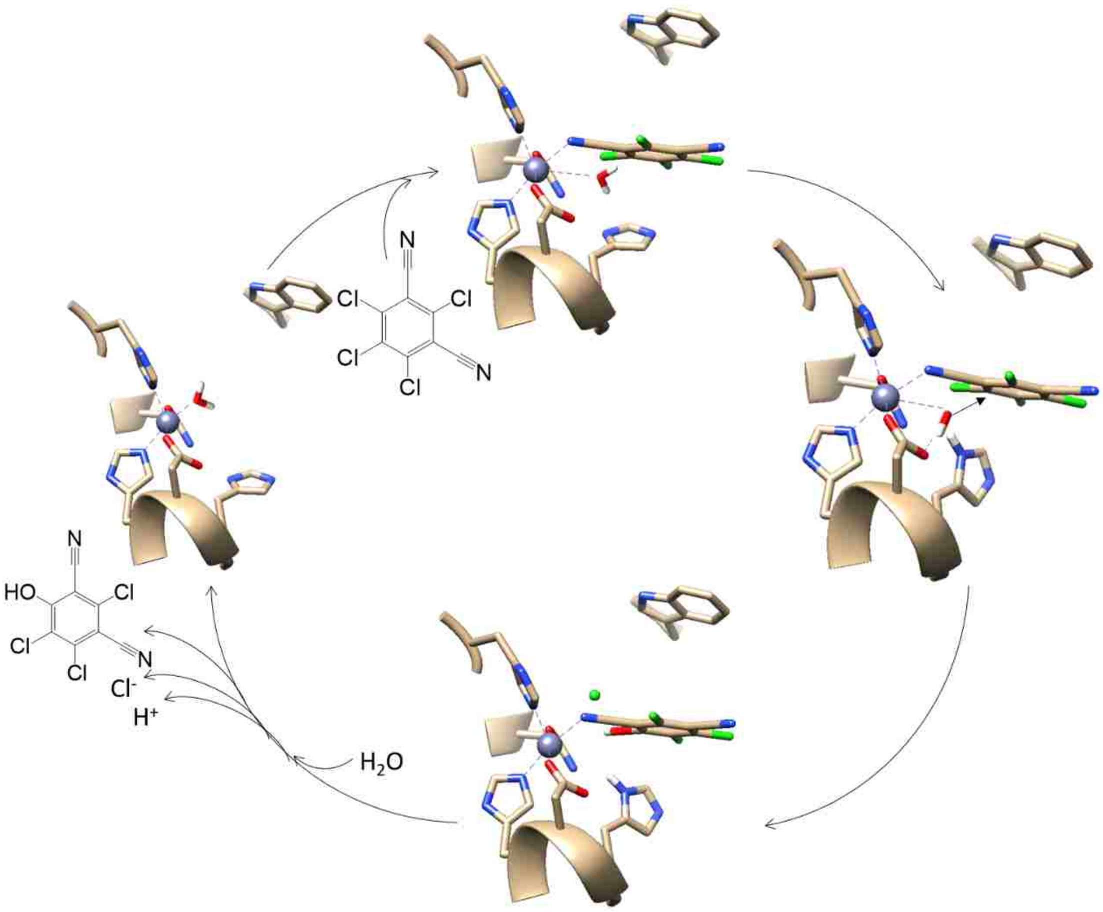

Figure 54. A revised catalytic mechanism for TPN hydrolysis by Chd.

Solvent kinetic isotope effect studies indicate that one proton is transferred in the transition-state, likely due to the breaking of a water O-H bond and the formation of a protonated His114.[97] The observed conformational flexibility of His114 may facilitate the formation of produces and enable product release. Once the products are released, the Zn(II)-bound water molecule is replaced. While a mechanism could also be proposed where a nitrile nitrogen atom of TPN does not bind to the active site Zn(II) ion, the substrate docking model supports Zn(II) binding and there is no residue other than the Zn(II) ligand Asn216 that could reasonably form a hydrogen bond to the nitrile nitrogen of TPN, which would be important for activating the substrate for hydrolysis.

CHAPTER FIVE RESERCH SUMMARY

Metalloenzymes play increasing important industrial roles in the chemistry fields related to water incorporation across CN and C-Cl bonds.[1] In this research, the structures and mechanisms of two novel enzymes that efficiently catalyze the hydration and hydrolysis reactions across CN and C-Cl bonds, respectively, were analyzed by biochemical, biophysical, computational modeling, crystallography, and spectroscopic approaches. These findings afforded in this thesis provide valuable mechanistic insight into developing biomimetic complexes.[118]

Within the eukaryotic nitrile hydratase work, the self-activation ability of an eukaryotic NHase – *Mb*NHase was supported by gene modification and enzyme preparations under different conditions. *Mb*NHase was found to have a similar active site and reaction mechanism compared to prokaryotic Co-type NHase enzymes that require accessory proteins for enzyme activation. The data presented also found that the unique insert sequence containing a histidine-rich region, assisted in enzyme activation and stabilization. However, *Mb*NHase still retained its ability to incorporate metal ions into the active site in the absence of the insert region. The accessory protein from other Co-type NHase enzymes not only improved enzyme activity but assisted in the post-translational modification required for activity.

To further explore how *Mb*NHase undergoes self-activation, the structural details around the active site should be determined by X-ray crystallography approaches. Unfortunately, X-ray quality crystals were not obtained. Moreover, the region critical for enzyme activation also remains to be analyzed by more genetic methods including site direct mutagenesis and direct evolution technics.

In the hydrolase research, a proposed mechanism of action for a novel chlorothalonil (TPN) dehalogenase (Chd) was developed. To accomplish this, a new continuous spectrophotometric assay for Chd was developed.[66b] This assay allowed the direct detection of a Chd reaction intermediate using stopped-flow spectroscopy with TPN as the substrate. Most of the kinetic results were carried out with high R^2 (>0.98) values and confirmed by multiple replications. The combination of these data with metal binding and kinetic studies, including pH and solvent isotope effect studies, allowed us to propose the first catalytic mechanism for Chd. The X-ray crystal structure of Chd provided valuable structural information with insight into how Chd recognizes and binds substrate. Confirmation of how substrate binds to Chd will need to be determined by mutagenesis and spectroscopic methods.

Because of precipitation problems, the first crystal structure of Chd was obtained by removing the first fifteen residues from the N-terminus. Thus, the removal of these fifteen residues, which contains two Cys amino acids, eliminated the precipitation problems and allowed Chd to remain soluble at high protein concentration (>10 mg/mL). Obtaining the X-ray crystal structure provided valuable information in support of the kinetic studies. First, Chd is a “head-to-tail” homodimer, formed between two α-helices from each monomer. It binds three Zn(II) ions, two of which are mononuclear active site Zn(II) ions in each monomer, while the third forms a structural site at the homodimer interface.[66b, 119] The active site Zn(II) ion is five coordinate with His117, His257, Asp116, Asn216, and water/hydroxide as ligands forming a distorted trigonal bipyramid or TBP active site. The structure also revealed a Y-shaped channel leading to the active site Zn(II) ion, which was proposed to recognize and bind substrate, pre-organizing it for hydrolysis relative to the active site Zn(II) ion. Substrate docking poses suggest that a CN group of TPN can bind to the active site Zn(II) ion, orienting orthro carbon of TPN with the nucleophilic Zn(II)-bound water/hydroxide molecule that also forms a hydrogen bond His114, which was proposed to function as the catalytic acid/base. A mechanism where a CN nitrogen atom of TPN does not bind to the active site Zn(II) ion was also proposed that would likely require an active site acid to form a hydrogen bonds to the CN group. However, no such acid was observed in the X-ray crystal structure suggesting this is not likely the mechanism of action for Chd. Even so, this type of mechanism cannot be eliminated at this point. A second coordination sphere residue, Glu81, forms a Glu-His-Zn triad, which likely functions to tune the Lewis acidity of the active site Zn(II) ion.[115] However, the proposed catalytic functions of both His114 and Glu81 remain to be determined by future work that includes site-directed mutagenesis of both residues, followed by spectroscopic and crystallization experiments in the absence and presence of TPN.

Bibliography

1. (a) Kobayashi, M.; Shimizu, S., Metalloenzyme nitrile hydratase: structure, regulation, and application to biotechnology. *Nat Biotechnol* **1998,** *16* (8), 733-6; (b) McCall, K. A.; Huang, C.; Fierke, C. A., Function and mechanism of zinc metalloenzymes. *J Nutr* **2000,** *130* (5S Suppl), 1437S-46S.

2. Prasad, S.; Bhalla, T. C., Nitrile hydratases (NHases): at the interface of academia and industry. *Biotechnol Adv* **2010,** *28* (6), 725-41.

3. Barber, J., Photosystem II: the water-splitting enzyme of photosynthesis. *Cold Spring Harb Symp Quant Biol* **2012,** *77*, 295-307.

4. Chen, Z.; Sun, X. D.; Shi, Y.; Shen, Z. Y.; Zhao, J. X.; Sun, X. Y., [Study on production of acrylamide by microbial method (I)--Culture of bacterium cells and expression of high activity of nitrile hydratase]. *Sheng Wu Gong Cheng Xue Bao* **2002,** *18* (1), 55-8.

5. Howden, A. J.; Preston, G. M., Nitrilase enzymes and their role in plant-microbe interactions. *Microb Biotechnol* **2009,** *2* (4), 441-51.

6. Wang, G.; Li, R.; Li, S.; Jiang, J., A novel hydrolytic dehalogenase for the chlorinated aromatic compound chlorothalonil. *J Bacteriol* **2010,** *192* (11), 2737-45.

7. Wyatt, J. M.; Linton, E. A., The industrial potential of microbial nitrile biochemistry. *Ciba Found Symp* **1988,** *140*, 32-48.

8. (a) Ramteke, P. W.; Maurice, N. G.; Joseph, B.; Wadher, B. J., Nitrile-converting enzymes: an eco-friendly tool for industrial biocatalysis. *Biotechnol Appl Biochem* **2013,** *60* (5), 459-81; (b) Howden, A. J. M.; Preston, G. M., Nitrilase enzymes and their role in plant-microbe interactions. *Microbial biotechnology* **2009,** *2* (4), 441-451.

9. Banerjee, A.; Sharma, R.; Banerjee, U., RETRACTED ARTICLE: The nitrile-degrading enzymes: current status and future prospects. *Applied Microbiology and Biotechnology* **2002,** *60* (1), 33-44.

10. Nomura, J.; Hashimoto, H.; Ohta, T.; Hashimoto, Y.; Wada, K.; Naruta, Y.; Oinuma, K.; Kobayashi, M., Crystal structure of aldoxime dehydratase and its catalytic mechanism involved in carbon-nitrogen triple-bond synthesis. *Proc Natl Acad Sci U S A* **2013,** *110* (8), 2810-5.

11. Zhang, X. H.; Liu, Z. Q.; Xue, Y. P.; Xu, M.; Zheng, Y. G., Nitrilase-catalyzed conversion of (R,S)-mandelonitrile by immobilized recombinant Escherichia coli cells harboring nitrilase. *Biotechnol Appl Biochem* **2016,** *63* (4), 479-89.

12. Schrauzer, G. N.; Doemeny, P. A.; Kiefer, G. W.; Frazier, R. H., Chemical evolution of a nitrogenase model. IV. Reduction of isonitriles. *J Am Chem Soc* **1972,** *94* (10), 3604-13.

13. Lavrov, K. V.; Karpova, I. Y.; Epremyan, A. S.; Yanenko, A. S., [Cloning and analysis of a new aliphatic amidase gene from Rhodococcus erythropolis TA37]. *Genetika* **2014,** *50* (10), 1145-53.

14. (a) Gong, J. S.; Lu, Z. M.; Li, H.; Shi, J. S.; Zhou, Z. M.; Xu, Z. H., Nitrilases in nitrile biocatalysis: recent progress and forthcoming research. *Microb Cell Fact* **2012,** *11*, 142; (b) Coffey, L.; Clarke, A.; Duggan, P.; Tambling, K.; Horgan, S.; Dowling, D.; O'Reilly, C., Isolation of identical nitrilase genes from multiple bacterial strains and real-time PCR detection of the genes from soils provides evidence of horizontal gene transfer. *Arch Microbiol* **2009,** *191* (10), 761-71; (c) Oinuma, K.; Hashimoto, Y.; Konishi, K.; Goda, M.; Noguchi, T.; Higashibata, H.; Kobayashi, M., Novel aldoxime dehydratase involved in carbon-nitrogen triple bond synthesis of Pseudomonas chlororaphis B23. Sequencing, gene expression, purification, and characterization. *J Biol Chem* **2003,** *278* (32), 29600-8; (d) Kato, Y.; Ooi, R.; Asano, Y., Distribution of aldoxime dehydratase in microorganisms. *Appl Environ Microbiol* **2000,** *66* (6), 2290-6.

15. Cassidy, M. P.; Raushel, J.; Fokin, V. V., Practical synthesis of amides from in situ generated copper(I) acetylides and sulfonyl azides. *Angew Chem Int Ed Engl* **2006,** *45* (19), 3154-7.

16. (a) Pratush, A.; Seth, A.; Bhalla, T. C., Cloning, sequencing, and expression of nitrile hydratase gene of mutant 4D strain of Rhodococcus rhodochrous PA 34 in E. coli. *Appl Biochem Biotechnol* **2012,** *168* (3), 465-86; (b) Kuhn, M. L.; Martinez, S.; Gumataotao, N.; Bornscheuer, U.; Liu, D.; Holz, R. C., The Fe-type nitrile hydratase from Comamonas testosteroni Ni1 does not require an activator accessory protein for expression in Escherichia coli. *Biochemical and Biophysical Research Communications* **2012,** *424* (3), 365-370.

17. Miyanaga, A.; Fushinobu, S.; Ito, K.; Wakagi, T., Crystal structure of cobalt-containing nitrile hydratase. *Biochemical and Biophysical Research Communications* **2001,** *288* (5), 1169-74.

18. Foerstner, K. U.; Doerks, T.; Muller, J.; Raes, J.; Bork, P., A nitrile hydratase in the Eukaryote *Monosiga brevicollis*. *PLoS ONE* **2008,** *3* (12), e3976.

19. Yamanaka, Y.; Kato, Y.; Hashimoto, K.; Iida, K.; Nagasawa, K.; Nakayama, H.; Dohmae, N.; Noguchi, K.; Noguchi, T.; Yohda, M.; Odaka, M., Time-Resolved Crystallography of the Reaction Intermediate of Nitrile Hydratase: Revealing a Role for the Cysteinesulfenic Acid Ligand as a Catalytic Nucleophile. *Angew Chem Int Ed Engl* **2015,** *54* (37), 10763-7.

20. (a) Blackwell, A. E.; Dodds, E. D.; Bandarian, V.; Wysocki, V. H., Revealing the quaternary structure of a heterogeneous noncovalent protein complex through surface-induced dissociation. *Anal Chem* **2011,** *83* (8), 2862-5; (b) Nelp, M. T.; Astashkin, A. V.; Breci, L. A.; McCarty, R. M.; Bandarian, V., The Alpha Subunit of Nitrile Hydratase Is Sufficient for Catalytic Activity and Post-Translational Modification. *Biochemistry* **2014,** *53* (24), 3990-3994.

21. Mitra, S.; Holz, R. C., Unraveling the catalytic mechanism of nitrile hydratases. *J Biol Chem* **2007,** *282* (10), 7397-404.

22. Liu, Y.; Cui, W.; Xia, Y.; Cui, Y.; Kobayashi, M.; Zhou, Z., Self-Subunit Swapping Occurs in Another Gene Type of Cobalt Nitrile Hydratase. *PLOS ONE* **2012,** *7* (11), e50829.

23. Zhou, Z.; Hashimoto, Y.; Kobayashi, M., Self-subunit swapping chaperone needed for the maturation of multimeric metalloenzyme nitrile hydratase by a subunit exchange mechanism also carries out the oxidation of the metal ligand cysteine residues and insertion of cobalt. *J Biol Chem* **2009,** *284* (22), 14930-8.

24. (a) Miyanaga, A.; Fushinobu, S.; Ito, K.; Shoun, H.; Wakagi, T., Mutational and structural analysis of cobalt-containing nitrile hydratase on substrate and metal binding. *Eur J Biochem* **2004,** *271* (2), 429-38; (b) Nojiri, M.; Nakayama, H.; Odaka, M.; Yohda, M.; Takio, K.; Endo, I., Cobalt-substituted Fe-type nitrile hydratase of Rhodococcus sp. N-771. *FEBS Lett* **2000,** *465* (2-3), 173-7.

25. Sari, M. A.; Jaouen, M.; Saroja, N. R.; Artaud, I., Influence of cobalt substitution on the activity of iron-type nitrile hydratase: are cobalt type nitrile hydratases regulated by carbon monoxide? *J Inorg Biochem* **2007,** *101* (4), 614-22.

26. Huang, W.; Jia, J.; Cummings, J.; Nelson, M.; Schneider, G.; Lindqvist, Y., Crystal structure of nitrile hydratase reveals a novel iron centre in a novel fold. *Structure* **1997,** *5* (5), 691-9.

27. (a) Light, K. M.; Yamanaka, Y.; Odaka, M.; Solomon, E. I., Spectroscopic and Computational Studies of Nitrile Hydratase: Insights into Geometric and Electronic Structure and the Mechanism of Amide Synthesis. *Chem Sci* **2015,** *6* (11), 6280-6294; (b) Martinez, S.; Wu, R.; Sanishvili, R.; Liu, D.; Holz, R., The Active Site Sulfenic Acid Ligand in Nitrile Hydratases Can Function as a Nucleophile. *J Am Chem Soc* **2014,** *136* (4), 1186-1189.

28. Marron, A. O.; Akam, M.; Walker, G., Nitrile Hydratase Genes Are Present in Multiple Eukaryotic Supergroups. *PLoS ONE* **2012,** *7* (4), e32867.

29. (a) Wainright, P.; Hinkle, G.; Sogin, M.; Stickel, S., Monophyletic origins of the metazoa: an evolutionary link with fungi. *Science* **1993,** *260* (5106), 340-342; (b) Snell, E. A.; Furlong, R. F.; Holland, P. W. H., Hsp70 sequences indicate that choanoflagellates are closely related to animals. *Current Biology* **2001,** *11* (12), 967-970; (c) King, N.; Carroll, S. B., A receptor tyrosine kinase from choanoflagellates: Molecular insights into early animal evolution. *Proceedings of the National Academy of Sciences* **2001,** *98* (26), 15032-15037; (d) Karpov, S. A.; Mylnikov, A. P., Preliminary observations on the ultrastructure of mitosis in choanoflagellates. *European Journal of Protistology* **1993,** *29* (1), 19-23; (e) Karpov, S. A.; Leadbeater, B. S. C., Cell and nuclear division in a freshwater choanoflagellate, Monosiga ovata Kent. *European Journal of Protistology* **1997,** *33* (3), 323-334; (f) Karpov, S. A.; Leadbeater, B. S. C., Cytoskeleton Structure and Composition in Choanoflagellates. *Journal of Eukaryotic Microbiology* **1998,** *45* (3), 361-367; (g) Hibberd, D. J., Observations on the ultrastructure of the choanoflagellate Codosiga botrytis (Ehr.) Saville-Kent with special reference to

the flagellar apparatus. *J Cell Sci* **1975,** *17* (1), 191-219; (h) Jens, B.; Hartmut, A., Comparative studies on the feeding behavior of two heterotrophic nanoflagellates: the filter-feeding choanoflagellate Monosiga ovata and the raptorial-feeding kinetoplastid Rhynchomonas nasuta. *Aquatic Microbial Ecology* **2000,** *22* (3), 243-249.

30. Xia, Y.; Cui, W.; Liu, Z.; Zhou, L.; Cui, Y.; Kobayashi, M.; Zhou, Z., Construction of a subunit-fusion nitrile hydratase and discovery of an innovative metal ion transfer pattern. *Sci Rep* **2016,** *6*, 19183.

31. (a) Ge, R.; Watt, R. M.; Sun, X.; Tanner, J. A.; He, Q. Y.; Huang, J. D.; Sun, H., Expression and characterization of a histidine-rich protein, Hpn: potential for Ni2+ storage in Helicobacter pylori. *Biochem J* **2006,** *393* (Pt 1), 285-93; (b) Gilbert, J. V.; Ramakrishna, J.; Sunderman, F. W., Jr.; Wright, A.; Plaut, A. G., Protein Hpn: cloning and characterization of a histidine-rich metal-binding polypeptide in Helicobacter pylori and Helicobacter mustelae. *Infect Immun* **1995,** *63* (7), 2682-8; (c) Higgins, K. A.; Carr, C. E.; Maroney, M. J., Specific metal recognition in nickel trafficking. *Biochemistry* **2012,** *51* (40), 7816-32.

32. Szponarski, M.; Schwizer, F.; Ward, T. R.; Gademann, K., On-cell catalysis by surface engineering of live cells with an artificial metalloenzyme. *Communications Chemistry* **2018,** *1* (1), 84.

33. Bloom, J. Reregistration Eligibility Decision Chlorothalonil. https://archive.epa.gov/pesticides/reregistration/web/pdf/0097red.pdf (accessed June 3).

34. Schecter, A.; Cramer, P.; Boggess, K.; Stanley, J.; Papke, O.; Olson, J.; Silver, A.; Schmitz, M., Intake of dioxins and related compounds from food in the U.S. population. *J Toxicol Environ Health A* **2001,** *63* (1), 1-18.

35. Tillman, R. W.; Siegel, M. R.; Long, J. W., Mechanism of action and fate of the fungicide chlorothalonil (2,4,5,6-tetrachloroisophthalonitrile) in biological systems: I. Reactions with cells and subcellular components of Saccharomyces pastorianus. *Pesticide Biochemistry and Physiology* **1973,** *3* (2), 160-167.

36. Vickers, A. E.; Sloop, T. C.; Lucier, G. W., Mechanism of action of toxic halogenated aromatics. *Environ Health Perspect* **1985,** *59*, 121-8.

37. Mozzachio, A. M.; Rusiecki, J. A.; Hoppin, J. A.; Mahajan, R.; Patel, R.; Beane-Freeman, L.; Alavanja, M. C., Chlorothalonil exposure and cancer incidence among pesticide applicator participants in the agricultural health study. *Environmental research* **2008,** *108* (3), 400-3.

38. Carlo-Rojas, Z.; Bello-Mendoza, R.; Figueroa, M. S.; Sokolov, M., Chlorothalonil Degradation under Anaerobic Conditions in an Agricultural Tropical Soil. *Water, Air, & Soil Pollution* **2004,** *151*, 397-409

39. (a) Copley, S. D., Microbial dehalogenases: enzymes recruited to convert xenobiotic substrates. *Curr. Opin. Chem. Biol.* **1998,** *2*, 613-7; (b) Janssen, D. B.;

Oppentocht, J. E.; Poelarends, G. J., Microbial dehalogenation. *Curr. Opin. Biotechnol.* **2001,** *12*, 254-258.

40. Slater, J. H.; Bull, A. T.; Hardman, D. J., Microbial dehalogenation of halogenated alkanoic acids, alcohols and alkanes. *Advances in microbial physiology* **1997,** *38*, 133-76.

41. Viciu, M. S.; Grasa, G. A.; Nolan, S. P., Catalytic Dehalogenation of Aryl Halides Mediated by a Palladium/Imidazolium Salt System. *Organometallics* **2001,** *20* (16), 3607-3612.

42. Leisinger, T.; Bader, R.; Hermann, R.; Schmid-Appert, M.; Vuilleumier, S., Microbes, enzymes and genes involved in dichloromethane utilization. *Biodegradation* **1994,** *5* (3-4), 237-48.

43. (a) Reddy, G. V.; Gold, M. H., Degradation of pentachlorophenol by Phanerochaete chrysosporium: intermediates and reactions involved. *Microbiology* **2000,** *146 (Pt 2)*, 405-13; (b) Beil, S.; Mason, J. R.; Timmis, K. N.; Pieper, D. H., Identification of chlorobenzene dioxygenase sequence elements involved in dechlorination of 1,2,4,5-tetrachlorobenzene. *Journal of bacteriology* **1998,** *180* (21), 5520-8; (c) Xun, L.; Topp, E.; Orser, C. S., Purification and characterization of a tetrachloro-p-hydroquinone reductive dehalogenase from a Flavobacterium sp. *Journal of bacteriology* **1992,** *174* (24), 8003-7; (d) Orser, C. S.; Dutton, J.; Lange, C.; Jablonski, P.; Xun, L.; Hargis, M., Characterization of a Flavobacterium glutathione S-transferase gene involved reductive dechlorination. *Journal of bacteriology* **1993,** *175* (9), 2640-4; (e) Yokota, T.; Fuse, H.; Omori, T.; Minora, Y., Microbial dehalogenation of haloalkanes mediated byoxy genases or halidohydrolase. *Agric. Biol. Chem.* **1986,** *50*, 453–460.

44. Bunge, M., .; Adrian, L.; Kraus, A.; Opel, M.; Lorenz, W. G.; Andreesen, J. R.; Görisch, H.; Lechner, U., Reductive dehalogenation of chlorinated dioxins by an anaerobic bacterium. *Nature* **2003,** *421*, 357-60.

45. (a) van der Ploeg, J.; van Hall, G.; Janssen, D. B., Characterization of the haloacid dehalogenase from Xanthobacter autotrophicus GJ10 and sequencing of the dhlB gene. *Journal of bacteriology* **1991,** *173* (24), 7925-33; (b) Verschueren, K. H.; Seljée, F.; Rozeboom, H. J.; Kalk, K. H.; Dijkstra, B. W., Crystallographic analysis of the catalytic mechanism of haloalkane dehalogenase. *Nature* **1993,** *363*, 693-8.

46. Yokota, T.; Fuse, H.; Omori, T.; Minoda, Y., Microbial Dehalogenation of Haloalkanes Mediated by Oxygenase or Halidohydrolase. *Agricultural and Biological Chemistry* **1986,** *50* (2), 453-460.

47. Bunge, M.; Adrian, L.; Kraus, A.; Opel, M.; Lorenz, W. G.; Andreesen, J. R.; Gorisch, H.; Lechner, U., Reductive dehalogenation of chlorinated dioxins by an anaerobic bacterium. *Nature* **2003,** *421* (6921), 357-60.

48. Verschueren, K. H.; Seljee, F.; Rozeboom, H. J.; Kalk, K. H.; Dijkstra, B. W., Crystallographic analysis of the catalytic mechanism of haloalkane dehalogenase. *Nature* **1993,** *363* (6431), 693-8.

49. (a) Scholten, J. D.; Chang, K. H.; Babbitt, P. C.; Charest, H.; Sylvestre, M.; Dunaway-Mariano, D., Novel enzymic hydrolytic dehalogenation of a chlorinated aromatic. *Science* **1991,** *253* (5016), 182-5; (b) Schmitz, A.; Gartemann, K. H.; Fiedler, J.; Grund, E.; Eichenlaub, R., Cloning and sequence analysis of genes for dehalogenation of 4-chlorobenzoate from Arthrobacter sp. strain SU. *Appl Environ Microbiol* **1992,** *58* (12), 4068-71.

50. Frere, J. M., Beta-lactamases and bacterial resistance to antibiotics. *Mol Microbiol* **1995,** *16* (3), 385-95.

51. Sakkas, V. A.; Lambropoulou, D. A.; Albanis, T. A., Study of chlorothalonil photodegradation in natural waters and in the presence of humic substances. *Chemosphere* **2002,** *48* (9), 939-45.

52. (a) Ukrainczyk, L.; Chibwe, M.; Pinnavaia, T. J.; Boyd, S. A., Reductive Dechlorination of Carbon Tetrachloride In Water Catalyzed by Mineral-Supported Biomimetic Cobalt Macrocycles. *Environmental Science & Technology* **1995,** *29* (2), 439-445; (b) de Jong, R. M.; Dijkstra, B. W., Structure and mechanism of bacterial dehalogenases: different ways to cleave a carbon-halogen bond. *Current opinion in structural biology* **2003,** *13* (6), 722-30.

53. Reprint with permission-Yang, X.; Bennett, B.; Holz, R. C., Analyzing the function of the insert region found between the α and β-subunits in the eukaryotic nitrile hydratase from Monosiga brevicollis. *Arch Biochem Biophys* **2018,** *657*, 1-7.

54. (a) Kovacs, J. A., Synthetic analogues of cysteinate-ligated non-heme iron and non-corrinoid cobalt enzymes. *Chem Rev.* **2004,** *104*, 825-848; (b) Harrop, T. C.; Mascharak, P. K., Fe(III) and Co(III) centers with carboxamido nitrogen and modified sulfur coordination: lessons learned from nitrile hydratase. *Acc Chem Res.* **2004,** *37*, 253-260.

55. (a) Kobayashi, M.; Nagasawa, T.; Yamada, H., Enzymatic synthesis of acrylamide: a success story not yet over. *Trends Biotechnol.* **1992,** *10*, 402–408; (b) Nagasawa, T.; Shimizu, H.; Yamada, H., The superiority of the third-generation catalyst, Rhodococcus rhodochrous J1 nitrile hydratase, for industrial production of acrylamide. *Appl. Microbiol. Biotechnol.* **1993,** *40* (189–195); (c) Nagasawa, T.; Yamada, H., Microbial production of commodity chemicals. *Pure Appl. Chem.* **1995,** *67*, 1241–1256; (d) Yamada, H.; Kobayashi, M., Hydratases involved in nitrile conversion: Screening, characterization and application. *Biosci. Biotech. Biochem.* **1996,** *60*, 1391-1400; (e) Prasad, S.; Bhalla, T. C., Nitrile hydratases (NHases): At the interface of academia and industry. *Biotechnology Advances* **2010,** *28* (6), 725-741; (f) Nagasawa, T.; Mathew, C. D.; Mauger, J.; Yamada, H., Nitrile Hydratase-Catalyzed Production of Nicotinamide from 3-Cyanopyridine in Rhodococcus rhodochrous J1. *Appl. Environ. Microbiol.* **1988,** *54*, 1766-1760.

56. Martinez, S.; Yang, X.; Bennett, B.; Holz, R. C., A cobalt-containing eukaryotic nitrile hydratase. *Biochimica et Biophysica Acta (BBA) - Proteins and Proteomics* **2017,** *1865* (1), 107-112.

57. (a) Tsujimura, M.; Odaka, M.; Nakayama, H.; Dohmae, N.; Koshino, H.; Asami, T.; Hoshino, M.; Takio, K.; Yoshida, S.; Maeda, M.; Endo, I., A novel inhibitor for Fe-type nitrile hydratase: 2-cyano-2-propyl hydroperoxide. *J Am Chem Soc.* **2003,** *125*, 11532-11538; (b) Dey, A.; Chow, M.; Taniguchi, K.; Lugo-Mas, P.; Davin, S.; Maeda, M.; Kovacs, J. A.; Odaka, M.; Hodgson, K. O.; Hedman, B.; Solomon, E. I., Sulfur K-Edge XAS and DFT Calculations on Nitrile Hydratase: Geometric and Electronic Structure of the Non-heme Iron Active Site. *J. Am. Chem. Soc.* **2006,** *128*, 533 - 541.

58. (a) Nishiyama, M.; Horinouchi, S.; Kobayashi, M.; Nagasawa, T.; Yamada, H.; Beppu, T., Cloning and characterization of genes responsible for metabolism of nitrile compounds from Pseudomonas chlororaphis B23. *J. Bacteriol.* **1991,** *173* (8), 2465-2472; (b) Hashimoto Y., N., M., Horinouchi S., Beppu T., Nitrile hydratase gene from Rhodococcus sp. N-774 requirement for its downstream region for efficient expression *Bioscience, biotechnology, and biochemistry* **1994,** *58* (10), 1859-1869; (c) Nojiri, M.; Yohda, M.; Odaka, M.; Matsushita, Y.; Tsujimura, M.; Yoshida, T.; Dohmae, N.; Takio, K.; Endo, I., Functional Expression of Nitrile Hydratase in Escherichia coli: Requirement of a Nitrile Hydratase Activator and Post-Translational Modification of a Ligand Cysteine. *Journal of Biochemistry* **1999,** *125* (4), 696-704.

59. Mendel, R. R.; Smith, A. G.; Marquet, A.; Warren, M. J., Metal and cofactor insertion. *Natural Product Reports* **2007,** *24* (5), 963-971.

60. Higgins, K. A.; Carr, C. E.; Maroney, M. J., Specific Metal Recognition in Nickel Trafficking. *Biochemistry* **2012,** *51* (40), 7816-7832.

61. Portion reprint with permission-Martinez, S.; Yang, X.; Bennett, B.; Holz, R. C., A cobalt-containing eukaryotic nitrile hydratase. *Biochim Biophys Acta Proteins Proteom* **2017,** *1865* (1), 107-112.

62. Stevens, J. M.; Rao Saroja, N.; Jaouen, M.; Belghazi, M.; Schmitter, J.-M.; Mansuy, D.; Artaud, I.; Sari, M.-A., Chaperone-assisted expression, purification, and characterization of recombinant nitrile hydratase NI1 from Comamonas testosteroni. *Protein Expression and Purification* **2003,** *29* (1), 70-76.

63. Kovacs, J. A., Synthetic analogues of cysteinate-ligated non-heme iron and non-corrinoid cobalt enzymes. *Chem Rev* **2004,** *104* (2), 825-48.

64. (a) Caux, P. Y.; Kent, R. A.; Fan, G. T.; Stephenson G. L, Environmental fate and effects of chlorothalonil: A Canadian perspective *Crit. Rev. Environ. Sci. Technol.* **1996,** *26*, 45-93; (b) Sakkas, V. A.; Lambropoulou, D. A.; Albanis, T. A., Study of chlorothalonil photodegradation in natural waters and in the presence of humic substances. *Chemosphere* **2002,** *48*, 939-945.

65. Kwon, J. W.; Armbrust, K. L., Degradation of chlorothalonil in irradiated water/sediment systems. *Journal of agricultural and food chemistry* **2006,** *54* (10), 3651-7.

66. (a) Vickers, A.; Sloop, T.; Lucier, G., Mechanism of Action of Toxic Halogenated Aromatics. *Environ Health Perspect.* **1985,** *59*, 121-126; (b) Wang,

G.; Li, R.; Li, S.; Jiang, J., A Novel Hydrolytic Dehalogenase for the Chlorinated Aromatic Compound Chlorothalonil. *J. Bacteriol.* **2010,** *192*, 2737–2745.

67. (a) Liang, B.; Wang, G.; Zhao, Y.; Chen, K.; Li, S.; Jiang, J., Facilitation of bacterial adaptation to chlorothalonil-contaminated sites by horizontal transfer of the chlorothalonil hydrolytic dehalogenase gene. *Applied and environmental microbiology* **2011,** *77* (12), 4268-72; (b) Ren, X.; Li, H.; Chen, S., Cloning of the chlorothalonil-degrading gene cluster and evidence of its horizontal transfer. *Current microbiology* **2011,** *62* (3), 1068-73; (c) Yue, W.; Xiong, M.; Li, F.; Wang, G., The isolation and characterization of the novel chlorothalonil-degrading strain Paracoccus sp. XF-3 and the cloning of the chd gene. *Journal of bioscience and bioengineering* **2015,** *120* (5), 544-8.

68. Chen, H.; Wang, H.; Wang, T.; Huang, S.; Zang, X.; Li, S.; Jiang, J., Identification of the metal center of chlorothalonil hydrolytic dehalogenase and enhancement of catalytic efficiency by directed evolution. *Applied Environmental Biotechnology* **2016,** *1*, 30-37.

69. D'Souza V, M.; Bennett, B.; Copik, A. J.; Holz, R. C., Divalent metal binding properties of the methionyl aminopeptidase from Escherichia coli. *Biochemistry* **2000,** *39* (13), 3817-26.

70. Winzor, D. J.; Sawyer, W. H., *Quantitative characterization of ligand binding*. New York : Wiley-Liss, c1995.: 1995.

71. Watterson, S. J.; Mitra, S.; Swierczek, S. I.; Bennett, B.; Holz, R. C., Kinetic and spectroscopic analysis of the catalytic role of H79 in the methionine aminopeptidase from Escherichia coli. *Biochemistry* **2008,** *47* (45), 11885-93.

72. Dreyton, C. J.; Knuckley, B.; Jones, J. E.; Lewallen, D. M.; Thompson, P. R., Mechanistic studies of protein arginine deiminase 2: evidence for a substrate-assisted mechanism. *Biochemistry* **2014,** *53* (27), 4426-33.

73. Anderson, V. E., Isotope effects on enzyme-catalyzed reactions. *Current Opinion in Structural Biology* **1992,** *2* (5), 757-764.

74. Jenson, D. L.; Barry, B. A., Proton-coupled electron transfer in photosystem II: proton inventory of a redox active tyrosine. *J Am Chem Soc* **2009,** *131* (30), 10567-73.

75. Elrod, J. P.; Hogg, J. L.; Quinn, D. M.; Venkatasubban, K. S.; Schowen, R. L., Protonic reorganization and substrate structure in catalysis by serine proteases. *J Am Chem Soc* **1980,** *102* (11), 3917-3922.

76. (a) Chow, C.; Xu, H.; Blanchard, J. S., Kinetic characterization of hydrolysis of nitrocefin, cefoxitin, and meropenem by beta-lactamase from Mycobacterium tuberculosis. *Biochemistry* **2013,** *52* (23), 4097-104; (b) Biro, F. N.; Zhai, J.; Doucette, C. W.; Hingorani, M. M., Application of stopped-flow kinetics methods to investigate the mechanism of action of a DNA repair protein. *Journal of visualized experiments : JoVE* **2010,** (37).

77. Ang, T. F.; Maiangwa, J.; Salleh, A. B.; Normi, Y. M.; Leow, T. C.,

Dehalogenases: From Improved Performance to Potential Microbial Dehalogenation Applications. *Molecules* **2018,** *23* (5).

78. Evers, T. H.; Appelhof, M. A.; Meijer, E. W.; Merkx, M., His-tags as Zn(II) binding motifs in a protein-based fluorescent sensor. *Protein Eng Des Sel* **2008,** *21* (8), 529-36.

79. Cleland, W. W., Mechanisms of enzyme-catalyzed reactions. *Advances in Enzymology and Related Areas of Molecular Biology* **1997,** *45*, 273-387.

80. Hubert Bradford Vickery, C. S. L., ON THE SEPARATION OF HISTIDINE AND ARGININE. *Journal of biological chemistry* **1928,** *78* (3), 627-635.

81. Cleland, W. W., Use of isotope effects to elucidate enzyme mechanisms. *Crit. Rev. Biochem.* **1982,** *13*, 385-427.

82. Salomaa, P.; Schaleger, L. L.; Long, F. A., Solvent Deuterium Isotope Effects on Acid-Base Equilibria. *J. Am. Chem. Soc.* **1964,** *86*, 1-7.

83. Leffek, K. T., SECONDARY KINETIC ISOTOPE EFFECTS IN BIMOLECULAR NUCLEOPHILIC SUBSTITUTIONS: I. DEUTERIUM EFFECTS IN THE BUNTE SALT REACTION. *Canadian Journal of Chemistry* **1964,** *42* (4), 851-855.

84. Elrod, J. P.; Hogg, J. L.; Quinn, D. M.; Venkatasubban, K. S.; Schowen, R. L., Protionic reorganization and substrate structure in catalysis by serine proteases. *J. Am. Chem. Soc.* **1980,** *102*, 3917-3922.

85. Sobrado, P.; Fitzpatrick, P. F., Solvent and primary deuterium isotope effects show that lactate CH and OH bond cleavages are concerted in Y254F flavocytochrome b2, consistent with a hydride transfer mechanism. *Biochemistry* **2003,** *42* (51), 15208-15214.

86. Chow, C.; Xu, H.; Blanchard, J. S., Kinetic Characterization of Hydrolysis of Nitrocefin, Cefoxitin, and Meropenem by β-Lactamase from Mycobacterium tuberculosis. *Biochemistry* **2013,** *52* (23), 4097-4104.

87. Martinez, S.; Wu, R.; Sanishvili, R.; Liu, D.; Holz, R., The active site sulfenic acid ligand in nitrile hydratases can function as a nucleophile. *J Am Chem Soc* **2014,** *136* (4), 1186-9.

88. Baxter, J.; Cummings, S. P., The current and future applications of microorganism in the bioremediation of cyanide contamination. *Antonie Van Leeuwenhoek* **2006,** *90* (1), 1-17.

89. (a) Copley, S. D., Microbial dehalogenases: enzymes recruited to convert xenobiotic substrates. *Current opinion in chemical biology* **1998,** *2* (5), 613-7; (b) Janssen, D. B.; Oppentocht, J. E.; Poelarends, G. J., Microbial dehalogenation. *Current opinion in biotechnology* **2001,** *12* (3), 254-8.

90. (a) Benning, M. M.; Taylor, K. L.; Liu, R. Q.; Yang, G.; Xiang, H.;

Wesenberg, G.; Dunaway-Mariano, D.; Holden, H. M., Structure of 4-chlorobenzoyl coenzyme A dehalogenase determined to 1.8 A resolution: an enzyme catalyst generated via adaptive mutation. *Biochemistry* **1996,** *35* (25), 8103-9; (b) Franken, S. M.; Rozeboom, H. J.; Kalk, K. H.; Dijkstra, B. W., Crystal structure of haloalkane dehalogenase: an enzyme to detoxify halogenated alkanes. *The EMBO journal* **1991,** *10* (6), 1297-302.

91. de Jong, R. M.; Tiesinga, J. J.; Rozeboom, H. J.; Kalk, K. H.; Tang, L.; Janssen, D. B.; Dijkstra, B. W., Structure and mechanism of a bacterial haloalcohol dehalogenase: a new variation of the short-chain dehydrogenase/reductase fold without an NAD(P)H binding site. *The EMBO journal* **2003,** *22* (19), 4933-44.

92. Poelarends, G. J.; Saunier, R.; Janssen, D. B., trans-3-Chloroacrylic acid dehalogenase from Pseudomonas pavonaceae 170 shares structural and mechanistic similarities with 4-oxalocrotonate tautomerase. *Journal of bacteriology* **2001,** *183* (14), 4269-77.

93. Reddy, G. V.; Gold, M. H., Purification and characterization of glutathione conjugate reductase: a component of the tetrachlorohydroquinone reductive dehalogenase system from Phanerochaete chrysosporium. *Arch Biochem Biophys* **2001,** *391* (2), 271-7.

94. (a) Rudolph, J.; Erbse, A. H.; Behlen, L. S.; Copley, S. D., A radical intermediate in the conversion of pentachlorophenol to tetrachlorohydroquinone by Sphingobium chlorophenolicum. *Biochemistry* **2014,** *53* (41), 6539-49; (b) Orser, C. S.; Lange, C. C.; Xun, L.; Zahrt, T. C.; Schneider, B. J., Cloning, sequence analysis, and expression of the Flavobacterium pentachlorophenol-4-monooxygenase gene in Escherichia coli. *Journal of bacteriology* **1993,** *175* (2), 411-6; (c) Hlouchova, K.; Rudolph, J.; Pietari, J. M.; Behlen, L. S.; Copley, S. D., Pentachlorophenol hydroxylase, a poorly functioning enzyme required for degradation of pentachlorophenol by Sphingobium chlorophenolicum. *Biochemistry* **2012,** *51* (18), 3848-60.

95. Hu, J.; Su, Q.; Schlessman, J. L.; Rokita, S. E., Redox control of iodotyrosine deiodinase. *Protein science : a publication of the Protein Society* **2019,** *28* (1), 68-78.

96. Peat, T. S.; Newman, J.; Balotra, S.; Lucent, D.; Warden, A. C.; Scott, C., The structure of the hexameric atrazine chlorohydrolase AtzA. *Acta Crystallogr D Biol Crystallogr* **2015,** *71* (Pt 3), 710-20.

97. Yang, X.; Bennett, B.; Liu, D.; Holz, R. C., Analyzing the Catalytic Mechanism of a Hydrolytic Metallo-Dehalogenase. *J. Biol. Chem* **2019**.

98. Tropea, J. E.; Cherry, S.; Waugh, D. S., Expression and purification of soluble His(6)-tagged TEV protease. *Methods Mol Biol* **2009,** *498*, 297-307.

99. Yang, X.; Bennett, B.; Holz, R. C., Analyzing the function of the insert region found between the alpha and beta-subunits in the eukaryotic nitrile hydratase from Monosiga brevicollis. *Archives of biochemistry and biophysics*

2018, *657*, 1-7.

100. Adams, P. D.; Afonine, P. V.; Bunkoczi, G.; Chen, V. B.; Davis, I. W.; Echols, N.; Headd, J. J.; Hung, L.-W.; Kapral, G. J.; Grosse-Kunstleve, R. W.; McCoy, A. J.; Moriarty, N. W.; Oeffner, R.; Read, R. J.; Richardson, D. C.; Richardson, J. S.; Terwilliger, T. C.; Zwart, P. H., PHENIX: a comprehensive Python-based system for macromolecular structure solution. *Acta Crystallographica Section D* **2010,** *66* (2), 213-221.

101. Emsley, P.; Lohkamp, B.; Scott, W. G.; Cowtan, K., Features and development of Coot. *Acta crystallographica. Section D, Biological crystallography* **2010,** *66* (Pt 4), 486-501.

102. Pettersen, E. F.; Goddard, T. D.; Huang, C. C.; Couch, G. S.; Greenblatt, D. M.; Meng, E. C.; Ferrin, T. E., UCSF Chimera--a visualization system for exploratory research and analysis. *Journal of computational chemistry* **2004,** *25* (13), 1605-12.

103. Signor, L.; Boeri Erba, E., Matrix-assisted laser desorption/ionization time of flight (MALDI-TOF) mass spectrometric analysis of intact proteins larger than 100 kDa. *Journal of visualized experiments : JoVE* **2013,** (79).

104. Kussmann, M.; Roepstorff, P., Sample preparation techniques for peptides and proteins analyzed by MALDI-MS. *Methods in molecular biology* **2000,** *146*, 405-24.

105. Trott, O.; Olson, A. J., AutoDock Vina: improving the speed and accuracy of docking with a new scoring function, efficient optimization, and multithreading. *J Comput Chem* **2010,** *31* (2), 455-61.

106. (a) Krissinel, E., Crystal contacts as nature's docking solutions. *Journal of computational chemistry* **2010,** *31* (1), 133-43; (b) Krissinel, E.; Henrick, K., Inference of macromolecular assemblies from crystalline state. *Journal of molecular biology* **2007,** *372* (3), 774-97.

107. Holm, L.; Laakso, L. M., Dali server update. *Nucleic acids research* **2016,** *44* (W1), W351-5.

108. (a) Crowder, M. W.; Spencer, J.; Vila, A. J., Metallo-beta-lactamases: novel weaponry for antibiotic resistance in bacteria. *Accounts of chemical research* **2006,** *39* (10), 721-8; (b) Fryszczyn, B. G.; Adamski, C. J.; Brown, N. G.; Rice, K.; Huang, W.; Palzkill, T., Role of beta-lactamase residues in a common interface for binding the structurally unrelated inhibitory proteins BLIP and BLIP-II. *Protein science : a publication of the Protein Society* **2014,** *23* (9), 1235-46; (c) Knaus, T.; Schober, M.; Kepplinger, B.; Faccinelli, M.; Pitzer, J.; Faber, K.; Macheroux, P.; Wagner, U., Structure and mechanism of an inverting alkylsulfatase from Pseudomonas sp. DSM6611 specific for secondary alkyl sulfates. *The FEBS journal* **2012,** *279* (23), 4374-84; (d) Walsh, T. R.; Toleman, M. A.; Poirel, L.; Nordmann, P., Metallo-beta-lactamases: the quiet before the storm? *Clinical microbiology reviews* **2005,** *18* (2), 306-25.

109. (a) Quiroga, R.; Villarreal, M. A., Vinardo: A Scoring Function Based on Autodock Vina Improves Scoring, Docking, and Virtual Screening. *PLoS One* **2016,** *11* (5), e0155183; (b) Seeliger, D.; de Groot, B. L., Ligand docking and binding site analysis with PyMOL and Autodock/Vina. *J Comput Aided Mol Des* **2010,** *24* (5), 417-22.

110. Baier, F.; Tokuriki, N., Connectivity between catalytic landscapes of the metallo-beta-lactamase superfamily. *Journal of molecular biology* **2014,** *426* (13), 2442-56.

111. (a) Queenan, A. M.; Bush, K., Carbapenemases: the versatile beta-lactamases. *Clinical microbiology reviews* **2007,** *20* (3), 440-58, table of contents; (b) Meini, M. R.; Llarrull, L. I.; Vila, A. J., Overcoming differences: The catalytic mechanism of metallo-beta-lactamases. *FEBS letters* **2015,** *589* (22), 3419-32.

112. Garau, G.; Bebrone, C.; Anne, C.; Galleni, M.; Frere, J. M.; Dideberg, O., A metallo-beta-lactamase enzyme in action: crystal structures of the monozinc carbapenemase CphA and its complex with biapenem. *J Mol Biol* **2005,** *345* (4), 785-95.

113. Hagelueken, G.; Adams, T. M.; Wiehlmann, L.; Widow, U.; Kolmar, H.; Tummler, B.; Heinz, D. W.; Schubert, W. D., The crystal structure of SdsA1, an alkylsulfatase from Pseudomonas aeruginosa, defines a third class of sulfatases. *Proceedings of the National Academy of Sciences of the United States of America* **2006,** *103* (20), 7631-6.

114. Christianson, D.; Cox, D., Catalysis by Metal-Activated Hydroxide in Zinc anc Manganese Metalloenzymes. *Annu. Rev. Biochem.* **1999,** *68*, 33-57.

115. Desmarais, W.; Bienvenue, D. L.; Bzymek, K. P.; Petsko, G. A.; Ringe, D.; Holz, R. C., The 0.95 Å Resolution and Low pH Crystal Structures of the Aminopeptidase from *Aeromonas proteolytica*. *J Biol Inorg Chem.* **2006,** *11*, 398-408.

116. Sakurai, M.; Furuki, T.; Inoue, Y., The pKa of the zinc-bound water in carbonic anhydrase and its model compounds as studied by the AM1 calculation coupled with a reaction field theory. *The Journal of Physical Chemistry* **1995,** *99* (50), 17789-17794.

117. Cosper, N. J.; Bienvenue, D. L.; Shokes, J.; Gilner, D. M.; Tsukamoto, T.; Scott*, R.; Holz*, R. C., The dapE-encoded N-succinyl-L,L-Diaminopimelic Acid Desuccinylase from Haemophilus influenzae is a Dinuclear Metallohydrolase. *J. Am. Chem. Soc.* **2004,** *125*, 14654-14655.

118. Breslow, R., Biomimetic Chemistry and Artificial Enzymes: Catalysis by Design. *Accounts of Chemical Research* **1995,** *28* (3), 146-153.

119. Chen, H.; Wang, H.; Wang, T.; Huang, S.; Zang, X.; Li, S.; Jiang, J., Identification of the metal center of chlorothalonil hydrolytic dehalogenase and enhancement of catalytic efficiency by directed evolution. *Applied Environmental Biotechnology; Vol 1, No 1 (2016)* **2016**.